FABRICATION, CHARACTERIZATION, AND MODELING OF RANDOM ANTI-REFLECTIVE OPTICAL SURFACE STRUCTURES

by

Rajendra Joshi

A dissertation submitted to the faculty of
The University of North Carolina at Charlotte
in partial fulfillment of the requirements
for the degree of Doctor of Philosophy in
Optical Science and Engineering

Charlotte

2020

Approved by:

_____
Dr. Gregory J. Gbur

_____
Dr. Ishwar D. Aggarwal

_____
Dr. Glenn D. Boreman

_____
Dr. Thomas Schmedake

ABSTRACT

RAJENDRA JOSHI. Fabrication, Characterization, and Modeling of Random Anti-reflective Optical Surface Structures. (Under the direction of DR. GREGORY J. GBUR)

Optical surfaces can be fabricated to be anti-reflective (AR) by coating single- or multi-layered dielectrics on them. However, the optical response through these surfaces is polarization- dependent and angle-dependent, and they degrade quickly on exposure to the environment and laser radiation. One alternative to these coated AR surfaces are periodic sub-wavelength AR structures, which possess no material mismatch with the substrate, contrary to that in the case of dielectric-coated AR surfaces. The polarization-dependency and angle-dependency of optical response of these structured surfaces is still an issue for some applications, however.

Optical surfaces fabricated with random AR surface structures (rARSS) have proven to be largely angle-independent and polarization-independent. They also withstand higher power laser damage threshold. There is a limited amount of research done in the area of fabrication and modeling of the rARSS.

We extended the research area in the fabrication of rARSS and added a physical model which will be able to simulate the optical response of the fabricated rARSS and relate it to the fabrication parameters. The fused silica substrates were etched using inductively coupled plasma deep reactive ion etching (ICP DRIE) method. The etching parameters were investigated and optimized to get very high transmittance (nearly perfect) from Visible to Short-wave Infrared (SWIR) region.

ACKNOWLEDGMENTS

I am deeply grateful to my advisor, Prof. Greg J. Gbur. During my entire period of study and research in the graduate program, and during ups and downs, he stood as a lighthouse and guided me in a right direction. My research was guided by his sharp intuition and insight. His knowledgeable and enthusiastic approach to research, which often went beyond science itself, was an inspiration for me. He has always been diligent in preparing me for all my publications and presentations. It has been my privilege to have numerous scientific discussions with him which make this dissertation work possible.

I would like to thank my committee members, Profs. Ishwar D. Aggarwal, Glenn D. Boreman and Thomas Schmedake for serving on my dissertation committee. I am grateful for their time and appreciate their comments and support in completing the dissertation.

I would like to thank Prof. Menelaos K. Poutous for making me understand the basics of the research work. I would like to thank Dr. Prakash Koirala for his encouragement. His advice has been invaluable in completing the dissertation. I would also like to thank graduate program director of Optical Science and Engineering, Prof. Angela Davies Allen for her help and guidance during my study at UNC Charlotte.

I would like to thank my fellows, Dr. Kevin Major, Courtney Taylor, and Abigail Peltier for scientific interactions and discussions over a broad range of research topics, which led to several collaborations.

I am thankful to Dr. Robert Hudgins and Dr. Lou Deguzman for their help in teaching me to operate many devices in the Optoelectronics Center at UNCC. Also, I would like to thank Mark Clayton for assisting me throughout many administrative issues.

I was supported by the GASP tuition award from UNCC Graduate School throughout

my graduate studies. I am thankful for the teaching assistantship provided by the Department of Optical Science and Engineering. My research assistantship in Prof. Ishwar D. Aggarwal's Optical Surface Structures Laboratory was supported through grants from Naval Research Laboratory (NRL). I would like to acknowledge the grant supports from NRL (N000173-12-1 G020) and ONR (N00014-13-1-0208). I would like to thank Dr. Lynda Busse (NRL), Dr. Catalin Florea (NRL) and Dr. Jesse Frantz (NRL) in the establishment of the research plan and collaboration in the research.

At last, I wish to express my deep gratitude to my parents, my beloved wife Deepa, and my children, Neha and Pranav, for their endless love, support, and encouragement, which always kept me motivated throughout this journey.

TABLE OF CONTENT

LIST OF TABLES

LIST OF FIGURES

LIST OF ABBREVIATIONS

~	approximate
1-D	one-dimensional
2-D	two-dimensional
3-D	three-dimensional
AFM	atomic force microscope
AOI	angle of incidence
AR	anti-reflection
ARSS	anti-reflective surface structure
ASE	advanced silicon etcher
BBAR	Broadband antireflection
CVD	chemical vapor deposition
DRIE	deep reactive ion etching
FS	fused silica
ICP	inductively coupled plasma
IR	infrared

pARSS	periodic anti-reflective surface structures
PECVD	plasma enhanced chemical vapor deposition
PVD	Physical vapor deposition
rARSS	random anti-reflective surface structures
RF	radio frequency
RIE	reactive ion etching
SE	spectroscopic ellipsometry
SW	short wavelength
SWIR	short-wave infrared
TE	transverse electric
TM	transverse magnetic
UV	ultraviolet
VIS	visible
WVASE	Woollam variable angle spectroscopic ellipsometer

CHAPTER 1 INTRODUCTION

1.1 Overview of the Dissertation

Light waves incident on a boundary separating two physical materials always undergo partial reflection, due to the discontinuity of the refractive index values across the boundary. In order to suppress this Fresnel-type reflection, anti-reflection coatings and structures are usually applied to the boundary. The conventional method of fabricating a layered anti-reflection (AR) coating on the surface, for a specific light wavelength, is to deposit a dielectric material of suitable thickness and refractive index on top of the substrate. The required refractive index and the thickness of the layer are related to the wavelength of the incident light and, the index difference between superstrate and substrate. If the path difference between the two waves reflected from the two interfaces, of a film-substrate layered structure is of the order of quarter of the wavelength ($\lambda/4$) of the incident wave, destructive interference would occur, as shown in figure 1 below. As a result, there will be no net energy reflected at the interface. Assuming there is a negligible amount of absorption in the substrate and the layered dielectric, all the incident power will be transmitted through the substrate [1].

Conventionally, anti-reflecting layers of thin films can be fabricated by the deposition of a single dielectric or, a stack of multiple discrete dielectric layers composed of various refractive index materials. The fabrication of the layered AR coatings is achieved using

thin film deposition techniques, such as Physical Vapor Deposition (PVD), Chemical Vapor Deposition (CVD), or Plasma Enhanced Chemical Vapor Deposition (PECVD).

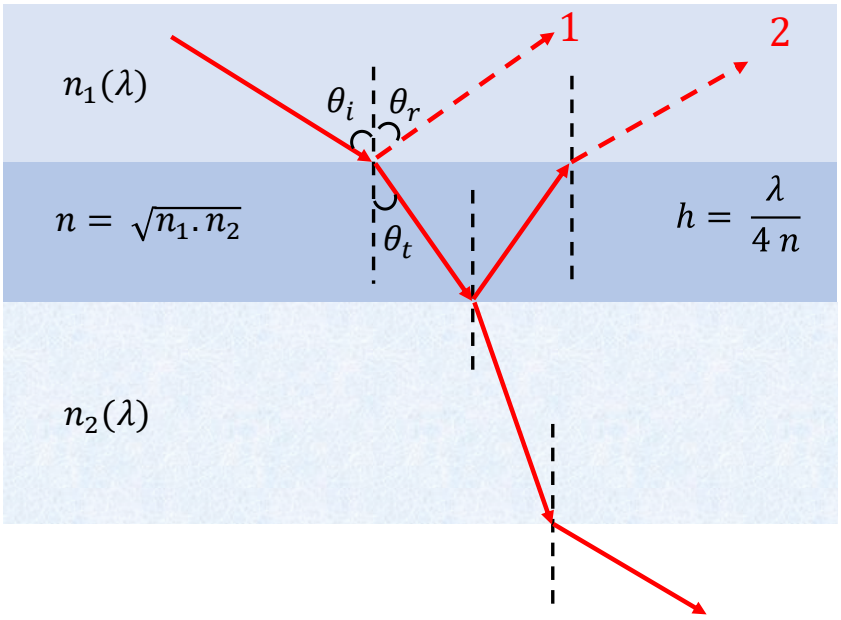

Figure 1.1. Quarter wave layer deposition of a dielectric of refractive index n between two dielectrics of refractive indices n_1 and n_2. The refractive index of the deposited dielectric is the square root of the product of n_1 and n_2. and the thickness of the dielectric is target wavelength divided by four times the refractive index of the deposited dielectric layer.

Specifically, PECVD is a plasma-assisted process during which a radio frequency (RF) electromagnetic field is applied to a low-pressure gas mixture in an evacuated chamber. The RF-energy induces a mixture of highly energetic electrons, ions, neutral atoms and molecules and reactive radicals, known as plasma. The plasma interacts with the substrate. The platen power is set so that deposition occurs on the substrate by the interaction of these atomic and molecular fragments.

For the fabrication of a single layer AR coating, a dielectric material of suitable refractive index and thickness is deposited on an optical substrate such that the path

difference between the two reflected rays from the two interfaces interfere destructively. As a result, the incident power is not reflected. The refractive index of the coated intermediate layer should be given by

$$n = \sqrt{n_1 . n_2} \qquad (1.1)$$

and the optical path-difference should be $\frac{\lambda}{4n}$ [2, 3]. However, the single layer AR coating does not work efficiently if the wavelengths of the incident light differs from the wavelength for which this coating has been designed. The AR effect for the broadband spectral region can be significantly improved using a multi-layered AR coating on the substrate. The various layers of different thicknesses and hence different effective refractive indices are designed to induce destructive interference for different wavelengths of incident light.

A large volume of work has been done related to the fabrication of AR layers with dielectrics, however, issues still exist [4-6]. One of the difficulties is to find dielectrics of refractive indices to match the AR condition on the surfaces given in equation (1.1). A large number of alternating index layers is required to fabricate a surface suitable for broad-band AR performance. Secondary issues arise when the fabricated materials are exposed to environmental conditions or high-power laser radiation. Since the AR coating layers are composed of at least two different materials, and the substrate is different than the deposited dielectrics, the thermal and mechanical stresses are mismatched in the strata. As a result, when layered AR coatings are exposed to environmental conditions for a long time, they can degrade quickly. The coated AR layers are vulnerable to high energy radiations. High energy laser incident radiations impose thermal and radiation stresses on the coated layers and can ablate or fracture the layers as a result [7].

In 1879, Lord Rayleigh was one of the first who analyzed the reflections of waves at the interfaces of the two media of different refractive indices and proposed coating a substrate with materials of refractive indices that form a gradient-index transition from the superstrate to the substrate, in order to overcome the shortcomings of homogeneously layered AR coatings [8].

These layered structures reduce the optical discontinuity at the interfaces. Some alternatives to broad-band AR coatings fabricated with multi-layered dielectrics are: a) Periodic sub-wavelength surface relief structures and, b) Random surface structures. Periodic sub-wavelength anti-reflective surface structures (pARSS) are fabricated by using standard photolithographic techniques. First, the optical substrate is coated with photoresist and an etching mask is made by exposing the resist. This can be done by the use of UV-exposure systems, such as stepper, contact alignment exposure system, e-beam writer etc. [6]. The exposed resist is developed after exposure to create the surface relief of the etching mask with the desired contours. The pattern is then transferred to the substrate using deep etching (plasma) methods, such as reactive ion etching (RIE) or inductively coupled plasma (ICP) RIE. The fabrication of periodic sub-wavelength surface relief structures (pARSS) can be a lengthy process, depending on the complexity of the masking resist profile.

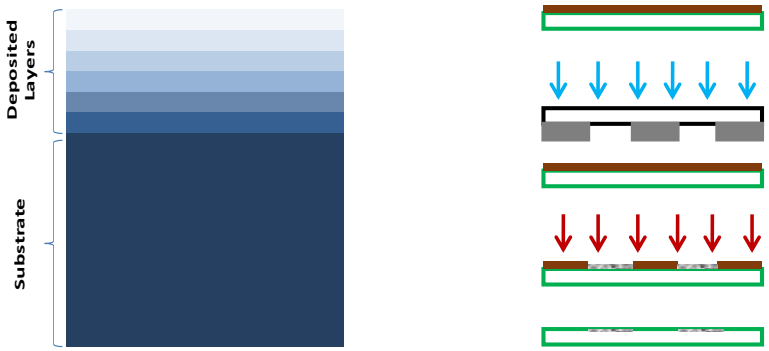

Figure 1.2. Optical surface with layered coatings and periodic structures are shown. (Left) The layered coatings can be single layered, multiple pairs with dielectric layers of high and low refracting indices or dielectric coatings of gradient indexed materials. (Right) The periodic structures can be fabricated using photolithographic exposure systems on coated resists to make an etch mask and then transferring the structures of the mask to the substrate using RIE method.

Light transmission through these periodic sub-wavelength surface relief pARSS is angle-dependent and, polarization dependent at angles other than normal incidence [9].

Optical surfaces with incident-angle and polarization independent transmissivity can be achieved using non-periodic sub-wavelength structured surfaces. These types of structures are usually classified as random anti-reflecting surface structures (rARSS). The optical transmission of this type of AR surfaces has been measured to be largely angle and polarization independent [10].

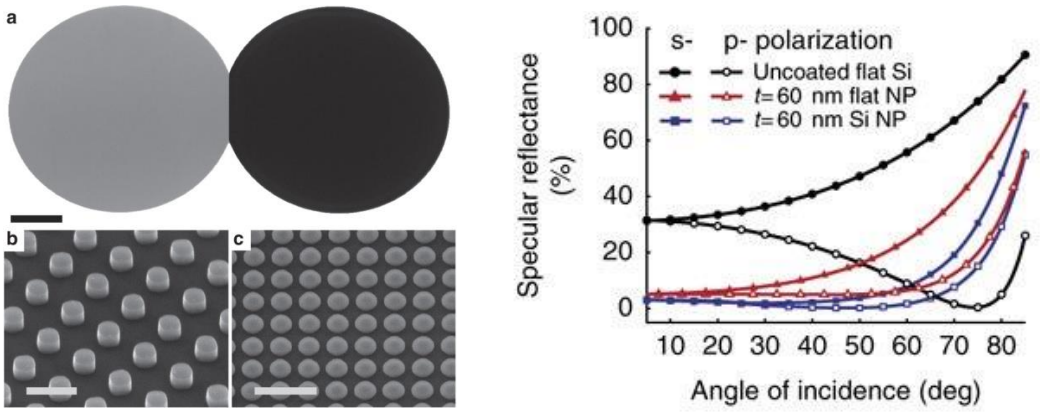

Figure 1.3. (Left) Periodic sub-wavelength structures on a Silicon substrate and their optical response are shown. (Right) The reflection is decreased significantly after the fabrication of SWS on the bare silicon substrate. The reflections are, however, largely polarized dependent.[9]

The chemically reactive gas ions produced by applying strong RF frequency electromagnetic field, typically 13.56 MHz, to the electrode of (ICP) RIE chamber are bombarded directly on an optical surface to fabricate rARSS on the surface. The fluoro-carbons are usually used to produce the reactive plasma inside the RIE chamber for the fabrication of rARSS on fused silica substrates [11].

The substrate is placed on a temperature-controlled electrode, and the energetic ions are directed to bombard the surface. The energy and direction of the bombarding ions can be controlled by the platen and coil powers respectively. The bombardment rate and hence the etch rate can be controlled by the gas flow rate, bias power and the pressure of the gases inside the chamber [12]. The substrate was etched for a certain time and varied the other etching parameters depending on the transmissivity requirement of the spectral region of interest.

Since the AR surface is fabricated on the substrate without deposition of material, there are no thin film stresses or thermal mismatches. As a result, the textured surfaces can

withstand higher laser damage thresholds. Recent results show that the laser damage threshold on rARSS fabricated fused silica samples is near 100 J/cm^2 using 1.06 μm pulsed laser [13].

All ARSS fine structure is smaller than the wavelength of the incident light, and as such, they can be classified as sub-wavelength (SW) structures. These SW structures can be regular or random. If the period of the structured pillars or any other shaped structure is constant over the surface of the substrate, then the structures are known as periodic. If the period of the structures is not well-defined or if there is no characteristic period, the structures are random.

For the fabrication of periodic AR surface relief structures, an etch mask can be used with conventional photolithography as described above. The fabrication of random ARSS can be done using a thin metal mask or without a metal mask. The process involves the use of (ICP) DRIE with the radicals adsorbed in the substrate surface and, the following etching reaction is enhanced by the reactive ion bombardment. The process variables in the fabrication of random AR structures are etching time, chamber pressure, platen and coil power; and the flow rates of reactive gases [11, 14]. The etching system is described in chapter 2 in more detail.

The differences in the fabrication of layered and periodic AR surfaces with rARSS include fewer fabrication steps, decreased processing time. The fabricated SW features are dimension tolerant because of their randomness. Since the interference phenomenon is destroyed by random structures of the random surface, the spectral band AR performance is fringeless as compared to the spectral response through the layered AR coatings. These

random AR structures, thus, show a suppressed Fresnel reflection over larger range of the angle of incidence (AOI).

1.2 Dissertation Outline

Chapter 1 introduces the anti-reflection (AR) surfaces, and their fabrication using various processes. An overview of techniques used for creating anti-reflective surfaces using conventional methods is given. It briefly discusses about realizing the AR surfaces by thin film deposition and also by fabricating periodic surface structures on the substrates. Then it discusses about the need of random anti-reflective surface structures and its fabrication using inductively coupled plasma deep reactive ion etching (ICP DRIE) method.

In chapter 2, the etching system used in the fabrication of rARSS is briefly described. First the molecular structure of fused silica is given in brief and then the Bosch process used to physically and chemically etch the fused silica surface inside the chamber using ICP DRIE process is described. The use of thin metallic mask as the etch mask and the etching parameters in ICP DRIE method to obtain a random anti-reflective surface structure that produces very high transmittance is described in the chapter.

Next, in chapter 3, the characterization of the fabricated random anti-reflective surface structures on the substrate is described. First the surface profile was measured using UV confocal microscopy, and then the results of the transmittance enhancement of the fabricated samples at various etching conditions are shown. Next, the fabrication of AR surface that have very high transmittance from visible to short-wave infrared region are discussed. Then these fabricated samples are characterized using spectroscopic ellipsometry.

In chapter 4, we analyzed the transmittance enhancement of the fabricated optical substrates and simulated the transmittance enhancement by the method of calculating the transmissivity through multi-layered dielectric media, derived using the modified Bruggeman's effective medium approximation and adding scattering factor in it.

Finally, the chapter 5 summarizes the research work discussed in this dissertation and briefly a direction is given for further work.

CHAPTER 2 ETCHING PROCESSES ON FUSED SILICA

2.1 Molecular Structure of Fused Silica

The building block of molecular structure of silicon dioxide is a three-dimensional tetrahedral cell structure of SiO_4 formed by four oxygen atoms surrounding a silicon ion as shown in figure 2.1(a). The Silicon and Oxygen atoms arrange themselves in such a way that bond length of Si-O bond is ~ 0.162 nm. The bond length is slightly smaller than the sum of the covalent radii of Si (0.11 nm) and O (0.066 nm) atoms, which is 0.176 nm. The normal distance between two Oxygen atoms is ~ 0.262 nm. The bond length of Si-Si is approximately 0.31 nm; however, it solely depends upon the SiO_2 arrangement. The bond angles O-Si-O are basically 109.5º, tetrahedral angle. The bond angle of Si-O-Si is approximately 145º for a free molecule, but it can vary from about 110º to 170º with a small change in the bond energy. The rotation of the bond about the axis is almost completely free as shown in figure 2.1(b).

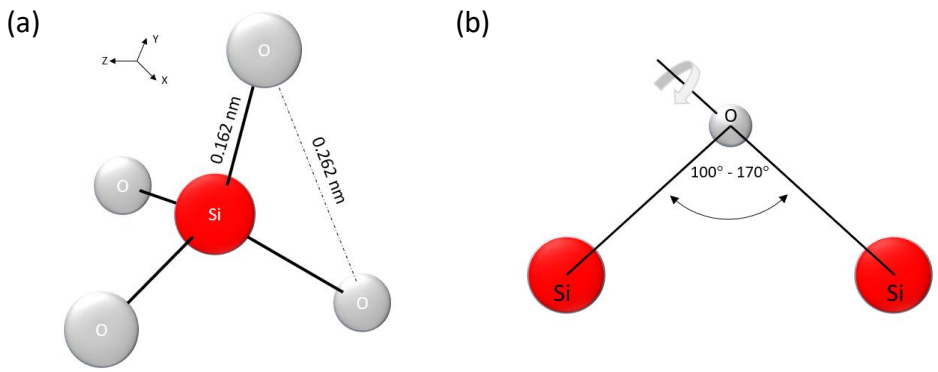

Figure 2.1. (a) SiO4 as a building block of SiO_2 (b) Si-O-Si bridge bonds between neighboring tetrahedra.

The basic units of tetrahedral structure of SiO_4 bond together by sharing an oxygen atom in between them and form a SiO_2 molecular structure. This is illustrated in figure 2.2 in a sample six-membered ring.

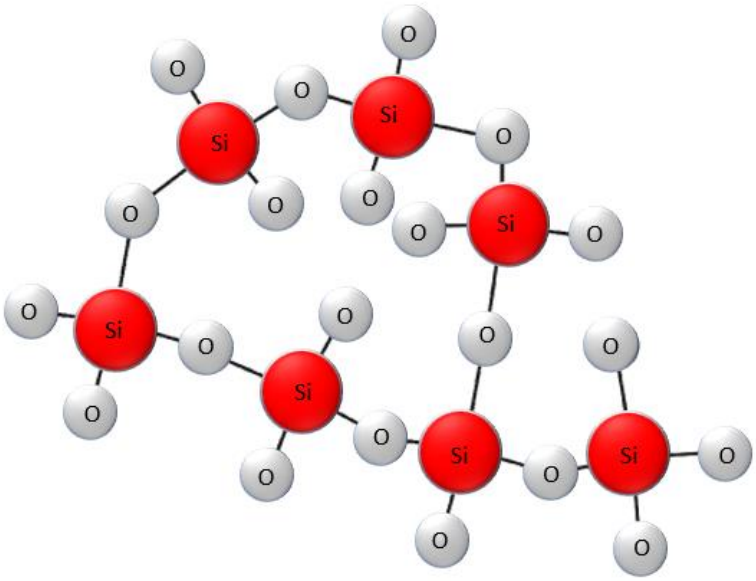

Figure 2.2. Six-membered SiO_2 molecule ring

The SiO_2 can exist in amorphous or in crystalline structure. The reason for the amorphous oxide structure is the absence of any crystalline form of SiO_2 whose lattice size closely matches the silicon lattice [15].

2.2 Etching System

The etching experiment was performed using STS ICP system as shown in the figure 2.3. The impedance of an ICP etching tool is matched to that of the plasma. This allows having a high coupling efficiency between the applied field and electrons in the plasma. The presence of solenoidal magnetic field improves the confinement of the plasma by reducing its losses around the chamber. Also, as the coil and platen power can be varied independently, the etchant species can be increased without increasing the radio frequency (RF) power to the substrate. This tool is able to produce high plasma densities at pressure less than 10 mTorr. Low pressure operation helps to reduce the scattering and therefore improves the control of etch profiles. The gases used in this system were SF_6, C_4F_8, Ar and O_2. The gas flow rates were controlled by mass flow controllers. The heat generated from the plasma can be transferred to the substrate. However, the temperature of the substrate can be stabilized by backside cooling with helium (He) gas. It is necessary to keep the substrate at a constant temperature to get a desired etching profile. The chamber can be pumped to a low pressure (~ 10^{-7} Torr) by a turbo pump which is backed by a dry pump. The etching gas mixtures are introduced through the annular region at the top of the chamber lid. The plasma of the etcher is inductively coupled through a coil at 13.56 MHz, with independent energy control provided by 13.56 MHz RF biasing on the substrate.

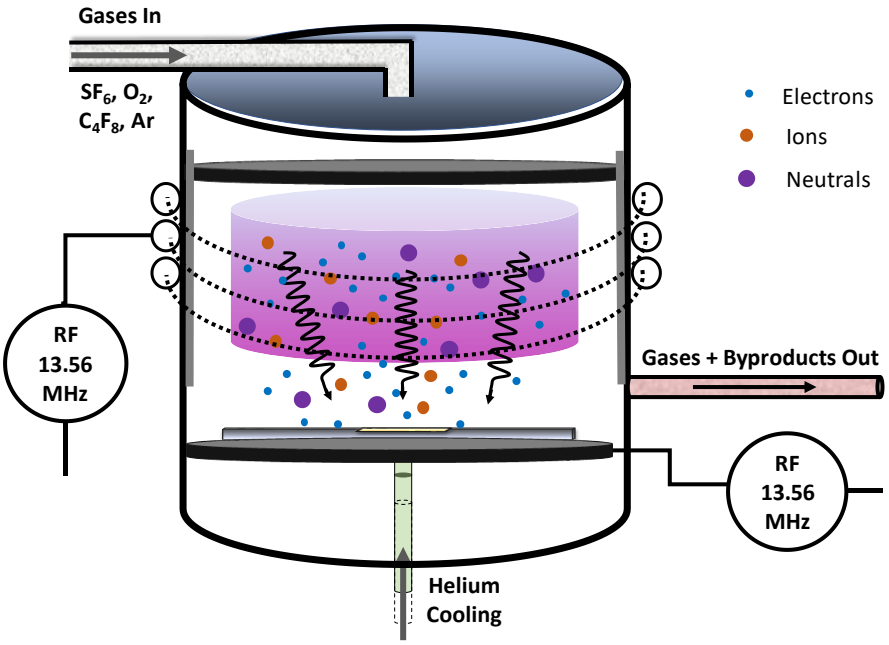

Figure 2.3. Schematics of STS ICP system Etcher. It uses the ionic bombardment of reactive plasma of fluorine-based gases on the fused silica substrate to make random AR surface structures on the substrate. The coil power, platen power can independently be varied which gives freedom to choose a variable at a time.

2.3 Reactive Ion Etching Process

Reactive ion etching (RIE) is an anisotropic process which combines the plasma and sputter etching processes. This is highly anisotropic process which is mostly used in the fabrication of micro- and nanostructures [16, 17]. The etch rate is not dependent on the crystalline structure of silicon, unlike wet etching, as depicted in figure 2.4. RIE creates trenches that have, in principle, vertical sidewalls due to directional ion bombardment. Still, the RIE processes that rely on pure SF_6 or CF_4 chemistry are not capable of producing high aspect ratio structures because the sidewalls are also exposed to highly reactive fluorine radicals [18, 19]. Anisotropy can be enhanced by using less reactive etchants, or by protecting the sidewalls with a passivation layer.

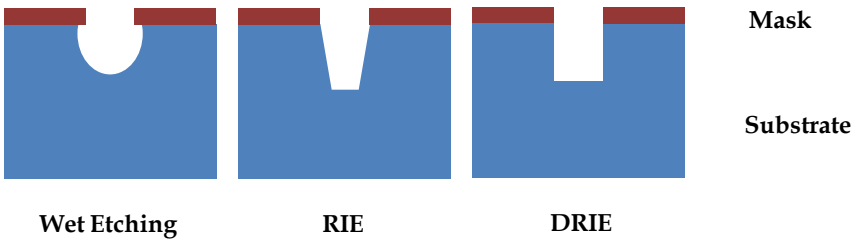

Figure 2.4. The difference between three different types of etching methods for fused silica.

Chlorine and bromine plasmas can also be used to etch fused silica, even though their reactivity with silicon is considerably lower than the reactivity of fluorine [20-22]. Due to their low reactivity, Cl- and Br- radicals do not etch fused silica spontaneously, or the spontaneous etching that does occur is insignificant. Fused silica is etched only when ion bombardment is present. Because of the directionality of the ions, the etch profiles are anisotropic. However, the etch rate is considerably lower by using less reactive etchants . The selectivity of photoresist, silicon dioxide and metal masks is also lower with Cl-based plasmas than with fluorine plasmas due to a low silicon etch rate and the greater ion bombardment required for the desorption of non-volatile etch products. Low selectivity typically requires the use of metal masks if deep structures are desired [20]. But this restriction is not applicable to the case where surface roughness on the fused silica is desired. This is the reason we used Fluorine based gases to etch the fused silica substrates.

2.4 Bosch Process and Inductive Coupled Plasma Deep Reactive Ion Etching

In plasma etch systems, the plasma is generated by coupling electromagnetic energy into the gas species. It employs radio frequency energy (RF) of 13.56 MHz to create plasma of ionized atoms, electrons, and radicals of reactive gases for etching. In the inductively coupled plasma (ICP) system, the axial magnetic field from surrounding the surrounding

coil induces an azimuthal electric field. The inductive coupling produces a dense plasma inside the chamber due to the magnetic confinement which helps in producing more ions and controlling the etching uniformity [23]. In addition to this field, an extra independently biased RF electric field of 13.56 MHz is applied. The RF frequency is applied to prevent the excessive charging of the insulating substrates, which enhances the efficiency of the ionization process. The induced electric field combined with RF electric field applied between the electrodes act as the electron and ion accelerators [24, 25].

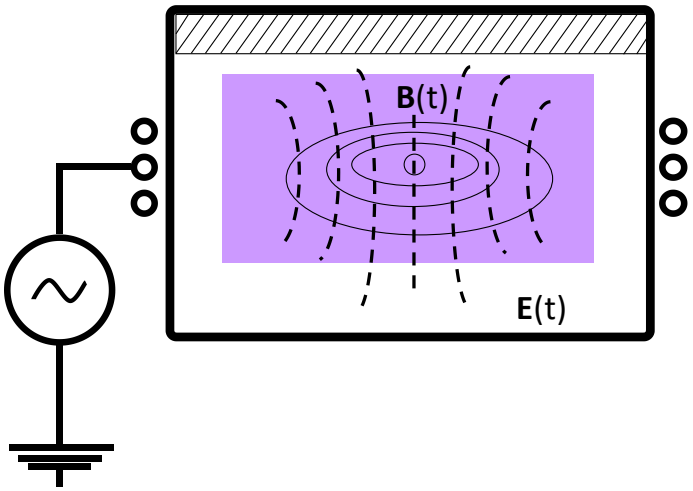

Figure 2.5. Inductively coiled plasma for deep reactive ion etching process

The Bosch process is the most widely used deep reactive ion etching (DRIE) technique [26]. It uses two steps: passivation and etching. The gas octofluoro-cyclobutane (C_4F_8) is introduced in the chamber in the passivation cycle. This gas converts into $(CF_2)_n$ radicals by electron impact dissociation and it diffuses on the substrate. This makes a thin layer of fluorocarbon soft polymer, similar to Teflon [27]. This This layer acts as the mask to helps to reduce the undercut and enhance anisotropic high aspect ratio etching. During the etching cycle, the SF_6 with gases are introduced and the plasma is struck in the gas mixture by the application of capacitive RF power source. This breaks the gas molecules

into reactive ions, electrons and there are neutral atoms too. By the application of electric field between two electrodes, the ions are accelerated towards the substrate to be etched. Then the reactive ions react with the substrate chemically and other particles react physically (similar to the case in sputtering), giving rise to the etched surface depending upon the parameters such as etch mask, energy of the ions (platen power), chamber pressure, type of gas mixture, directionality of the ions (coil power), time of passivation and etch.

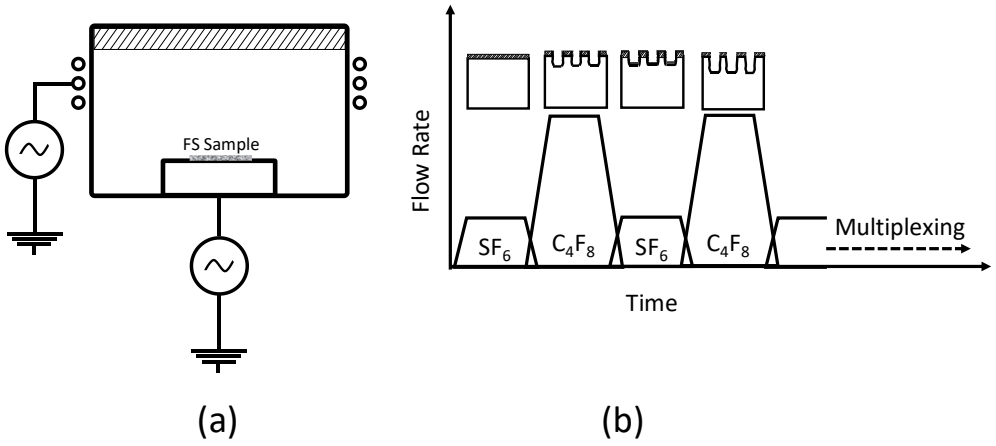

Figure 2.6. Bosch Process applied in fused silica substrate. The figure (a) on the left shows the schematics of the etching mechanism and the figure (b) on the right shows the processing steps schematic vs. time during multiplexing.

The repetition of etching and passivation cycles (called multiplexing) results in almost vertical sidewalls [28]. The drawback of the process is the scalloping of the sidewalls due to the alternating etching and passivation steps [29]. The sidewall roughness can be reduced by shortening the duration of the etching and passivation steps or by post processing: thermal oxidation followed by oxide etching [30]. The schematics of the Bosch process is shown in the figure 2.6.

The etching of the optical substrate using Bosch process is shown in the figure

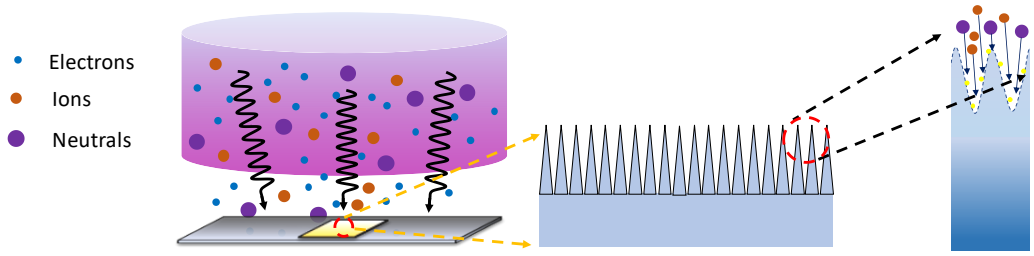

Figure 2.7. The etching of the fused silica optical substrate using Bosch process

The etch chemistry in passivation and etching cycle are given below:

1. Passivation Step

$$C_4F_8 + e^- \rightarrow CF_x^+ + CF_xF^- + e^-$$

$$CF_x \rightarrow nCF_2 \quad \text{(Fluorocarbon polymer)}$$

2. Etching Step

$$SF_6^+ e^- \rightarrow S_xF_y^+ + S_xF_y + F + e^-$$

$$nCF_2^+ + F \rightarrow SO_2F_2 + O_2 + (x-4)F \qquad (x \leq 6)$$

$$2SiO_2 + C_4F_8 \rightarrow 2SiF_4 + 4CO$$

The volatile gas and the unused gases pumped out of the chamber continuously during the multiplexing.

2.5 Etching Parameters of Fused Silica

The random surfaces on the fused silica wafer can be induced by the conventional method as shown in the figure 2.8. Conventionally a fused silica wafer is spin-coated with a positive photoresist and exposed in a 5X reduction stepper to develop rough surface on the photoresist. The rough surface induced on the photoresist can be used as an etch mask in the ICP RIE chamber to transfer the rough surface on the fused silica. However, this method is time consuming and hence it is expensive too.

In a second method, we used a gold sputtered fused silica substrates to etch random anti-reflective surface structures on them as shown in the figure 2.9. The thin layer of gold layer (porous layer) acts as an etch mask in the ICP DRIE process. This method is a single step etching method as the random surface on the fused silica substrates can be developed by the use of ICP RIE using Bosch process as described in the previous section.

The optimization of the ICP DRIE process to get the random surface structures which have the properties of high anti-reflection at a given wavelength or for a broadband is a challenging task. It requires a precise control on the etching parameters. By controlling the etching parameters, the fluxes of the ions and neutrals reaching the substrate can be controlled, which basically produces the surface structures as needed for the application.

The parameters used for the optimized etching of the fused silica optical substrates is given in the table 2.1.

Table 2.1. Etching parameters of the fused silica optical substrates

Parameter	**Passivation**	**Etching**
C_4F_8 flow (sccm)	85	0
SF_6 flow (sccm)	0	130
O_2 flow (sccm)	0	13
Cycle Time (Second)	7	9
Platen Power (Watt)	0	Variable
Coil Power (Watt)	Variable	
Chamber Pressure (mTorr)	Variable	
Etching Time (Minutes)	Variable	

There are several methods to induce random rough surface on the optical substrates. One of the conventional methods we used to induce random surface on a planar fused silica substrate was using photolithography method. This conventional method we used uses multiple steps to get random surface on the optical substrate, which is shown in figure 2.7.

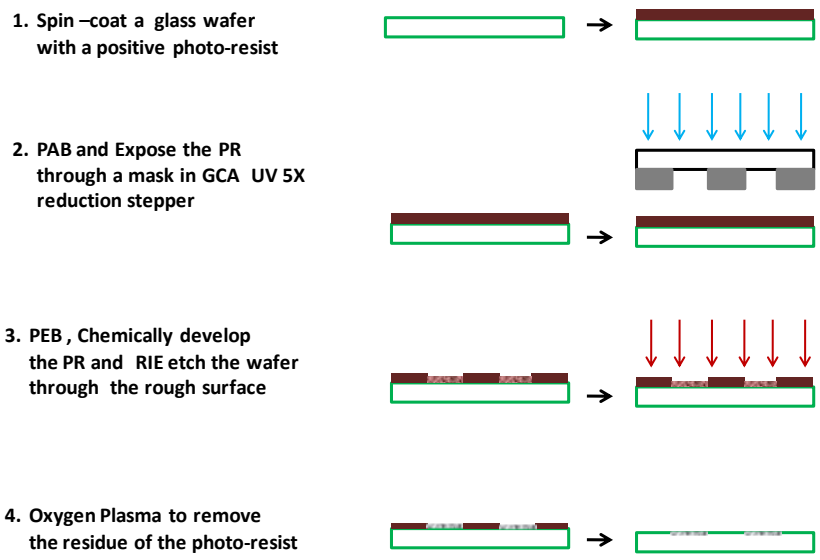

Figure 2.8. Conventional method of developing random rough surface on a fused silica substrate. This method needs many steps to achieve the goal and hence time consuming and expensive.

Another method we used to develop random anti-reflective surface structure on the planar as well as curved fused silica substrate is shown in the figure 2.8.

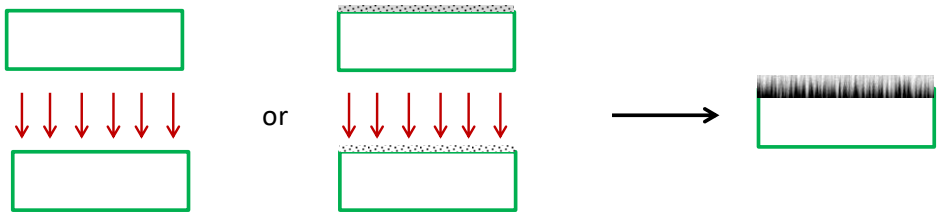

Figure 2.9. Single step etching method to achieve random rough surface on fused silica substrate using ICP RIE Bosch process.

The feature height, depth and average roughness of the random surface structures developed using this method can be controlled by varying the applied chamber pressure, platen power, coil power, etching time, gas flow rates etc.

The optimized condition was used, and the planar and curved fused silica optical substrates were etched. The transmissivity for a planar fused silica 4” wafer sample etched with optimized etching condition is shown in the figure 2.10. The transmissivity reached about 99.6% when the sample was etched on both sides [31]. The fabricated fused silica samples with optimized conditions for various wavelength region have been used in many applications [32-35].

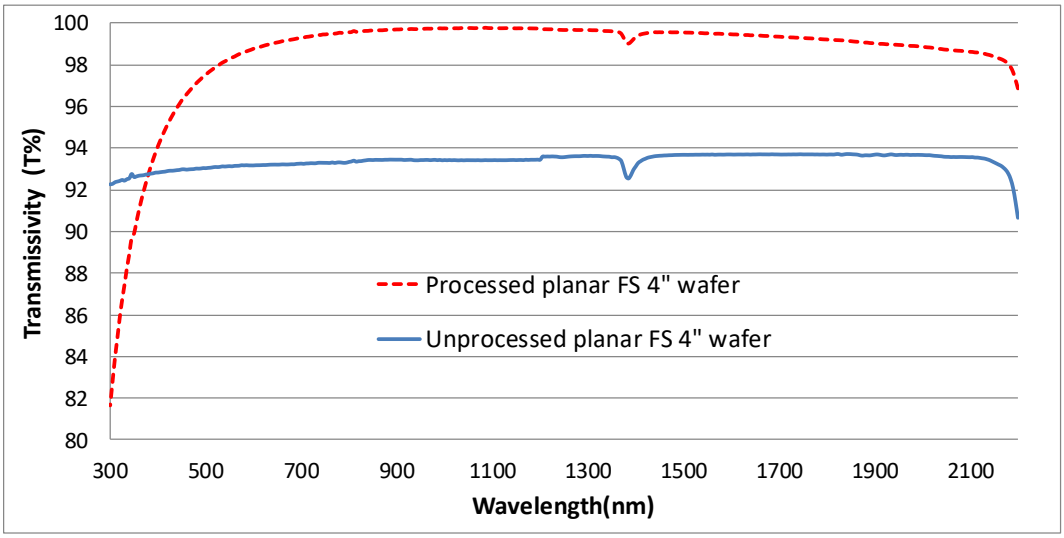

Figure 2.10. The transmissivity of the both-side processed planar fused full 4" wafer using optimized etching parameters. This shows about 99.6 % of transmissivity in a broadband wavelength range.

The top-view (5°- inclination) and side-view SEM image of one of the samples fabricated with optimized etching conditions is shown in the figure 2.11.

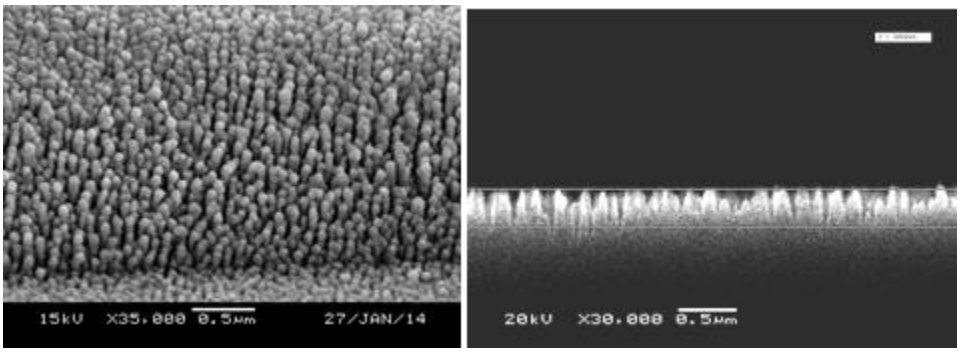

Figure 2.11. The top-view (5°- inclination) and side-view SEM image of one of the samples fabricated with optimized etching conditions.

In summary, we briefly discussed about various etching processes that are used in etching optical substrates. Then we showed a single step etching process, using Bosch process, to etch fused silica substrate to induce random anti-reflective surface structures (rARSS). This method is quicker than the conventional methods, and we can control the etching process as needed for the fabrication of rARSS on optical substrates to give the higher and broadband AR surface. We showed the result of one of the optimized etching conditions, which was used to fabricate rARSS on a planar fused silica 4" wafer. After etching both sides, it shows ~ 99.6% transmissivity in a broad wavelength region.

CHAPTER 3 FABRICATION RESULTS OF ANTI-REFLECTIVE RANDOM SURFACE STRUCTURES

3.1 Characterization of Optical Substrates

The optical substrates were etched using ICP DRIE method. The device used was Advanced Silicon Etcher (ASE). The optical substrates used for etching in our case were UV grade planar fused silica. The substrates were etched with variable etching parameters using Bosch process. The variables we used in our case were chamber pressure, coil power, platen power and etching time. When one variable was changed, the other parameters were kept at a fixed optimized value. After etching the substrates applying the method as described in chapter 2, we measured their topical structure using scanning electron microscope (SEM).

The Scanning Electron Microscope (SEM) images of the samples processed are shown in the figures 3.3, 3.4, 3.5 and 3.6 for variable parameters: chamber pressure, platen power, coil power and etching time respectively.

The chamber pressure was varied from 15 mTorr to 30 mTorr and then to 45 mTorr. The variable platen powers used for etching were 15 W, 30 W and 45 W. The variable coil powers used were 500 W, 750 W and 1000 W. The etching time was varied from 30 minutes to 60 minutes and then to 90 minutes in the etching processes. The other

parameters were kept constant at the optimized values for all the processes as shown in the table 2 of the chapter 2.

The roughness parameters: average roughness (R_a), root-mean squared roughness (R_q), total roughness (R_z) are shown in the figure 3.1, obtained from the measurement of roughness using atomic force microscope (AFM).

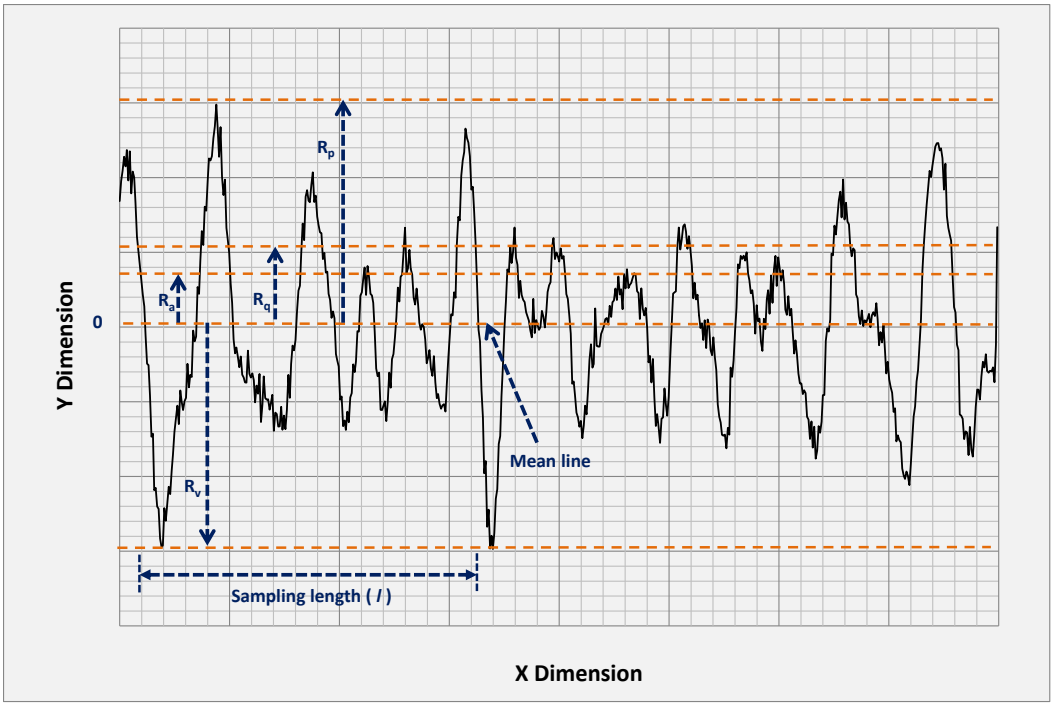

Figure 3.1. The roughness parameters: average roughness (R_a), root-mean squared roughness (R_q), total roughness (R_z).

The average roughness (Ra) and the root-mean squared roughness (Rq) are given by

$$R_a = \frac{1}{l} \int_0^l |y| dx$$

$$R_q = \sqrt{\frac{1}{l} \int_0^l y^2 dx}$$

The total roughness (Rz) is the sum of peak roughness (Rp) and valley roughness (Rv), where peak and valley roughness are the positive maximum and minimum values of the roughness [36], which are shown in the figure 3.1.

$$R_z = R_p + R_v$$

The skewness and kurtosis give the characteristic signature of the rough structures formed on the surface [37].

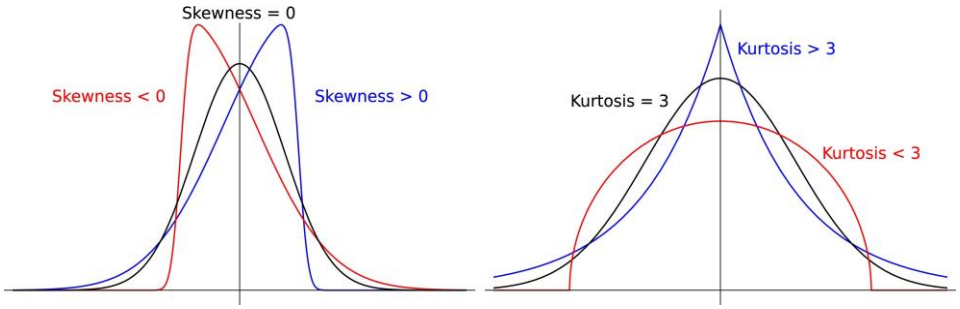

Figure 3.2. Figure depicting the skewness and kurtosis of a surface. These parameters give the characteristic signature of the rough surface.

At first the chamber pressure was varied and the change in the surface structures, roughness, surface profile, and the transmissivity were measured. The surface profile is shown in the figure 3.3 as taken by scanning electron microscope (SEM).

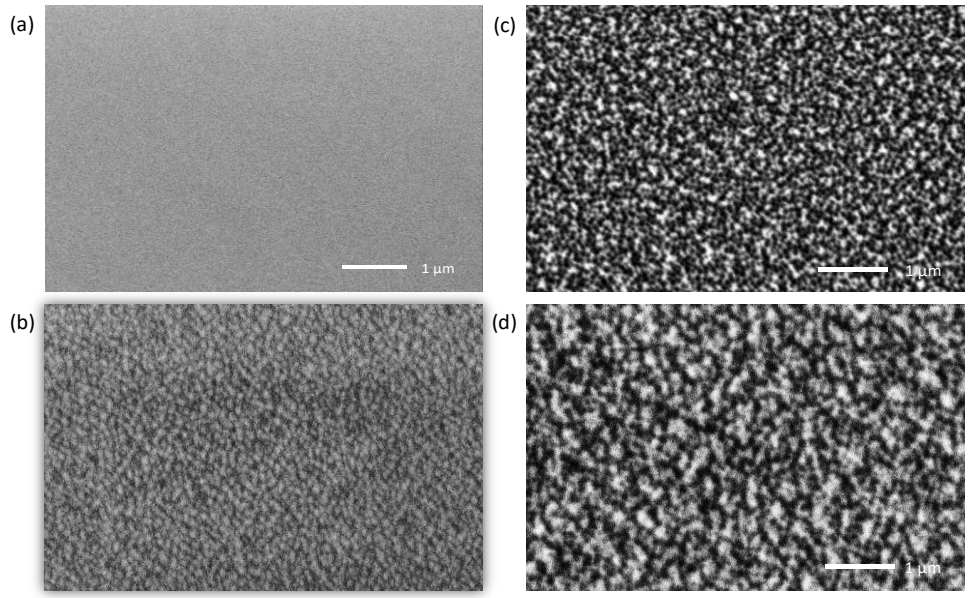

Figure 3.3. Unprocessed and processed samples with varying chamber pressure. The figure 3.3(a) shows the unprocessed sample and 3.3(b), 3.3(c), and 3.3(d) show the SEM images of the samples processed at 15 mTorr, 30 mTorr and 45 mTorr respectively.

The average roughness (R_a), root-mean squared roughness (R_q), total roughness (R_z), Skewness (R_{sk}) and Kurtosis (R_{ku}) were measured for the samples fabricated with varying chamber pressure. The values are tabulated in 3.1.

Table 3.1. Change in roughness parameters with change in processing chamber pressure

Sample	Roughness				
	R_a (nm)	R_q(nm)	R_z(nm)	R_{sk}	R_{ku}
Unprocessed	3.5	4.4	30.1	0.06	2.97
Processed (15 mTorr)	22.61	28.02	153.14	0.17	2.57
Processed (30 mTorr)	121.88	151.35	780.18	0.08	2.72
Processed (45 mTorr)	148.32	183.07	1007.26	0.07	2.77

Then the platen power was varied and the change in the surface structures, roughness, surface profile, and the transmissivity were measured. The surface profile is shown in the figure 3.4 as taken by scanning electron microscope (SEM).

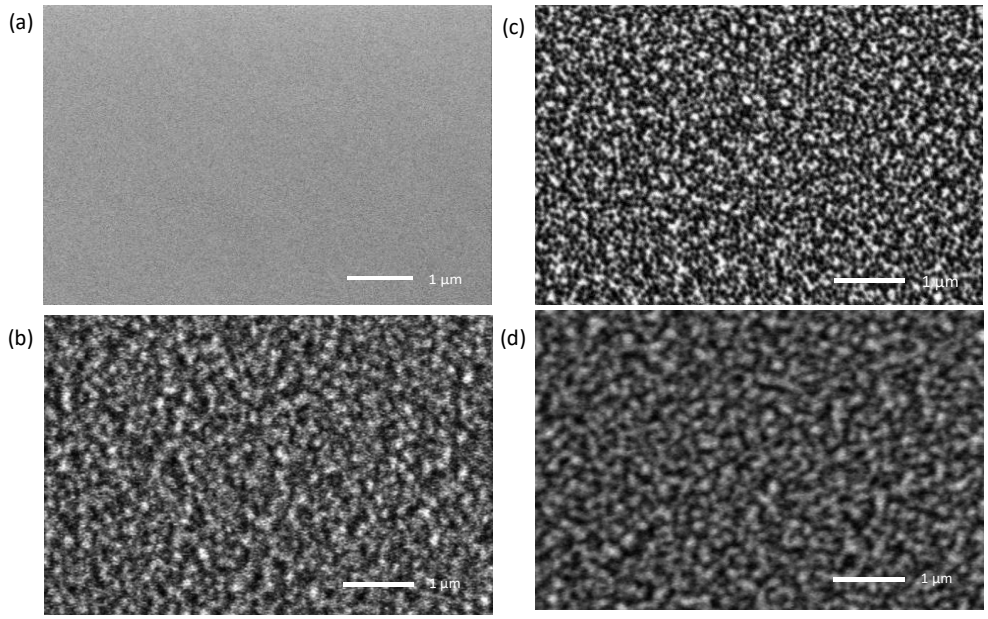

Figure 3.4. Unprocessed and processed samples with varying platen power. The figure 3.4(a) shows the unprocessed sample and 3.4(b), 3.4(c), and 3.4(d) show the SEM images of the samples processed at 15 Watt, 30 Watt and 45 Watt respectively.

The average roughness (R_a), root-mean squared roughness (R_q), total roughness (R_z), Skewness (R_{sk}) and Kurtosis (R_{ku}) were measured for the samples fabricated with varying platen power. The values are tabulated in 3.2.

Table 3.2. Change in roughness parameters with change in platen power

Sample	Roughness				
	R_a (nm)	R_q(nm)	R_z(nm)	R_{sk}	R_{ku}
Unprocessed	3.5	4.4	30.1	0.06	2.97
Processed (15 Watt)	98.52	119.72	633.71	-0.09	2.40
Processed (30 Watt)	121.88	151.35	780.18	0.08	2.72
Processed (45 Watt)	149.29	187.47	1007.59	0.13	2.30

Next the platen power was varied and the change in the surface structures, roughness, surface profile, and the transmissivity were measured. The surface profile is shown in the figure 3.5 as taken by scanning electron microscope (SEM).

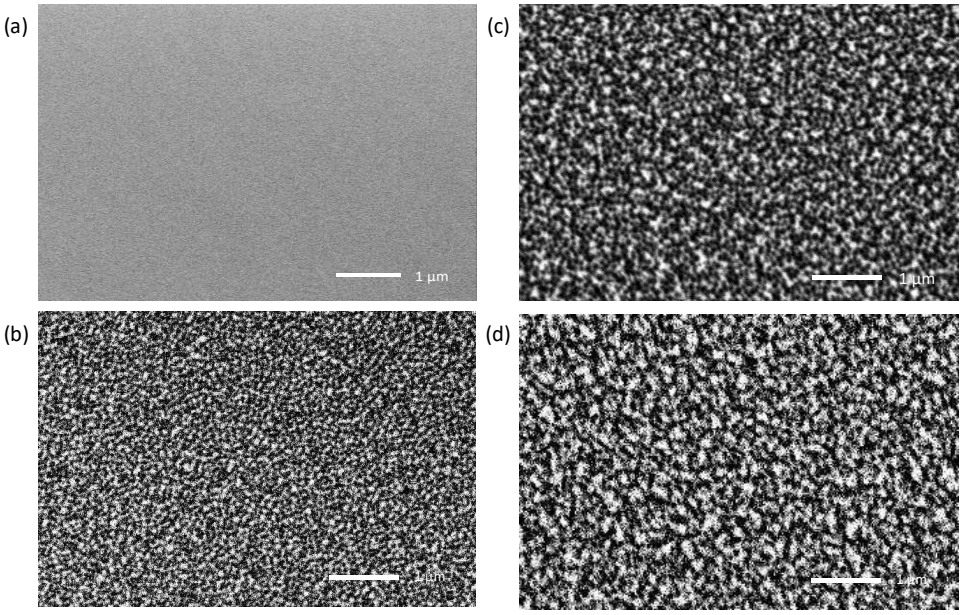

Figure 3.5. Unprocessed and processed samples with varying coil power. The figure 3.5(a) shows the unprocessed sample and 3.5(b), 3.5(c), and 3.5(d) show the SEM images of the samples processed at 500 Watt, 750 Watt and 1000 Watt respectively.

The average roughness (R_a), root-mean squared roughness (R_q), total roughness (R_z), Skewness (R_{sk}) and Kurtosis (R_{ku}) were measured for the samples fabricated with varying coil power. The values are tabulated in 3.3.

Table 3.3. Change in roughness parameters with change in coil power

Sample	Roughness				
	R_a (nm)	R_q(nm)	R_z(nm)	R_{sk}	R_{ku}
Unprocessed	3.5	4.4	30.1	0.06	2.97
Processed (500 Watt)	91.34	113.51	608.45	-0.21	2.91
Processed (750 Watt)	121.88	151.35	780.18	0.08	2.72
Processed (1000 Watt)	152.75	192.08	948.56	0.35	2.95

Finally, the etching time was varied and the change in the surface structures, roughness, surface profile, and the transmissivity were measured. The surface profile is shown in the figure 3.6 as taken by scanning electron microscope (SEM).

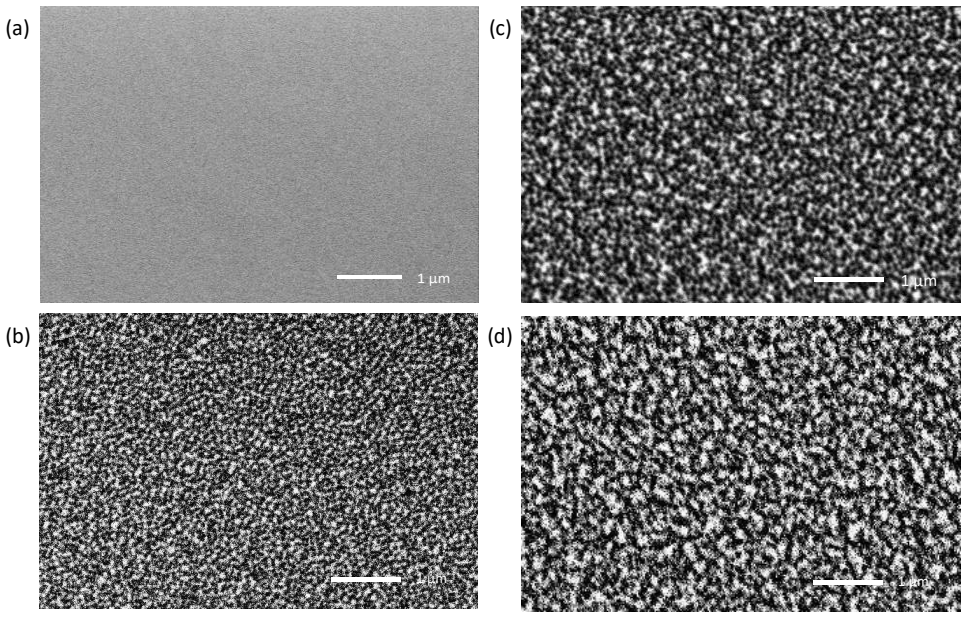

Figure 3.6. Unprocessed and processed samples with varying etching time. The figure 3.6(a) shows the unprocessed sample and 3.6(b), 3.6(c), and 3.6(d) show the SEM images of the samples processed for 30 minutes, 60 minutes and 90 minutes respectively.

The average roughness (R_a), root-mean squared roughness (R_q), total roughness (R_z), Skewness (R_{sk}) and Kurtosis (R_{ku}) were measured for the samples fabricated with varying coil power. The values are tabulated in 3.4.

Table 3.4. Change in roughness parameters with change in etching time

Sample	**Roughness**				
	R_a (nm)	**R_q(nm)**	**R_z(nm)**	**R_{sk}**	**R_{ku}**
Unprocessed	3.5	4.4	30.1	0.06	2.97
Processed (30 Minute)	39.65	49.79	267.59	0.27	2.93
Processed (60 Minute)	121.88	151.35	780.18	0.08	2.72
Processed (90 Minute)	139.06	168.76	907.52	0.38	2.69

3.2 Surface Profile Characterization of the Etched Samples

The etched samples had different surface profile with the change in the etching parameters. The fill factor of the surfaces at different heights from the bottom of the etched surface was taken using LEXT confocal microscope. The figures 3.7, 3.8, 3.9 and 3.10 show the surface profiles of the processed samples. The horizontal axis shows the net depth of the samples from the ambient and the vertical axis shows the fill factor ratio of the substrate (fused silica) with respect to the air.

First the surface profiles of the samples processed at various chamber pressures are shown in figure 3.7. As the chamber pressure increases, the ion density increases, and we expect that the etch rate increases with the increase in the chamber pressure.

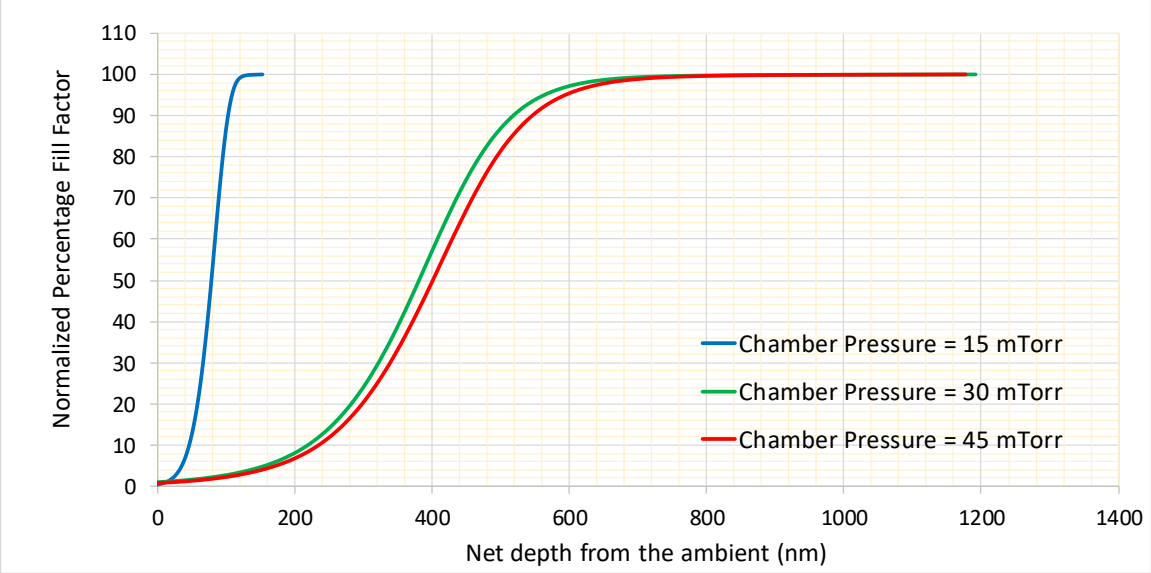

Figure 3.7. The variation of the percentage fill factor of the substrate with the height of the surface for variable chamber pressure.

The material/void fraction percentage at each height of the fabricated samples with variable chamber pressure are summarized in the table 3.5 taking only 10 values from 0 to 100% material left after etching:

Table 3.5. Substrate material left after etching at distance of the layer from ambient at the variable chamber pressure

Substrate material left after etching (%)	Distance of the layer from ambient (nm) at the variable chamber pressure		
	15 mTorr	30 mTorr	45 mTorr
0	0	0	0
10	45.48	217.98	233.59
20	57.70	281.45	297.21
30	65.97	321.78	338.53
40	72.46	353.07	371.26
50	78.21	380.76	400.57
60	83.61	407.50	428.66
70	89.02	435.71	458.39
80	94.95	469.11	493.50
90	102.60	518.03	545.43
100	153.14	780.21	820.21

This analysis shows that as the chamber pressure increases, the etched depth also increases. Also, the material/void ratio changes smoothly as the chamber pressure goes on increasing.

Next the surface profiles of the samples processed at various platen power are shown in figure 3.8. As the platen power increases, the reactive ions reaching the substrate increases and impinge with higher energies, and we expect that the etch rate increases with the increase in the platen power.

The material/void fraction percentage at each height of the fabricated samples with variable platen power are summarized in the table 3.6 taking only 10 values from 0 to 100% material left after etching.

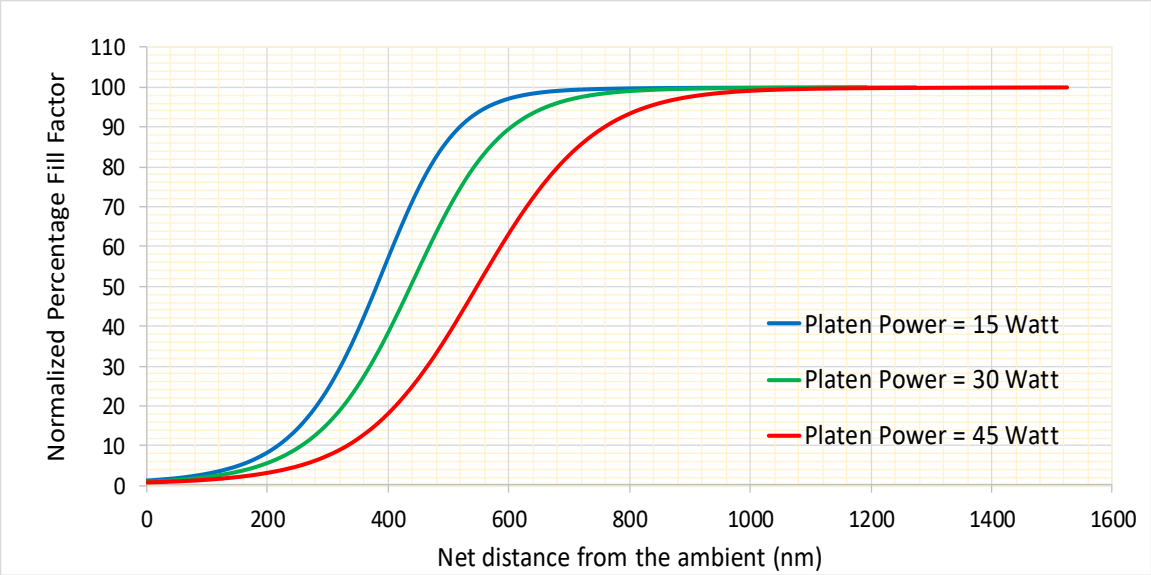

Figure 3.8. The variation of the percentage fill factor of the substrate with the height of the surface for variable platen power

Table 3.6. Substrate material left after etching at distance of the layer from ambient at the variable platen power

Substrate material left after etching (%)	Distance of the layer from ambient (nm) at the variable platen power		
	15 Watt	30 Watt	45 Watt
0	0	0	0
10	217.98	257.39	334.37
20	281.45	326.37	413.76
30	321.78	370.65	466.68
40	353.07	405.71	509.43
50	380.76	437.34	548.48
60	407.50	468.36	587.81
70	435.71	501.87	630.51
80	469.11	542.36	682.30
90	518.03	603.75	759.13
100	1191.94	1274.12	1526.09

This analysis shows that as the platen power increases, the etched depth also increases. The slope of the material/void ratio goes larger with increasing the platen power.

Then the surface profiles of the samples processed at various coil power are shown in figure 3.9. As the coil power increases, the number of reactive species increases, and thus we expect the etch rate increase with the increase in the coil power.

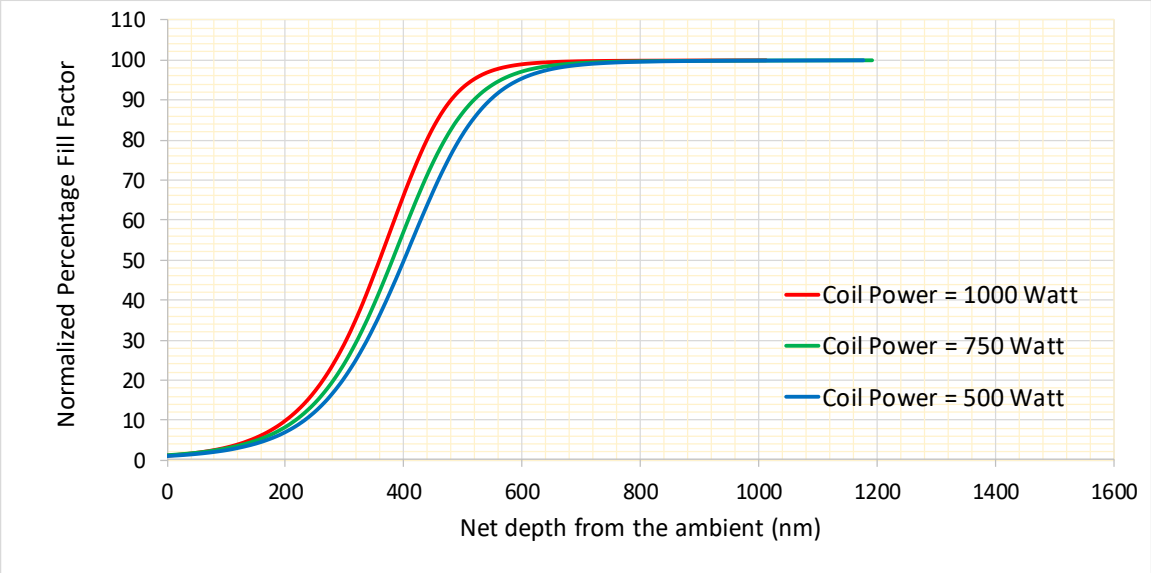

Figure 3.9. The variation of the percentage fill factor of the substrate with the height of the surface for variable coil power

The material/void fraction percentage at each height of the fabricated samples with variable coil power are summarized in the table 3.7 taking only 10 values from 0 to 100% material left after etching.

This analysis shows that as the coil power increases, the etched depth also increases. The slope of the material/void ratio goes larger with increasing the coil power. However, the slope of the profile of sample etched goes smaller with increase in the chamber pressure, which is most probably caused because the directionality of the ions increases with increase in the coil power and hence the profile becomes more anisotropic (i.e. less slope of the profile) with increase in the coil power.

Finally, the surface profiles of the samples processed at various etching time are shown in figure 3.10. As the etching time increases, the number of reactive species impinging on

the substrate significantly increase, and thus we expect the etch rate increase with the increase in the etching time.

Table 3.7. Substrate material left after etching at distance of the layer from ambient at the variable coil power

Substrate material left after etching (%)	Distance of the layer from ambient (nm) at the variable coil power		
	500 Watt	750 Watt	1000 Watt
0	0	0	0
10	201.43	217.98	347.75
20	263.48	281.45	428.81
30	302.82	321.78	482.94
40	332.73	353.07	527.33
50	358.85	380.76	568.21
60	383.84	407.50	608.59
70	409.48	435.71	652.79
80	438.56	469.11	705.35
90	479.20	518.03	782.77
100	722.14	791.94	826.97

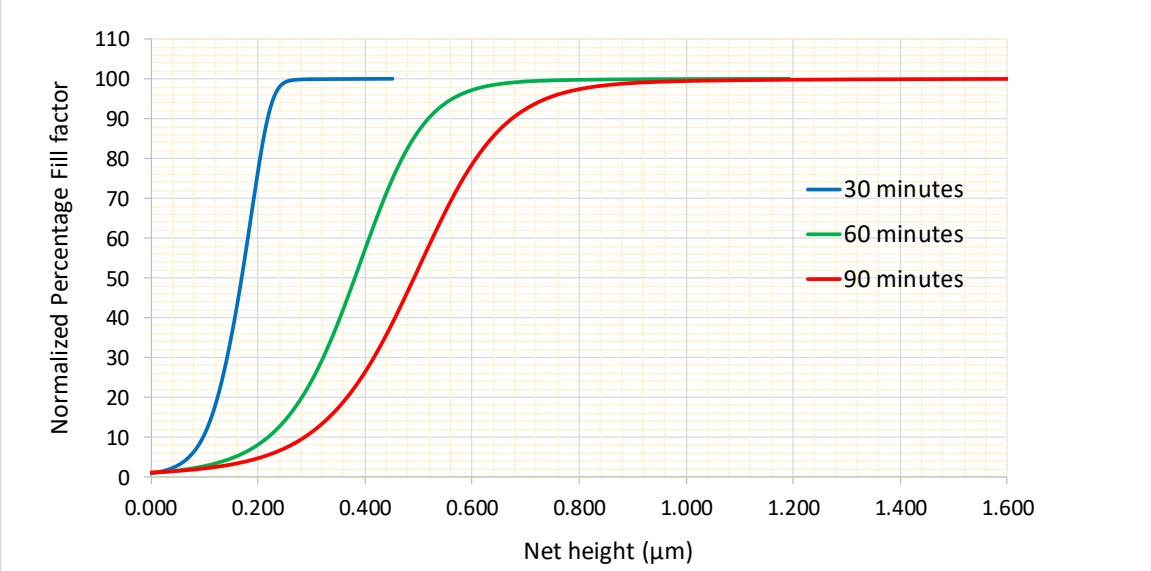

Figure 3.10. The variation of the percentage fill factor of the substrate with the height of the surface for variable etching time.

The material/void fraction percentage at each height of the fabricated samples with variable etching time are summarized in the table 3.8 taking only 10 values from 0 to 100% material left after etching.

Table 3.8. Substrate material left after etching at distance of the layer from ambient at the variable etching time

Substrate material left after etching (%)	Distance of the layer from ambient (nm) at the variable Etching Time		
	30 minutes	60 minutes	90 minutes
0	0	0	0
10	97.98	257.39	285.56
20	125.11	326.37	365.49
30	143.21	370.65	416.19
40	157.70	405.71	455.79
50	170.38	437.34	491.26
60	181.95	468.36	525.86
70	193.13	501.87	562.63
80	204.75	542.36	607.24
90	218.91	603.75	674.33
100	282.21	770.12	1001.01

This analysis shows that as the etching time increases, the etched depth increases. The slope of the material/void ratio decreases with increasing the etching time.

3.3 Transmission Enhancement with Variable Parameters

The transmission enhancement was measured using Varian Cary 5000 UV-Vis-NIR Spectrophotometer. The resolution of this spectrometer is ±0.1nm in UV-Vis region and ±0.4nm in infrared region. The wavelength chosen to measure the enhancement was from 300nm to 2200nm. All the measurements were taken at normal angle of incidence. A basic schematic for the measurement of the transmissivity of the planar fused silica sample is shown in the figure 3.11.

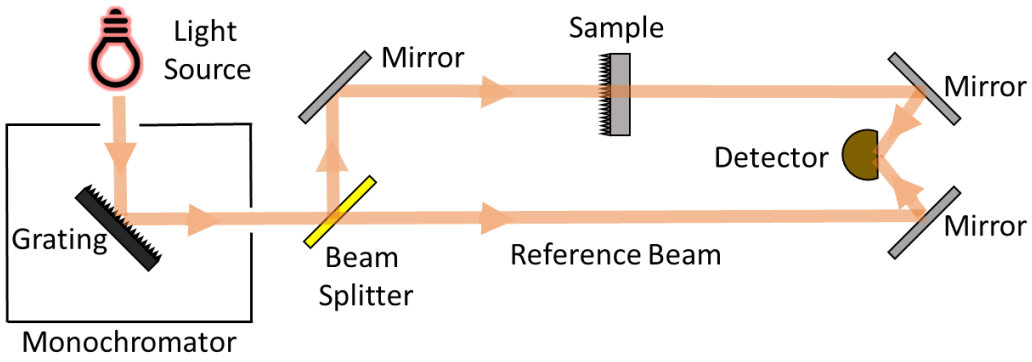

Figure 3.11. Schematic diagram of the spectrophotometer. The sample was put normal to input beam direction and the etched surface facing the incoming beam (in case of one-side etched samples).

The transmission enhancement was measured using Varian Cary 5000 UV-Vis-NIR Spectrophotometer. The resolution of this spectrometer is ±0.1nm in UV-Vis region and ±0.4nm in infrared region.

The spectral transmittivity at normal incidence was measured from 300 nm to 2200 nm in an increment of 5 nm. The measured spectral transmittances were used to calculate the rARSS transmission enhancement (η) by using the formula below:

$$\eta = \left(\frac{t_p}{t_u} - 1\right) \times 100\% \qquad (3.1)$$

where, t_p and t_u are the measured transmittances through the processed and unprocessed surfaces respectively.

First the transmissivity and then the transmittance enhancement of the samples processed at various chamber pressures are shown in figure 3.12. As the chamber pressure increases, the etch depth increases, and we expect that the maximum transmissivity red shifts with the increase in the chamber pressure.

We see from the figures 3.12 (a) and 3.12 (b) that the transmissivity red shift with the increase in chamber pressure, and also the higher transmissivity is observed in larger band.

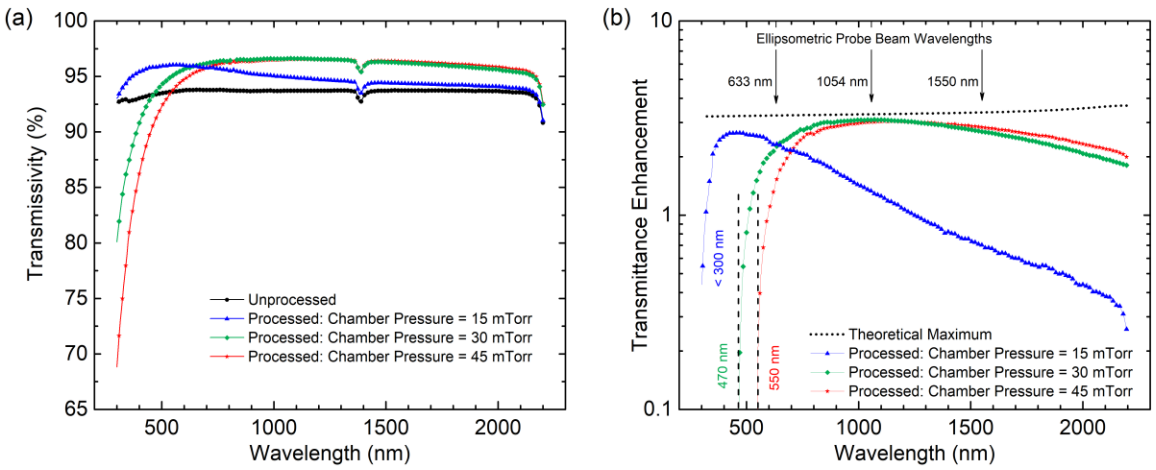

Figure 3.12. Transmissivity of the unprocessed and processed samples with varying chamber pressure

Next the transmissivity and then the transmittance enhancement of the samples processed at various platen powers are shown in figure 3.13. As the platen power increases, the etch depth increases, and we expect that the maximum transmissivity red shifts with the increase in the platen power.

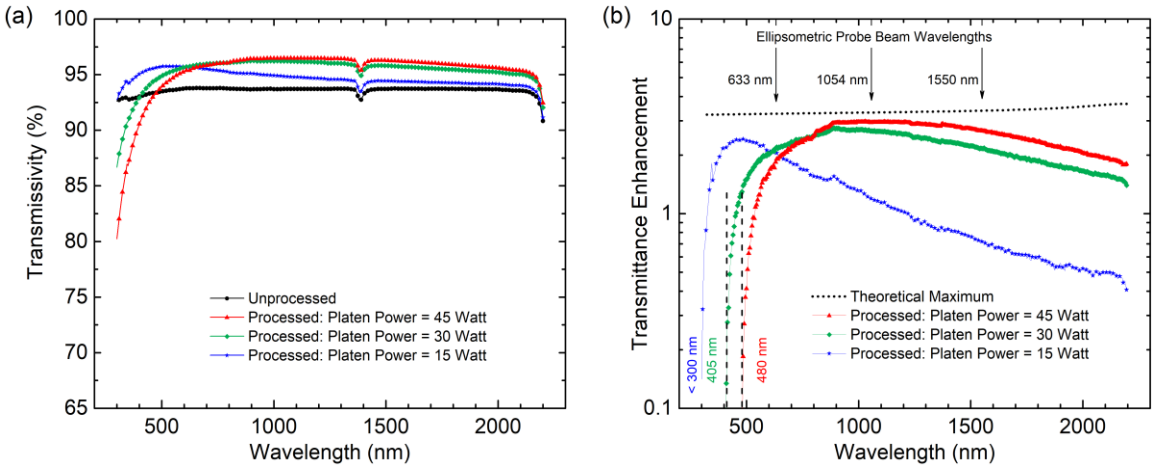

Figure 3.13. Transmissivity of the unprocessed and processed samples with varying platen power.

We see from the figures 3.13 (a) and 3.13 (b) that the transmissivity red shift with the increase in platen power, and also the higher transmissivity is observed in larger band.

Then the transmissivity and then the transmittance enhancement of the samples processed at various coil powers are shown in figure 3.14. As the coil power increases, the etch depth increases, and we expect that the maximum transmissivity red shifts with the increase in the coil power.

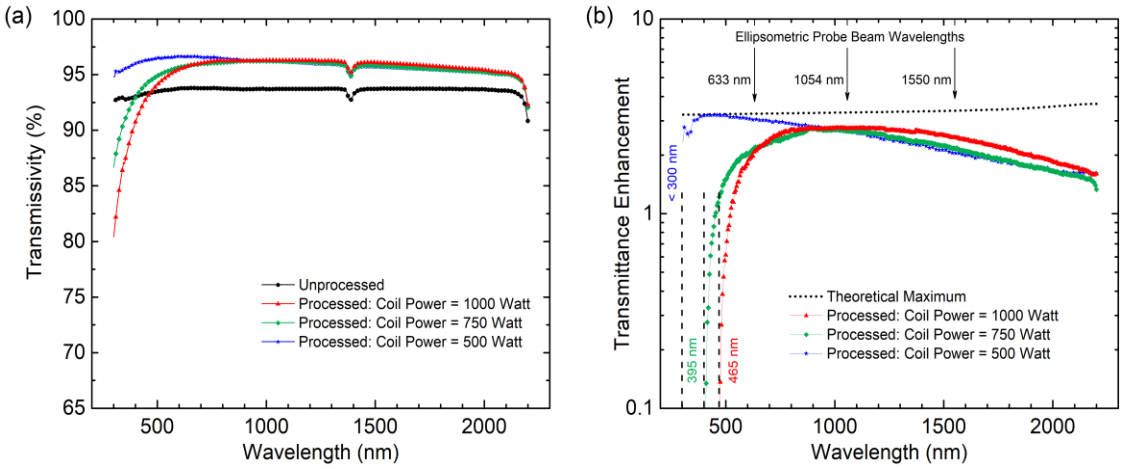

Figure 3.14. Transmissivity of the unprocessed and processed samples with varying coil power.

We see from the figures 3.14 (a) and 3.14 (b) that the transmissivity red shift with the increase in coil power, and also the higher transmissivity is observed in larger band.

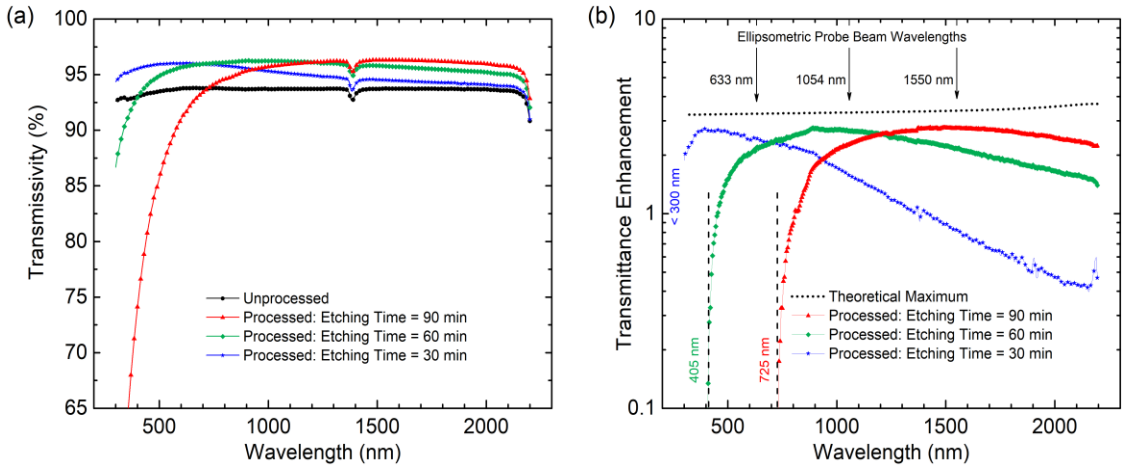

Figure 3.15. Transmissivity of the unprocessed and processed samples with varying etching time

Finally, the transmissivity and then the transmittance enhancement of the samples processed at various etching times are shown in figure 3.15. As the etching time increases, the etch depth increases, and we expect that the maximum transmissivity red shifts with the increase in the etching time.

We see from the figures 3.15 (a) and 3.15 (b) that the transmissivity red shift with the increase in etching time, and also the higher transmissivity is observed in larger band.

The increase in the transmittance and the threshold wavelength above which the transmittance starts to increase is tabulated in table 3.9.

Table 3.9. Cut-off wavelengths corresponding to processed planar fused silica sample

Processing parameters	Parameter values	Cut-off wavelengths (nm)
Chamber Pressure	15 mTorr	< 300
	30 mTorr	470
	45 mTorr	550
Coil Power	500 Watt	< 300
	750 Watt	395
	1000 Watt	465
Platen Power	15 Watt	< 300
	30 Watt	405
	45 Watt	480
Etching Time	30 minutes	< 300
	60 minutes	405
	90 minutes	725

We see that the threshold wavelength increases with increase in the chamber pressure, coil power, platen power, and etching time.

3.4 Fabrication of Anti-Reflective Surface on Fused Silica from Visible to Short-Wave Infrared Spectral Band

The highly transmissivity enhanced random-structured anti-reflection surfaces were fabricated on plane fused silica substrate. The transmissivity region can be which are tailored to shift from Visible to NIR or SWIR using an optimized reactive-ion etching fabrication process. Because of the high transmissivity and the angular independency in the transmission, this novel material is a considered to work very well in the Visible, NIR and SWIR spectral regions for non-imaging applications [33].

We processed the fused silica substrates at various chamber pressures using the Bosch process[38] in an STS Advanced Silicon Etcher (ASE), using an inductively-coupled plasma deep reactive ion etch (ICP DRIE) technique, to restructure the surface of optical-grade planar fused silica substrates. It induces a random, sub-wavelength, nanoscale topography on the surfaces which behaves as a gradient index film with anti-reflective properties. These surface structures are usually referred to as random anti-reflective surface structures (rARSS). The resulting surface structure depends on the etching parameters of the ICP-RIE process used. The etching process consisted of two cycles: (a) an etching cycle using sulfur-hexafluoride (SF_6) and oxygen (O_2) and, (b) a passivation cycle using freon (C_4F_8) gas [39-41]. The nanoscale random structures formed on the resulting surface depend on the processing parameters. The main processing variables are gas flow rates, chamber pressure, coil power, platen power and total etching time. The change in these processing parameters changes the anisotropic etching of the material by the change in the

number of positive ions and reactive neutral atoms impinging perpendicularly on the surface of the material [28]. As a result, the average roughness (R_a) of the random surface formed on the substrate and the average diameter of the random nanostructures can be modified and the refractive index of the surface changes going from the air to the substrate.

The surface spectral transmittance was measured through the rARSS on the fused silica substrates at 550nm, 885nm and 1280nm at normal incidence using a Cary 5000 spectrometer, to establish trends in transmission enhancement. The data was collected for wavelengths from 300 nm to 2200 nm at 5 nm wavelength intervals. The measured spectral transmittances were used to calculate the rARSS transmission enhancement (η) by using the formula (3.1).

The maximum possible theoretical transmittance enhancement through a one-side processed fused silica single surface is about 3.1% to 3.5%, in the 300 nm to 2200 nm spectral region. The figure 3.16 shows the transmission enhancements in the three values 550nm, 885nm and 1280nm. The sample A had the highest enhancement of the transmissivity at 550 nm, sample B had the highest transmissivity at 885 nm, and the sample C had the highest transmissivity at 1280 nm.

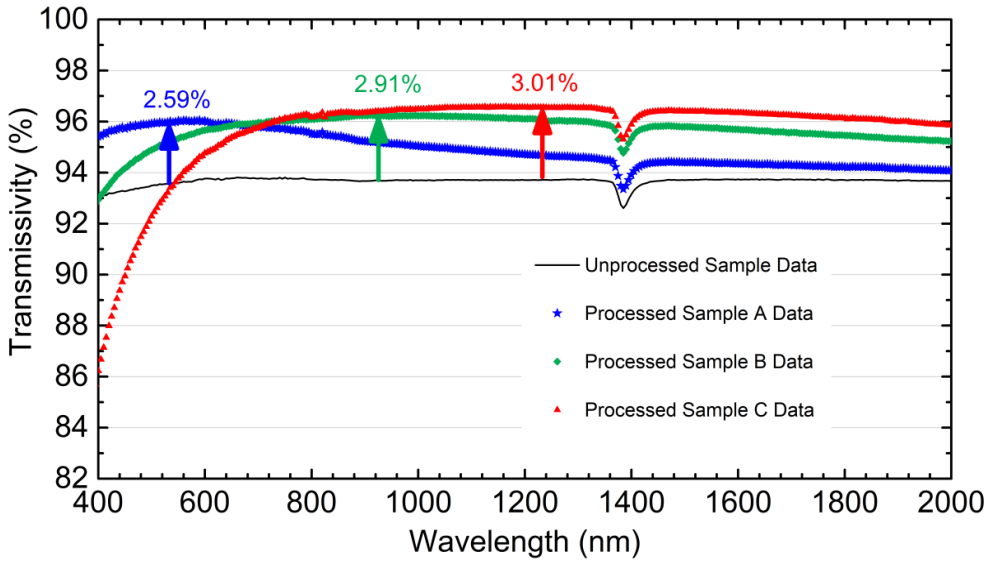

Figure 3.16. The transmissivity of the three samples processed with three different optimized processes and their transmissivity enhancements at three different spectral regions

The figures 3.17, 3.18 and 3.19 show the transmissivity enhancement of the fabricated planar fused silica samples A, B and C at the wavelengths 550nm, 885 nm and 1280 nm respectively.

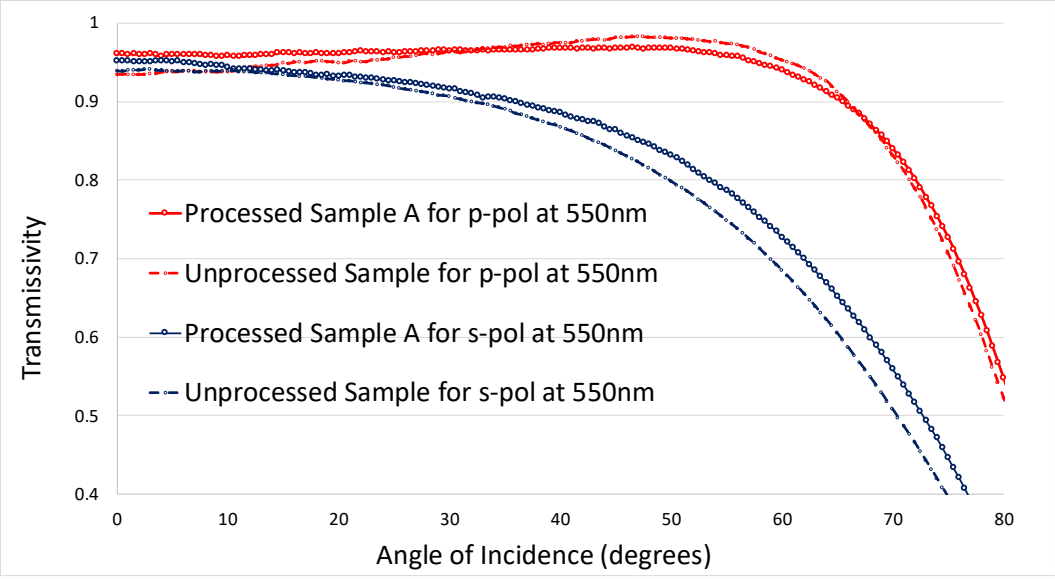

Figure 3.17. The ellipsometric measurement on sample A showing the transmissivity enhancement of both s- and p-polarized beam at 550 nm.

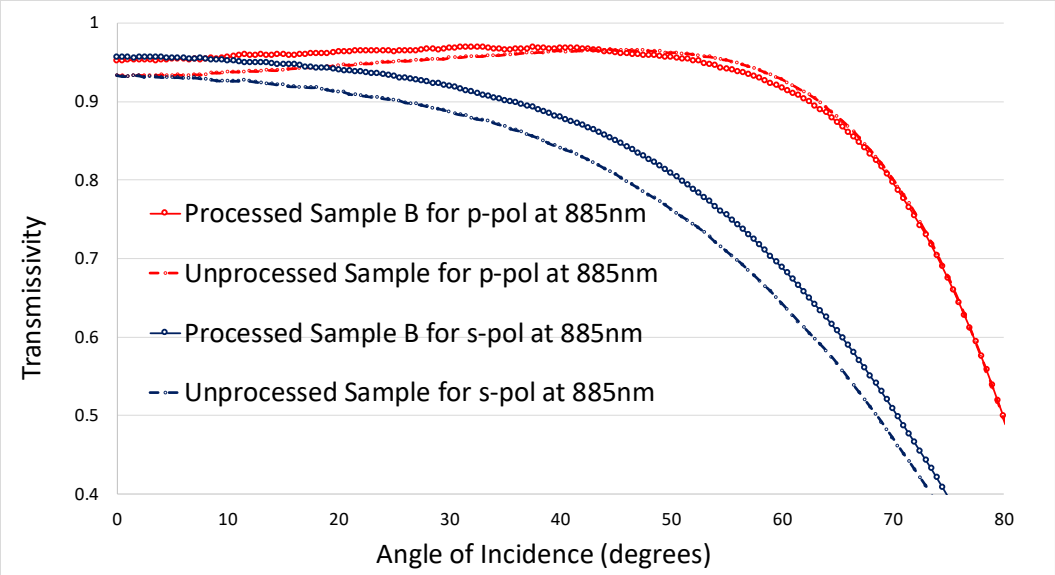

Figure 3.18. The ellipsometric measurement on sample B showing the transmissivity enhancement of both s- and p-polarized beam at 885 nm.

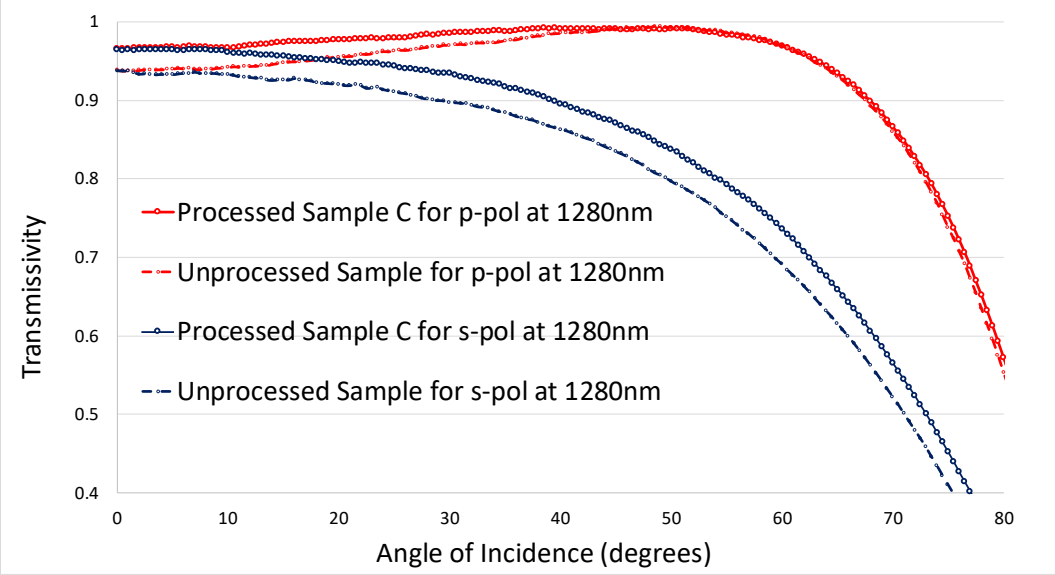

Figure 3.19. The ellipsometric measurement on sample B showing the transmissivity enhancement of both s- and p-polarized beam at 885 nm.

They all show that the transmissivity of both s- and p- polarized light is enhanced and it is angle-independent for a large angle of incidence.

The table 3.10 shows the average roughness of the processed samples and their maximum transmissivity enhancements at 550nm, 885nm and 1280nm.

Table 3.10. Roughness and transmissivity enhancement of three fabricated samples

Sample	Average Roughness (R_a)	Maximum Transmissivity Enhancement
A	22.61 nm	2.59 % at 550nm
B	121.88 nm	2.91 % at 885nm
C	148.32 nm	3.01% at 1280nm

This shows that the transmissivity enhancement shifts in the higher wavelength region as the average roughness increases.

3.5 Ellipsometric Characterization of the Random Anti-Reflective Surface Structures

Fresnel reflection at the interface between two dielectrics can be suppressed by either using thin film interference effects or by decreasing the abrupt changes between their refractive indices. The former can be achieved by coating the dielectric with a single layer or multiple layers of suitable dielectric thin films, and the latter by restructuring the surface of the dielectric to induce an effective gradient refractive index between the two optical media layers [4, 32, 42, 43]. The amplitude of the normalized transmittance through such a random anti-reflection planar surface has been measured to be almost unity for incidence angles from 0 to ±30 degrees [32, 44, 45]. However, the phase shift of the reflected light from the rARSS as a function of the angle of incidence has not been investigated to date, to the best of our knowledge. This research can be helpful in understanding and controlling the phase shift by changing the processing parameters.

We processed the fused silica substrates at chamber pressures of 15 mTorr, 30 mTorr and 45 mTorr using the Bosch process [38] in an STS Advanced Silicon Etcher, using an inductively-coupled plasma deep reactive ion etch (ICP DRIE) technique, to restructure the surface of optical-grade planar fused silica substrates. It induces a random, sub-wavelength, nanoscale topography on the surfaces which behaves as a gradient index film with anti-reflective properties. These surface structures are usually referred to as random anti-reflective surface structures (rARSS). The resulting surface structure depends on the etching parameters of the ICP-DRIE process used. The etching process consisted of two cycles: (a) an etching cycle using sulfur-hexafluoride (SF_6) and oxygen (O_2) and, (b) a passivation cycle using freon (C_4F_8) gas [39]. During the etching cycle, SF_6 gas is admitted into the chamber and dissociated into a mixture of fluorine and sulfur ions. These ions are accelerated to the surface of the substrate. Fluorine ions react with the Si atoms on the fused silica surface. During the passivation cycle, the platen power is kept very low and C_4F_8 gas enters the chamber. This gas deposits on the activated surface created during the etching cycle. In the following etching cycle, the fluorine ions react with Si and oxygen reacts with C atoms present on the surface from the passivation cycle. During the etching cycles, the volatile gaseous byproducts, silicon tetrafluoride (SiF_4) and carbon monoxide and carbon dioxide (CO, CO_2) are pumped out, leaving the etched surface behind. Similar processes have been reported by others to induce random roughness on fused silica surfaces [11, 14]. The nanoscale random structures formed on the resulting surface depend on the processing parameters. The main processing variables are gas flow rates, chamber pressure, coil power, platen power and total etching time. The surface-ion reaction time inside the chamber depends on the ion dwelling and residence time. The increase in the processing

chamber pressure increases the anisotropic etching of the material by the increased number of positive ions and reactive neutral atoms impinging perpendicularly on the surface of the material [28]. By varying this parameter, the maximum depth of the surface roughness (R_z) and the average diameter of the random nanostructures can be modified.

We measured the spectroscopic transmittance through the rARSS on the fused silica substrates, as a function of ICP-RIE processing chamber pressure. The substrate spectral transmittance was measured at normal incidence using a Cary 5000 spectrometer. The transmission data was collected for wavelengths from 300 nm to 2200 nm at 5 nm wavelength intervals. The measured spectral transmittance was used to calculate the rARSS transmission enhancement calculated using formula (3.1), between the processed samples and an unprocessed fused silica substrate.

Thus, if the processed surface measured transmittance was lower than the unprocessed corresponding value, the transmittance enhancement resulted in a negative normalized fraction, whereas if the processed surface measured transmittance was higher, the enhancement was a positive normalized fraction. This allows us to express the increase in transmittance due to the anti-reflective property of the rARSS in a normalized-ratio difference to the Fresnel interface transmittance as in figure 3.20.

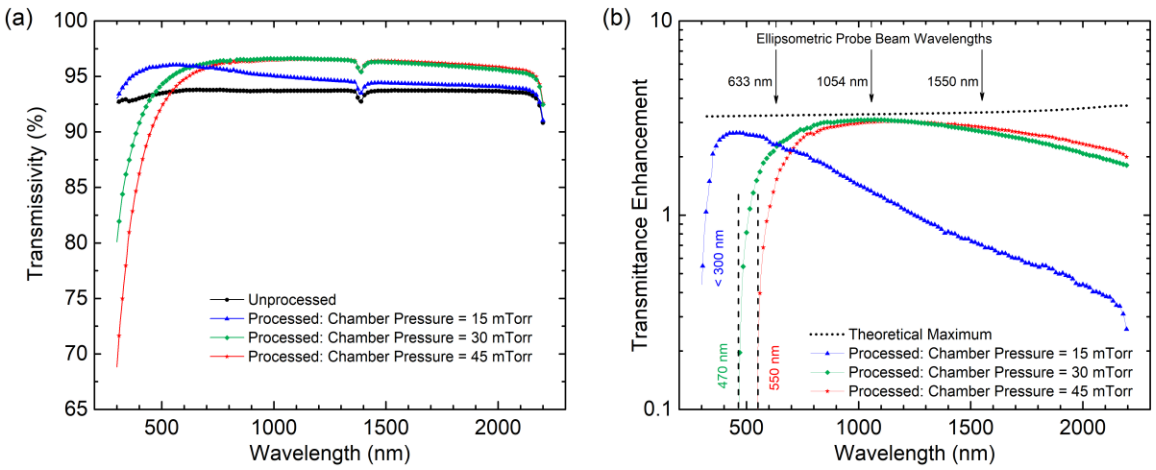

Figure 3.20. Measured normal incidence transmittance enhancement from one-side processed fused silica substrates at different processing chamber pressures. The theoretical maximum transmittance enhancement for a single surface is also shown for comparison. At lower chamber process pressures, the transmittance enhancement peak blue shifts and the maximum enhancement bandwidth decreases. The ellipsometric test wavelengths are shown with the arrow markers for reference. The dashed vertical asymptotes indicate the enhancement cutoff wavelength.

The maximum possible theoretical transmittance enhancement through a fused silica single surface is about 3.1% to 3.5%, in the 300 nm to 2200 nm spectral region.

The samples processed at chamber pressures of 30 mTorr and 45 mTorr have an enhanced transmission of about 3% for a broadband region from 1000 nm to 1300 nm, where the ideal maximum transmittance enhancement is about 3.22% indicating the transmission of the rARSS single surface is 99.7%. The enhancement cutoff wavelength in figure 3.20 is the wavelength below which there is no enhancement in transmittance. At lower processing chamber pressures, the enhancement cutoff wavelength decreases (blue shifts), as indicated by the trend of the dashed vertical asymptotes in the figure 3.20.

The physical characteristics, viz. maximum roughness (R_z), and lateral feature diameter, of the random rough surfaces were measured in order to relate them to the measured optical performance for each sample. The maximum roughness (R_z) of each

processed sample was obtained using a Dimension 3100 Scanning Probe Microscopy (SPM) system with a nanoscope IV SPM controller, atomic force microscope (AFM) manufactured by VEECO. A high aspect ratio needle was used for higher accuracy. Scanning electron microscope images (SEM) were obtained at normal viewing conditions, and granulometry was used on the SEM images of the etched surface, to obtain the feature diameter size distribution from multiple locations on each processed substrate. The average feature diameters, transmittance cutoff wavelengths, and the average maximum depths of the processed substrates all increase with higher processing chamber pressures, as shown in figure 3.21.

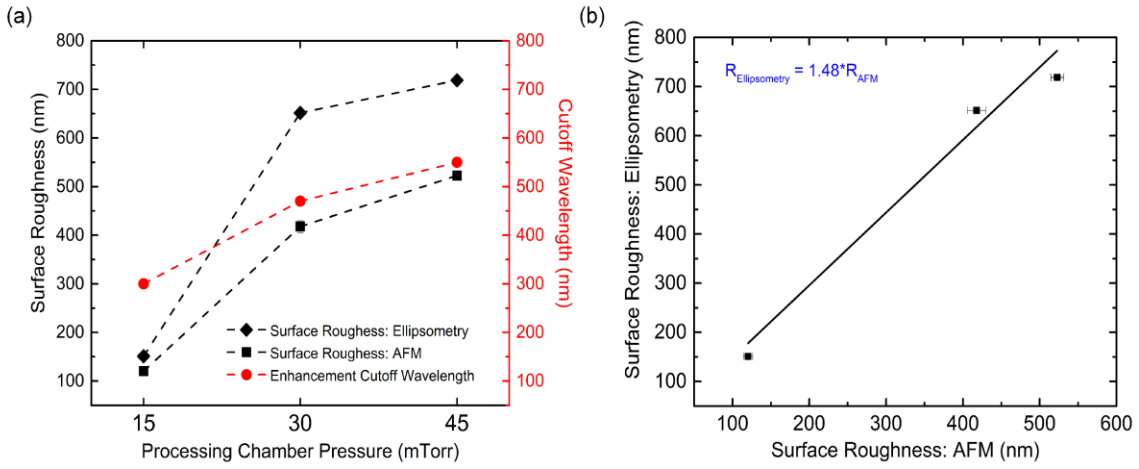

Figure 3.21. (Left) Measured maximum roughness (R_z) of the structured surface, plotted with the threshold transmission enhancement wavelength (λ_o) from Fig. 3.18, and (right) the comparison of surface roughness measured by AFM and its value analyzed using spectroscopic ellipsometric (SE) analysis, from the fused silica substrates processed at the chamber pressures shown in x-axis of the figure in left. The increase in process pressure results in increase in the values of R_z, cutoff transmission enhancement wavelength and, the average diameter of the featured surfaces.

Next, we measured and calculated the ellipsometric parameters (ψ and Δ) by using variable angle spectroscopic ellipsometry and investigated the phase shift produced at different wavelengths by the rARSS developed with various processing parameters [46].

A short description of spectroscopy ellipsometric (SE) analysis method is given in chapter 4.

The measurements were performed on both processed and unprocessed fused silica samples using a Woollam variable angle spectroscopic ellipsometer (WVASE) at three wavelengths: 633 nm, 1054 nm and 1550 nm, for all three processed rARSS samples, at variable angle of incidence from 20 degrees to 90 degrees, in increments of 0.1 degrees.

The results are shown in the figure 3.22. Both ellipsometric parameter measurements indicate a pseudo-Brewster angle, similar to that shown by an optical surface that is coated with absorbing material on top. However, in our case, the surface transmittance is higher than the planar (unprocessed) surface values, and there is no material dependent spectral absorption observed at these wavelengths.

For the sample processed at 45 mTorr chamber pressure, both of the ellipsometric measurements have large uncertainties, which result in large fluctuations in the polarization signal ratio. This observation is related to the proximity of the 633 nm test wavelength to the transmission enhancement asymptote (550 nm) and discussed further below.

The broadband spectral transmittance of optical wavelengths from 1000 nm to 1500 nm, at normal incidence for rARSS processed at chamber pressures of 30 mTorr and 45 mTorr are similar, as seen in figure 3.20 but the ellipsometric parameters ψ and Δ are quite different for the two samples in the above spectral band, as shown in figure 3.22. The two samples processed at chamber pressures of 30 mTorr and 45 mTorr have low normal incidence transmission enhancement at 633 nm, as can be seen in the figure 3.20. This

affects their light scattering at the above-mentioned wavelength, and thus reduces their Fresnel specular reflection.

The sample processed at higher chamber pressure (45 mTorr) has higher scatter and the ellipsometric measurements have more fluctuations. Also, the ellipsometric measurements from all processed samples have fewer fluctuations at angles of incidence greater than Brewster's angle.

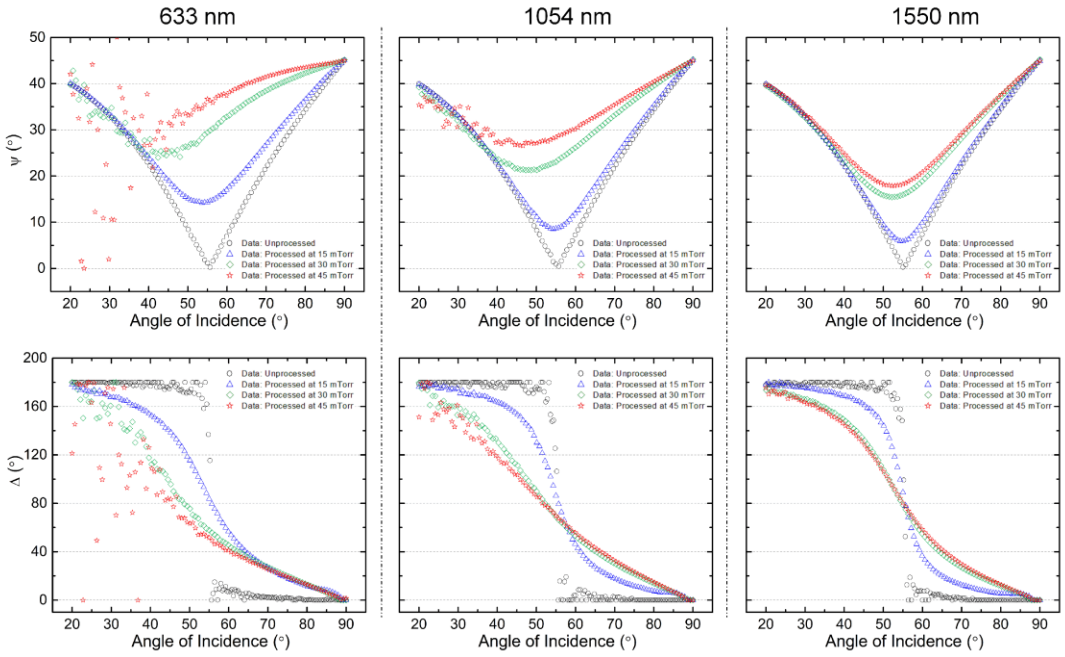

Figure 3.22. Measured ellipsometric parameters ψ (top) and Δ (bottom) with respect to the angle of incidence at 633 nm, 1054 nm, and 1550 nm wavelengths, for the three process pressures compared to an unprocessed fused silica surface. The sampled angular increment is 0.1°. Both ellipsometric parameters change more from the value of an unprocessed sample with increase in the process pressure. At low AOI, the polarized reflected specular beam values measured are very low, as it is evident for the low processing chamber pressure sample variations. Note the decrease of the pseudo-Brewster angle value with increasing process pressure at all three probe beam wavelengths.

The point at which the slope of the plot for ψ versus AOI intersects the horizontal line at ψ =0 is the Brewster/ pseudo-Brewster angle. The Brewster angle for the

unprocessed and the pseudo-Brewster angles for each processed sample was calculated at each incident wavelength for all processing chamber pressures. The method used for the calculation is shown in a representative figure 3.23, plotted for 1500 nm incident wavelength.

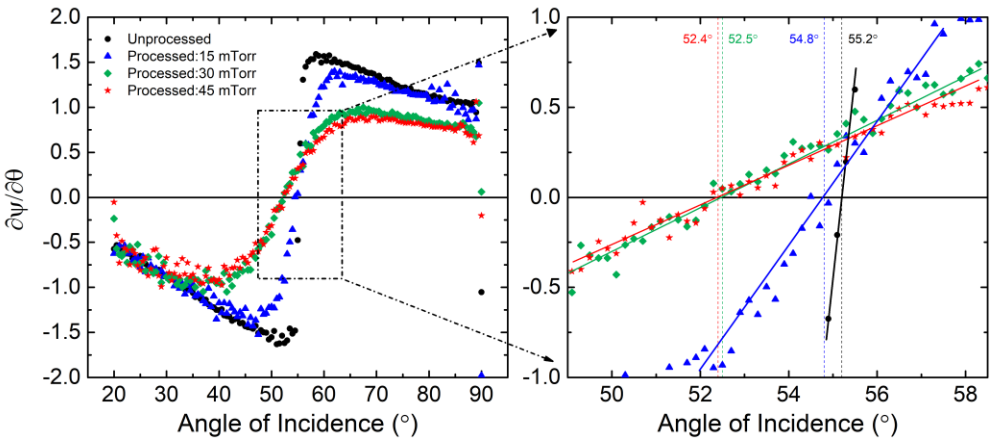

Figure 3.23. The Brewster's angle calculation from the plot of ψ versus angle of incidence at incident wavelength of 1550 nm. (Left) The plots of versus angle of incidence for samples processed with different parameters. (Right) Zoomed in portion of the figure on t the figure on the left and the slopes intersecting the horizontal line at ψ = 0, showing the Brewster angle for the unprocessed and pseudo-Brewster angles for the processed samples by dotted lines at the intersections.

The Brewster angle for the unprocessed and the pseudo-Brewster angles for each processed sample were calculated at the incident wavelengths as a function of processing chamber pressures, and the results are tabulated in table 3.11 and they are plotted in figure 3.24.

As in the case of lossy media, we determine the pseudo-Brewster angle as the angle of incidence for which the reflectivity polarization ratio is a minimum.

Table 3.11. Brewster's angle at incident wavelength for unprocessed and processed samples

Sample	Brewster Angle (°) at Incident Wavelength		
	1550 nm	1054 nm	633 nm
Unprocessed	55.2	55.4	55.5
Processed (15 mTorr)	54.8	54.6	54.5
Processed (30 mTorr)	52.5	50.2	46.3
Processed (45 mTorr)	52.4	48.5	44.2

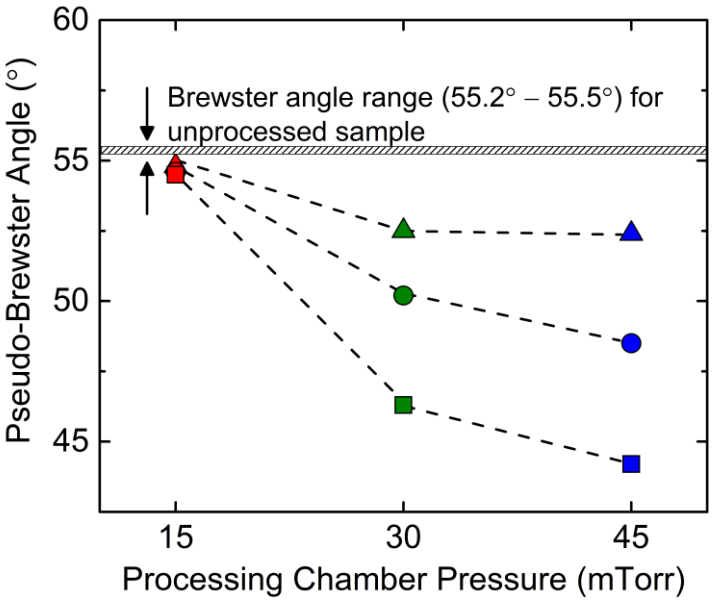

Figure 3.24. Measured pseudo-Brewster angle at wavelengths of 633 nm (□), 1054 nm (○) and 1550 nm (Δ), for samples processed at the chamber pressures indicated. The Brewster angle value for unprocessed fused silica is shown as the horizontal asymptote. The pseudo-Brewster angle increases as a result of the processing chamber pressure increase.

For higher processing pressures, the pseudo-Brewster angle values decrease for each of the wavelengths 633 nm, 1054 nm, and 1550 nm. We note that the values of the pseudo-Brewster angles approach the Brewster angle asymptote for the unprocessed fused silica substrate as the processing chamber pressure decreases.

The change in the slope of the cosine of the differential reflection phase shift at the pseudo-Brewster angles for the samples processed at different chamber pressures normalized to the same slope of the plane fused silica sample were calculated and are shown in figure 3.25. It is evident from the figure that the slope increases nonlinearly with an increase in processing chamber pressure for all the probe beam wavelengths 633 nm, 1054 nm, and 1550 nm.

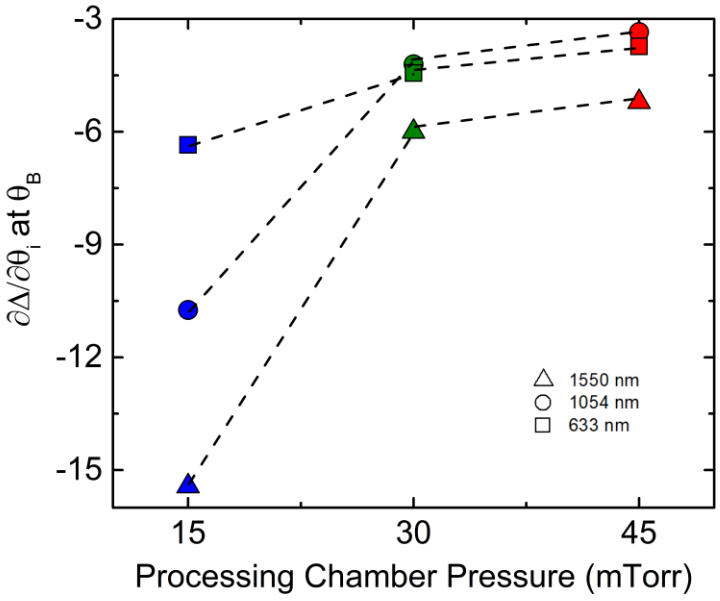

Figure 3.25. The rate of change of the differential reflection phase shift ($\partial\Delta / \partial\theta$) at pseudo-Brewster angles for fused silica samples processed at various chamber pressures. The rate of change increases non-linearly with higher processing chamber pressures for each of the test wavelengths: 633 nm (□), 1054 nm (○) and 1550 nm (Δ).

Finally, the rate of change of the differential reflection phase shift, with respect to the angle of incidence at the pseudo-Brewster angle, was plotted as a function of the ratio of maximum roughness depth to the incident wavelength (R_z/λ), as shown in figure 3.26.

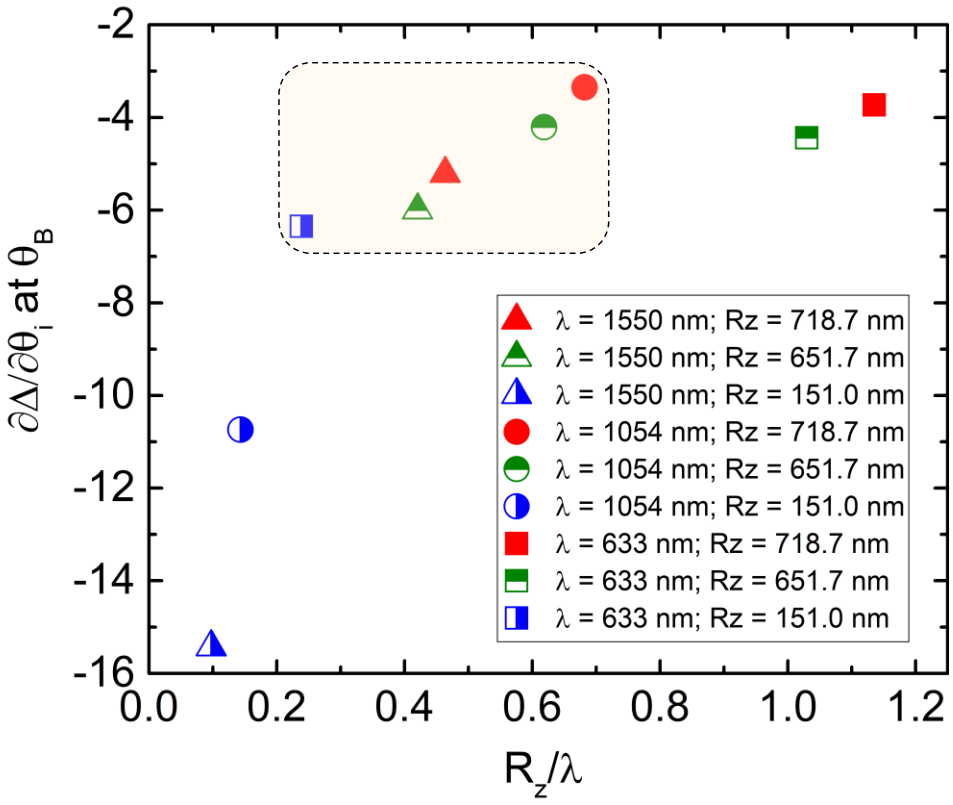

Figure 3.26. The rate of change of the differential reflection phase shift ($\partial\Delta / \partial\theta$) at pseudo-Brewster angle for samples processed with various chamber pressures for different ratios of average maximum roughness-to- incident beam wavelength (R_z/λ). This rate change increases with the increase in the values of R_z/λ for 633 nm (□), 1054 nm (○) and 1550 nm (Δ) wavelengths.

From this analysis, it can be observed that the rate of change of the differential phase shift increases with the decrease in the ratio of R_z/λ. The fabrication window (shown by the box on figure 3.26) correlates the processing parameters with R_z/λ at which maximum

transmittance enhancement occurs for an incident wave at normal angle of incidence. In other words, we can estimate the phase shift produced by a processing parameter at which the transmittance is maximum for a given spectral band.

In summary, three different random anti-reflective surface structures were fabricated on fused silica, using ICP-DRIE method. The random surface roughness was induced using different processing chamber pressures. The surface morphology characteristics, such as roughness and feature size distribution, were measured and compared to the optical transmittance of the samples. The normal incidence transmittance enhancement peak red shifts and the maximum transmittance bandwidth widens as the processing chamber pressure increases. The ellipsometric characterization on the sub-wavelength structured surfaces showed that the spectral transmittance for normal incidence through the two samples processed at different chamber pressures can be similar, but Δ can be significantly different for the spectral band. We found a smooth transition of Δ with respect to the angle of incidence (θ_i) for the air-substrate interfaces for fused silica rARSS. Since there is no significant absorption loss for fused silica substrates at the test wavelengths ($\leq$ 1550 nm), the increase in the depth of the etched surface and generating the gradient-indexed sub-wavelength profile of the fabricated surface could be accounted for the smooth transition of the ψ and Δ curves, with respect to the angle of incidence.

We determined that the rate of change of the differential reflection phase shift at pseudo-Brewster angle increases with the increase in wavelength of incident light, and it also increases with the increase in the ratio of maximum roughness depth to the incident wavelength (R_z/λ). The etched layer thicknesses and refractive indices of the processed samples were calculated using the ellipsometric data fitting method.

Furthermore, we were able to estimate the processing parameters for the fabrication of rARSS on fused silica surface at which a minimal Fresnel reflection occurs for a given wavelength of light incident normally on it.

CHAPTER 4 ANALYSIS AND SIMULATION OF OPTICAL PHENOMENA OF THE FABRICATED SUBSTRATES

In this chapter, the transmissivity through fabricated random anti-reflective surface structures (rARSS) on the plane fused silica samples have been simulated. The fabricated surface is random in the sense that the surface structures are not periodic in any direction and they do not have a fixed fill factor.

First, a short derivation of reflection and transmission of plane waves using Maxwell's equations is given to make a basis for calculation of transmissivity through multilayer dielectrics, which is given in next section [1, 47]. We used LEXT confocal microscope to measure the amount of substrate left at a measured depth from the ambient after ICP DRIE through the thickness of the material. Then the calculation of material/void percentage of the material using SE analysis at given thickness and the comparison of these parameters with that calculated experimentally using LEXT confocal microscope is shown. An introduction to spectroscopic ellipsometry is given and the necessity to use five-layer method to simulate the transmissivity through the fabricated samples is also shown. Then we used modified Bruggeman effective medium approximation to calculate the effective refractive index of each layer of certain thickness at a given depth of the fabricated random structures. The values of thickness and fill factor (and then refractive index) were verified by spectroscopy ellipsometry (SE) analysis of the fabricated rARSS. Then using matrix method of calculating transmittance and reflectance through multilayers of dielectrics, we simulated the transmittance through the fabricated rARSS on plane fused silica samples

making use of the modified Bruggeman effective medium approximation and adding scattering factor.

The simulated transmittance through the fabricated samples were compared with the experimentally measured transmittance through the samples using CARY spectrometer. The simulated and measured transmittance values were found to be in good agreement in a broadband non-scattering region.

4.1 Reflection and Transmission of Plane Waves using Maxwell's Equations

All the classical electromagnetic phenomena can be precisely described by using the following four equations, known as Maxwell's equations.

$$\nabla \times \boldsymbol{E} = -\frac{\partial \boldsymbol{B}}{\partial t} \tag{4.1}$$

$$\nabla \times \boldsymbol{H} = J + \frac{\partial \boldsymbol{D}}{\partial t} \tag{4.2}$$

$$\nabla \cdot \boldsymbol{D} = \rho \tag{4.3}$$

$$\nabla \cdot \boldsymbol{B} = 0 \tag{4.4}$$

The quantities used in the equations above are as follows:

E = Electric field intensity

H = magnetic field intensity

B = magnetic flux density

D = electric flux density

ρ = volume charge density

J = electric current density

The constitutive equations, to solve Maxwell's equations are the relationship between **B** and **H**, and that between **D** and **E**, are given by

$$\boldsymbol{D} = \varepsilon \boldsymbol{E} = \varepsilon_0 \boldsymbol{E} + \boldsymbol{P} \tag{4.5}$$

$$\boldsymbol{B} = \mu \boldsymbol{H} = \mu_0 \boldsymbol{H} + \boldsymbol{M} \tag{4.6}$$

The quantities ε and μ are permittivity and permeability tensors respectively, **P** and **M** are the electric and magnetic polarizations respectively. When an electromagnetic field is present in a matter, the electric field induces a dipole polarization **P** and magnetic field induces a magnetization **M** in the material. The quantities ε_0 and μ_0 are permittivity and permeability of vacuum respectively.

Applying curl operator in equation 4.1 and 4.2 and then using equation 4.3 and 4.4 in them, we get the electromagnetic equations as follows:

$$\nabla^2 \boldsymbol{E} - \mu\varepsilon \frac{\partial^2 \boldsymbol{E}}{\partial t^2} = 0 \tag{4.7}$$

$$\nabla^2 \boldsymbol{H} - \mu\varepsilon \frac{\partial^2 \boldsymbol{H}}{\partial t^2} = 0 \tag{4.8}$$

The equations (4.7) and (4.8) are satisfied by monochromatic plane waves.

For the calculation of reflection and transmission through a layered media, it is assumed that there is a continuity of some components of field vectors at the dielectric interfaces between the layers. Let us consider a plane wave incident on the interface is

partially reflected into the first medium and is partially transmitted through the interface into the second medium.

Let the field amplitude of the incident, reflected and transmitted plane waves be $\boldsymbol{E}_i\, e^{j(\omega t-\boldsymbol{k}_i .\boldsymbol{r})}$, $\boldsymbol{E}_r\, e^{j(\omega t-\boldsymbol{k}_r .\boldsymbol{r})}$ and $\boldsymbol{E}_t\, e^{j(\omega t-\boldsymbol{k}_t .\boldsymbol{r})}$ respectively, where ω is plane wave frequency and $\boldsymbol{k}_i$, $\boldsymbol{k}_r$ and $\boldsymbol{k}_t$ are the wave propagation vectors for incident, reflected and transmitted plane waves respectively.

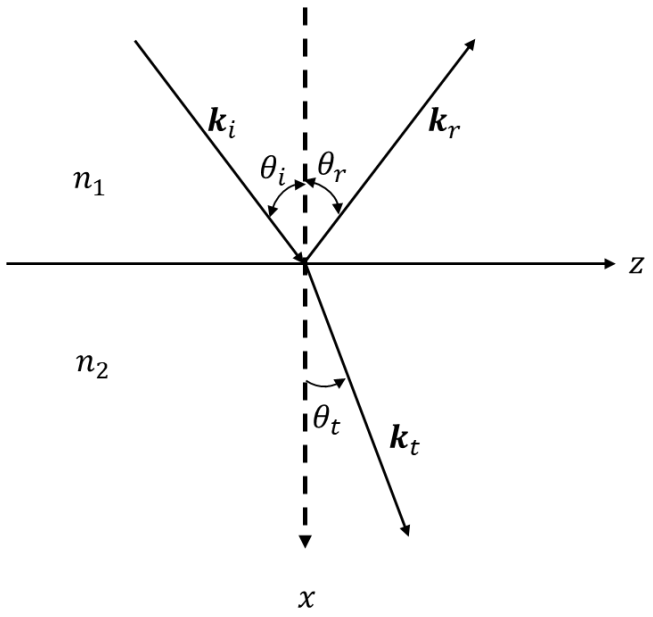

Figure 4.1. Reflection and refraction of a plane wave incident on the boundary between two homogeneous, isotropic, lossless dielectric media

Using the boundary conditions at the interface, the arguments of the field amplitudes must satisfy the equation

$$(\boldsymbol{k}_i \,.\, \boldsymbol{r})_{x=0} = (\boldsymbol{k}_r \,.\, \boldsymbol{r})_{x=0} = (\boldsymbol{k}_t \,.\, \boldsymbol{r})_{x=0} \qquad (4.9)$$

Assuming the refractive indices of medium 1 and 2 to be n_1 and n_2, the magnitudes of the wave numbers would be

$|\boldsymbol{k}_i| = |\boldsymbol{k}_r| = (\omega/c)\, n_1$ and $|\boldsymbol{k}_t| = (\omega/c)\, n_2$ (4.10)

The equations (4.9) and (4.10) imply that all three propagation wave vectors ($\boldsymbol{k}_i, \boldsymbol{k}_r$ and $\boldsymbol{k}_t$) lie in the same plane, which is called plane of incidence; and their tangential components must also be equal to each other.

If the angle of incidence, reflection and transmission of the wave vectors with respect to the normal of the plane interface, be θ_i, θ_r and θ_t respectively,

$$n_1 \sin\theta_i = n_1 \sin\theta_r = n_2 \sin\theta_t \quad (4.11)$$

This gives

$$\theta_i = \theta_r \quad (4.12)$$

$$\frac{n_2}{n_1} = \frac{\sin\theta_i}{\sin\theta_t} \quad (4.13)$$

which is famously known as Snell's law.

The superposition of the incident and reflected waves in each medium gives the general solution of the wave equations (4.7) and (4.8), and these can be written as

$$\boldsymbol{E} = \begin{cases} \boldsymbol{E}_1 \exp(-i\,\boldsymbol{k}_1.\boldsymbol{r} + i\,\omega t) + \boldsymbol{E'}_1 \exp(-i\,\boldsymbol{k'}_1.\boldsymbol{r} + i\,\omega t), & x < 0 \\ \boldsymbol{E}_2 \exp(-i\,\boldsymbol{k}_2.\boldsymbol{r} + i\,\omega t) + \boldsymbol{E'}_2 \exp(-i\,\boldsymbol{k'}_2.\boldsymbol{r} + i\,\omega t), & x < 0 \end{cases} \quad (4.14)$$

where $\mathbf{E}_1$, $\mathbf{E}_1'$, $\mathbf{E}_2$, and $\mathbf{E}_2'$ are constant complex vectors; and $\mathbf{k}_1'$, and $\mathbf{k}_2'$ are the mirror images of the wave vectors $\mathbf{k}_1$, and $\mathbf{k}_2$, with respect to the *yz* plane. In this case, $\mathbf{E}_1$ is the amplitude of incidence, $\mathbf{E}_1'$ is the amplitude of reflection, $\mathbf{E}_2$ is amplitude of transmission, and $\mathbf{E}_2'$ is the amplitude of reflection in the second medium which is zero.

The calculation for magnetic field vector from equations 4.7 and 4.14 gives

$$\boldsymbol{H} = \frac{i}{\mu\varepsilon}\,\boldsymbol{\nabla} \times \boldsymbol{E} \qquad (4.15)$$

In case of s-wave (TE wave), the electric field vectors are perpendicular to the plane of incidence and magnetic field vectors are in the plane of incidence. The magnetic field vectors give a positive energy flow in the direction of the wave propagation, as shown in the figure 4.2.

Let us consider a plane wave with wave vector $\mathbf{k}_1$ and frequency ω incidents on the interface of the medium 1 and 2, as shown in figure 4.2. It partially reflects back in the same medium 1, and partially transmits in the second medium 2. The wave vectors of reflected and transmitted plane waves are $\mathbf{k}_1'$ and $\mathbf{k}_2$. The permittivity and permeability of the medium 1 and medium 2 are ε_1, μ_1 and ε_2, μ_2 respectively.

Suppose the incident wave vector $\mathbf{k}_1$ makes an angle θ_1 and the transmitted wave vector $\mathbf{k}_2$ makes an angle θ_2 with respect to the normal to the interface.

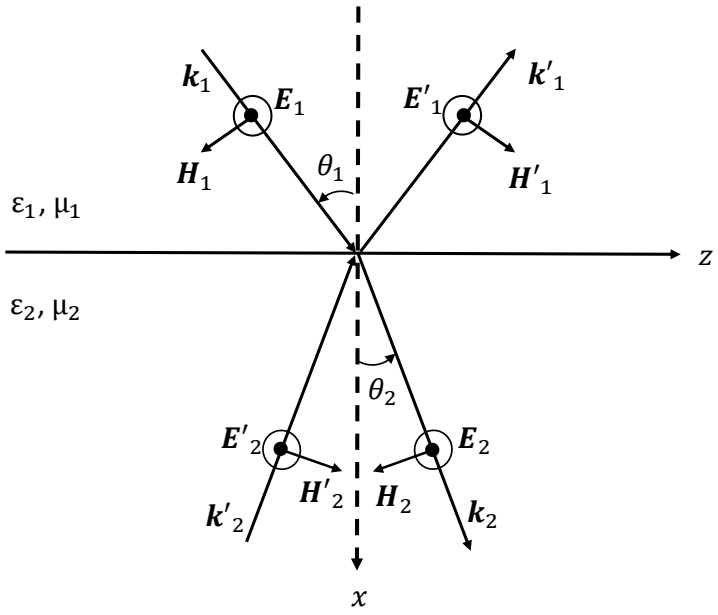

Figure 4.2. Incidence, reflection and transmission of s-wave (TE wave)

Applying the boundary conditions, the tangential components of electric and magnetic fields at the interface $x = 0$ should be continuous. If these wave vectors are resolved into independent parallel wave (with subscript p) and perpendicular (with subscript s) components, it can be shown that these are independent of each other for homogeneous and isotropic media 1 and 2.

The continuity of E_y and H_z at the interface x = 0 gives

$$E_{1s} + E'_{1s} = E_{2s} + E'_{2s} \tag{4.16}$$

$$\sqrt{\frac{\varepsilon_1}{\mu_1}}(E_{1s} - E'_{1s})\cos\theta_1 = \sqrt{\frac{\varepsilon_2}{\mu_2}}(E_{2s} - E'_{2s})\cos\theta_2 \tag{4.17}$$

The equations (4.16) and (4.17) can be written in a matrix form as follows:

$$D_s(1)\begin{pmatrix} E_{1s} \\ E'_{1s} \end{pmatrix} = D_s(2)\begin{pmatrix} E_{2s} \\ E'_{2s} \end{pmatrix} \tag{4.18}$$

where the dynamic matrix of the s wave for the medium i (i = 1, 2) is given by

$$D_s(i) = \begin{pmatrix} 1 & 1 \\ \sqrt{\frac{\varepsilon_i}{\mu_i}} & \sqrt{\frac{\varepsilon_i}{\mu_i}} \end{pmatrix} \tag{4.19}$$

For the s-wave incident from the medium 1, the reflection and transmission coefficients for a single interface are given by

$$r_s = \left(\frac{E'_{1s}}{E_{1s}}\right)_{E'_{2s}=0} \tag{4.20}$$

$$t_s = \left(\frac{E_{2s}}{E_{1s}}\right)_{E'_{2s}=0} \tag{4.21}$$

There is only one boundary and the *s*-wave incidents on the boundary coming from medium 1 and only the transmitted wave E_{2s} exists in the medium 2. The incident *s*-wave on the interface from medium 2 does not exist and is taken to be zero. Hence, we can write $E'_{2s} = 0$.

Assuming $\mu_1 = \mu_2$, we get

$$r_s = \frac{n_1 \cos\theta_1 - n_2 \cos\theta_2}{n_1 \cos\theta_1 + n_2 \cos\theta_2} \tag{4.22}$$

$$t_s = \frac{2n_1 \cos\theta_1}{n_1 \cos\theta_1 + n_2 \cos\theta_2} \tag{4.23}$$

In case of p-wave (TM wave), the magnetic field vectors are perpendicular to the plane of incidence and electric field vectors are in the plane of incidence. The magnetic field vectors give positive energy flow in the direction of the wave propagation, as shown in the figure 4.3.

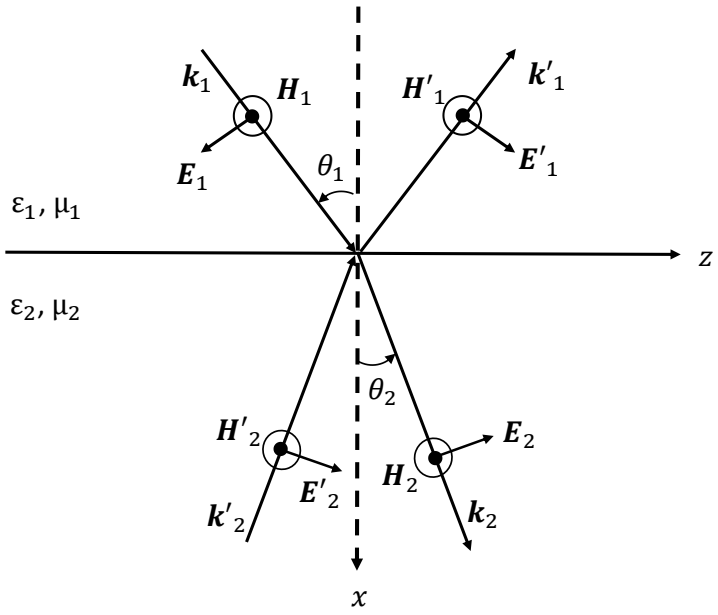

Figure 4.3. Incidence, reflection and transmission of p-wave (TM wave)

The continuity of E_z and H_y at the interface x = 0 gives

$$(E_{1p} + E'_{1p})\cos\theta_1 = (E_{2p} + E'_{2p})\cos\theta_2 \tag{4.24}$$

$$\sqrt{\frac{\varepsilon_1}{\mu_1}}(E_{1p} - E'_{1p}) = \sqrt{\frac{\varepsilon_2}{\mu_2}}(E_{2p} - E'_{2p}) \tag{4.25}$$

The equations (4.24) and (4.25) can be written in a matrix form as follows:

$$D_p(1)\begin{pmatrix} E_{1p} \\ E'_{1p} \end{pmatrix} = D_s(2)\begin{pmatrix} E_{2p} \\ E'_{2p} \end{pmatrix} \tag{4.26}$$

where the dynamic matrix of the *p* wave for the medium *i* (*i* = 1, 2) is given by

$$D_p(i) = \begin{pmatrix} \cos\theta_i & \cos\theta_i \\ \sqrt{\frac{\varepsilon_i}{\mu_i}} & -\sqrt{\frac{\varepsilon_i}{\mu_i}} \end{pmatrix} \tag{4.27}$$

For the p-wave, the reflection and transmission coefficients for a single interface are given by

$$r_p = \left(\frac{E'_{1p}}{E_{1p}}\right)_{E'_{2p}=0} \tag{4.28}$$

$$t_p = \left(\frac{E_{2p}}{E_{1p}}\right)_{E'_{2p}=0} \tag{4.29}$$

There is only one boundary and the *p*-wave incidents on the boundary coming from medium 1 and only the transmitted wave E_{2p} exists in the medium 2. The incident *p*-wave on the interface from medium 2 does not exist and is taken to be zero. Hence, we can write $E'_{2p} = 0$.

Again, assuming $\mu_1 = \mu_2$, we get

$$r_s = \frac{n_1 \cos\theta_2 - n_2 \cos\theta_1}{n_1 \cos\theta_2 + n_2 \cos\theta_1} \tag{4.30}$$

$$t_s = \frac{2n_1 \cos\theta_1}{n_1 \cos\theta_2 + n_2 \cos\theta_1} \tag{4.31}$$

The time averaged pointing vector for a plane wave of amplitude E, in a dielectric (so that the refractive index is real), with a real wave vector (k) is given by

$$\boldsymbol{S} = \frac{\boldsymbol{k}}{2\,\mu\omega} |\boldsymbol{E}|^2 \tag{4.32}$$

The reflectance and transmittance of the s- and p- plane waves are given by

$$R_s = |\boldsymbol{r_s}|^2 \tag{4.33}$$

$$R_p = \left|\boldsymbol{r_p}\right|^2 \tag{4.34}$$

$$T_s = \frac{n_2 \cos\theta_2}{n_1 \cos\theta_1} |t_s|^2 \tag{4.35}$$

$$T_p = \frac{n_2 \cos\theta_2}{n_1 \cos\theta_1} \left|t_p\right|^2 \tag{4.36}$$

The reflectance values at varying angle of incidences for a plane wave incident at an interface of air ($n_1 = 1.0$) and glass ($n_2 = 1.5$) is given in the figure 4.4:

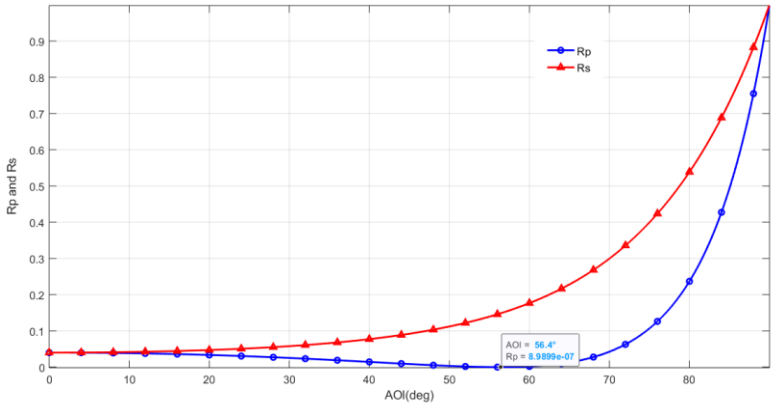

Figure 4.4. Reflectance values (R_s and R_p) for a single interface dielectric.

4.2 Reflectance and Transmittance through Multilayered Dielectric Media

Let us consider an electromagnetic wave is incident on a multiple isotropic layered dielectric media from ambient of refractive index n_0. A number of multiple homogeneous dielectric films of various thicknesses and various refractive indices are coated on the top of the substrate layer by layer. The refractive indices of N layers 1, 2, 3, …., N are n_1, n_2, n_3, ……, n_N and the thicknesses are d_1, d_2, d_3, d_4, ……, d_N respectively. The refractive index of the substrate is n_s, as shown in figure 4.5.

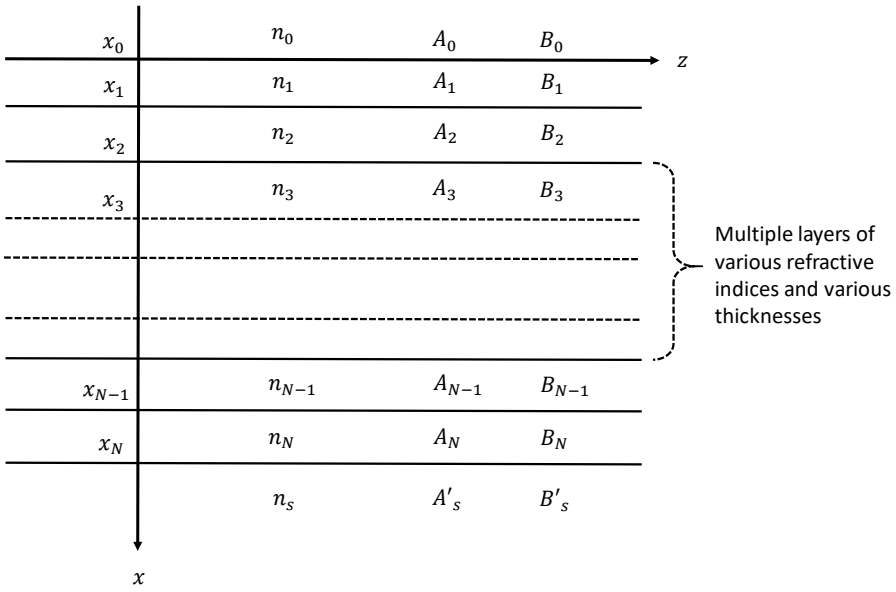

Figure 4.5. Reflection and transmission of electromagnetic waves through multilayer dielectric medium

The thicknesses of the films are related as follows:

$$\left.\begin{aligned} d_1 &= x_1 - x_0 \\ d_2 &= x_2 - x_1 \\ d_3 &= x_3 - x_2 \\ \ldots\ldots &= \cdots\ldots\ldots\ldots \\ d_N &= x_N - x_{N-1} \end{aligned}\right\} \tag{4.37}$$

The refractive indices are related as

$$n(x) = \begin{cases} n_0, & x < x_0 \\ n_1, & x_0 < x < x_1 \\ n_2, & x_1 < x < x_2 \\ & \ldots\ldots\ldots\ldots \\ n_N, & x_{N-1} < x < x_N \\ n_s, & x_N < x \end{cases} \tag{4.38}$$

The dielectric medium in z-direction is homogeneous, such that $\frac{\partial n}{\partial z} = 0$. The propagation of the electromagnetic wave is in *x*-*z* plane. The electric field of a general plane-wave solution of the wave equation for either an *s*-wave (**E** || **y**) or a *p*-wave (**H** || **y**) can be written in the form:

$$E = E(x)e^{i(\omega t - \beta z)} \tag{4.39}$$

where, β is the *z* component of the wave vector and ω is its angular frequency.

Once the electromagnetic wave incidents on the interface, the electric field E(x) has the components travelling up and down. These can be written as

$$E(x) = \begin{cases} A_0 e^{-ik_{0x}(x-x_0)} + B_0 e^{ik_{0x}(x-x_0)}, & x < x_0 \\ A_l e^{-ik_{lx}(x-x_l)} + B_l e^{ik_{lx}(x-x_l)}, & x_{l-1} < x < x_l \\ A'_s e^{-ik_{sx}(x-x_N)} + B'_s e^{ik_{sx}(x-x_N)}, & x_N < x \end{cases} \tag{4.40}$$

where $\pm k_{lx}$ are the *x* components of the wave vectors, which can be written as

$$k_{lx} = \left[\left(n_l \frac{\omega}{c}\right)^2 - \beta^2\right]^{\frac{1}{2}}, \qquad l = 0, 1, 2, 3, \ldots . N, s \tag{4.41}$$

If the ray angle is θ_l, then

$$k_{lx} = n_l \frac{\omega}{c} cos\theta_l \tag{4.42}$$

The coefficients A_l and B_l are the amplitudes of the plane waves at interface $x = x_l$.

The electric field *E(x)* is continuous when represented as in equation (4.34), but it is no longer continuous when it is decomposed into two parts (travelling up = $A_l e^{-ik_{lx}(x-x_l)}$ and travelling down = $B_l e^{ik_{lx}(x-x_l)}$, the decomposed parts are no longer continuous at the interfaces. The two amplitudes of *E(x)* can be represented in column vectors using dynamical matrices as follows:

$$\begin{pmatrix} A_0 \\ B_0 \end{pmatrix} = {D_0}^{-1} D_0 \begin{pmatrix} A_1 \\ B_1 \end{pmatrix},$$

$$\begin{pmatrix} A_l \\ B_l \end{pmatrix} = P_l {D_l}^{-1} D_{l+1} \begin{pmatrix} A_{l+1} \\ B_{l+1} \end{pmatrix}, \quad l = 1, 2, 3, \ldots\ldots, N \qquad (4.43)$$

In the relation (4.42), N+1 represents the *s* layer, $A_{N+1} = A'_s$ and $B_{N+1} = B'_s$.

The dynamical matrices can be respectively written as

$$D_l = \begin{pmatrix} 1 & 1 \\ n_l cos\theta_i & -n_l cos\theta_i \end{pmatrix} \qquad \text{for } s \text{ wave} \qquad (4.44)$$

and

$$D_l = \begin{pmatrix} cos\theta_i & cos\theta_i \\ n_l & -n_l \end{pmatrix} \qquad \text{for } p \text{ wave} \qquad (4.45)$$

The value of P_l can be written as

$$P_l = \begin{pmatrix} e^{i\phi_l} & 0 \\ 0 & e^{-i\phi_l} \end{pmatrix}, \qquad \text{with} \quad \phi_l = k_{lx}\, d_l \qquad (4.46)$$

With the help of these matrices, we can write the relation between A_0, B_0 and A'_s, B'_s as

$$\begin{pmatrix} A_0 \\ B_0 \end{pmatrix} = \begin{pmatrix} M_{11} & M_{12} \\ M_{21} & M_{22} \end{pmatrix} \begin{pmatrix} A'_s \\ B'_s \end{pmatrix}, \qquad (4.47)$$

where the matrix is given by

$$\begin{pmatrix} M_{11} & M_{12} \\ M_{21} & M_{22} \end{pmatrix} = {D_0}^{-1} \left[\prod_{l=1}^{N} D_l P_l \, {D_l}^{-1} \right] D_s \qquad (4.48)$$

The reflection coefficient is given by

$$r = \left(\frac{B_0}{A_0}\right)_{B_s=0} = \frac{M_{21}}{M_{11}} \tag{4.49}$$

The transmission coefficient is given by

$$t = \left(\frac{A_s}{A_0}\right)_{B_s=0} = \frac{1}{M_{11}} \tag{4.50}$$

where we defined $A_s = A'_s,\ B_s = B'_s$ and dropped the prime (′).

Now the reflectance is given by

$$R = |r|^2 = \left|\frac{M_{21}}{M_{11}}\right|^2, \tag{4.51}$$

where it is assumed that the medium 0 is lossless.

When all the layers and the bounding media are pure dielectrics with real n_0 and n_s , and the incident and transmitted wave have real propagation vectors (with real θ_0 and real θ_s), the transmittance is given by

$$T = \frac{n_2\, cos\theta_s}{n_0 cos\theta_0}\ |t|^2 = \frac{n_2\, cos\theta_s}{n_0 cos\theta_0}\ \left|\frac{1}{M_{11}}\right|^2, \tag{4.52}$$

4.3 Ellipsometric Measurements and Data Analysis

We used ellipsometer to measure the ellipsometric parameters ψ and Δ of the three samples which had optimized transmissivities in three different spectral regions. The sample A had the maximum transmissivity in the visible region, the sample B had maximum transmissivity in the near-infrared region, while the sample C had the maximum transmissivity in the short-wave infrared region. These three fabricated samples were taken as the representative samples for the simulations.

4.3.1 Fundamentals of Spectroscopic Ellipsometry

Spectroscopic ellipsometry (SE) is a non-invasive, non-destructive optical metrology where a change in polarization state of a beam of light that reflects from or transmits through a sample is measured. with the goal being to extract information about the optical properties and layer thickness of the sample. In particular, for a set angle of incidence, the spectral dependence of the complex ratio of the amplitude reflection coefficients for the two orthogonal linear polarization states (*p* and *s*), defined by $r_p/r_s \equiv \tan\Psi \exp(i\Delta)$, provides information on the multilayer film structure and on the complex dielectric functions of the layer components. This non-invasive technique can be used for both in-situ and ex-situ characterization of samples that could be as simple in optical structure as an uncoated bulk substrate or a single layer on a bulk substrate, or as complicated as multiple layers in opto-electronic devices [46, 48].

Ellipsometry in reflection mode provides a description of the ratio of the reflected to incident wave polarization states, whereby each polarization state itself is defined as a ratio of *p* to *s* complex field components. Equivalently, the measurement provides a description of the ratio of complex amplitude reflection coefficients for the *p* and *s* waves. This latter description is given in terms of the ellipsometric angles (ψ and Δ) as follows

$$\rho = \frac{r_p}{r_s} = \frac{|r_p|}{|r_s|}\exp\left[i\,(\delta_{rp} - \delta_{rs})\right] = tan\psi \exp(i\Delta), \tag{4.53}$$

where

$$\psi = \tan^{-1}\left(\frac{|r_p|}{|r_s|}\right), \tag{4.54}$$

$$\Delta = \delta_{rp} - \delta_{rs} \tag{4.55}$$

Hence, the ellipsometric angle ψ is a measure of the ratio (p-to-s) of the relative field amplitude changes upon reflection (each described as a reflected-to-incident ratio), and the angle Δ is the difference ($p-s$) in the phase shifts upon reflection (each described as a reflected−incident difference). Thus, both angles describe the complex incident and reflected electric field vector components vibrating parallel and perpendicular to the plane of incidence.

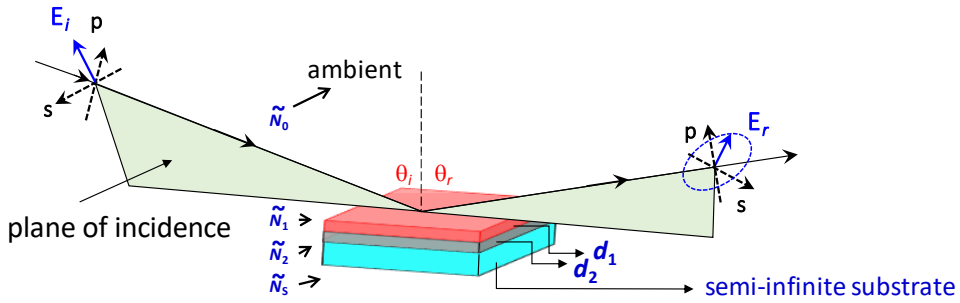

Figure 4.6. Schematic of ellipsometric measurement on a multi-layer coating on a semi-infinite substrate. Ellipsometric angles ψ and Δ measured from the sample is a function of complex index of refractions for the component layers including the substrate, layer thickness, and angle of incidence. Parameters of interest are derived from non-linear regression analysis by considering a realistic optimal model representing the sample under measurement.

4.3.2 Ellipsometric Measurement and Analysis

In this paragraph, the samples prepared as described in chapters 2 and 3 were used to measure the Ψ and Δ using the variable angle spectroscopic ellipsometer (VASE), manufactured by J. A. Woollam (WVASE). The sample was put at angle of incidence of zero degree to the incident beam. The measurements were taken at three different wavelengths: 550 nm, 1054 nm and 1550 nm for each sample. The backside of the sample was taped with a scotch tape so that the backside reflection was reduced to zero, making

sure that diffused reflection was not registered at the detector. The reflectivity was measured in such a way that the detector receives specular reflection only. Each of the measurement was taken from angle of incidence of 22 degrees to 90 degrees at an increment of 0.1 degrees.

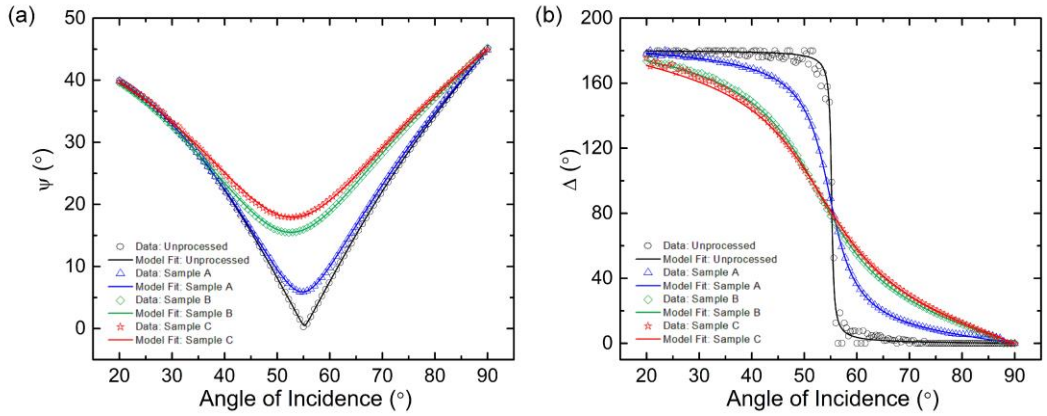

Figure 4.7. Experimental versus model fit ellipsometric angles acquired at $\lambda = 1550\ nm$ for four samples: (a) unprocessed, (b) processed sample A, (c) processed sample B, and (d) processed sample C are shown in the figure.

The figure 4.7 shows the experimental versus model fit of ψ and Δ acquired on four different samples at beam wavelength, λ = 1550 nm. First and foremost, bare substrate which has been identified as unprocessed sample in this chapter was analyzed by considering a semi-infinite bulk layer with surface roughness layer on top by considering effective medium approximation (EMA). The EMA layer is considered to consist 50/50 volume fractions of bulk material and void. The dielectric function for the glass substrate (unprocessed sample) is represented by the combination of Sellmeier equations. The analytical expression commonly used to model the dispersion in the real part of a dielectric function for transparent material can be expressed as,

$$\varepsilon = \varepsilon_{1o} + \sum_{i=1}^{2} \frac{A_i E_i^2}{E_i^2 - E^2} \qquad (4.56)$$

where ε_{1o} is a constant additive term to the real part of dielectric functions, A_i and E_i are the amplitudes and resonance energies of the two oscillators respectively that define (along with ε_{1o}) the Sellmeier equation. The figure 4.9 shows the optical model used for the ellipsometric analysis and the parameters derived from the analysis. The point to remember here is that the unprocessed sample was analyzed by considering the data collected at three wavelengths which required using a dispersion relation in the real part of dielectric function. For the analysis of rest of the samples as shown in Fig. 4.8 (b), (c), and (d) ellipsometric data at 1550 nm were considered and dielectric function for the material is fixed to the value obtained in the analysis of unprocessed sample.

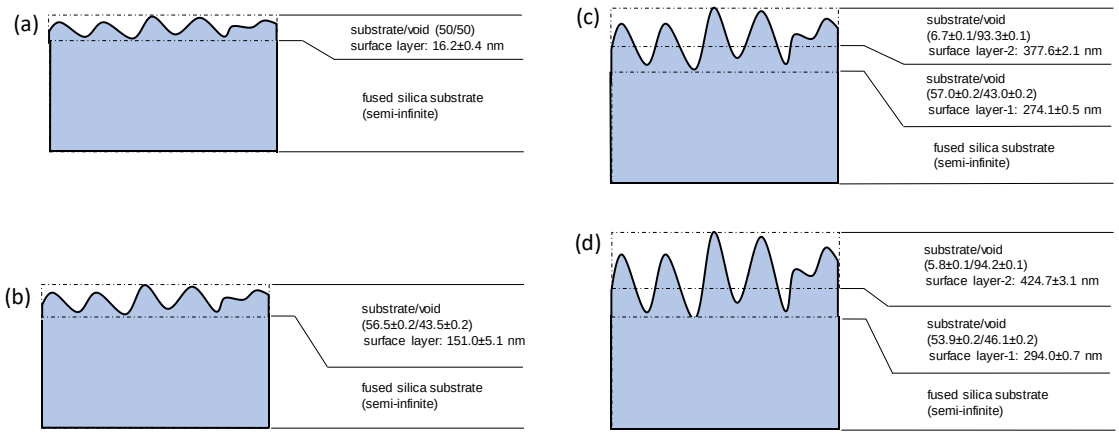

Figure 4.8. Optical model used for the analysis and structural parameters derived have been shown in the figures for four samples: (a) unprocessed sample, (b) processed sample A, (c) processed sample B, and (d) processed sample C are shown in the figure.

The roughness modulation in processed sample A is smaller as compared to that for the processed samples B and C. Hence, the unprocessed sample and the processed sample

A were modeled by considering a single roughness layer, as shown in figures 4.9 (a) and 4.9 (b) respectively. The processed samples B and C showed a higher degree of roughness modulation and thus they required multi-layer surface roughness model that best represented the samples under analysis, as shown in figures 4.9 (c) and 4.9 (d) respectively. The figure 4.9 also depicts structural parameters derived from the ellipsometric analysis.

4.4 Modified Bruggeman Theory

The Bruggeman theory derived from Clausius-Mossotti relation has been modified to calculate the refractive index of the medium at a given thickness.

4.4.1 One-dimensional Periodic Medium

Let us consider a one-dimensional periodic medium (such as, grating, that has the period of Λ) is made by mixing two different dielectric media. Suppose the refractive index of the medium 1 and medium 2 are respectively n_1 and n_2 of the substrate. The zeroth order effective medium approximation (EMA), in quasi-static limit ($\lambda >> \Lambda$), has the periodic scale independent form given by:

$$n_{eff}^{(0)} = \sqrt{n_1^2\left(1 - f_x f_y\right) + n_2^2 f_x f_y} \qquad (4.57)$$

where the fill factors of the dielectric media in x and y direction are f_x and f_y respectively.

For a non-periodic medium, composed of random distributions of "spherical particles" of m materials, the zeroth order EMA, in quasi-static limit ($\lambda >> \Lambda$), has the periodic scale independent form, given by

$$\sum_m f_m \frac{\varepsilon_m - \varepsilon}{\varepsilon_m + 2\varepsilon} = 0 \qquad (4.58)$$

This is Bruggeman EMA for spherical "inclusions" in a medium with resulting index $n^2 = \varepsilon$.

For two materials (i.e. air and fused silica of refractive index n), the resulting effective refractive index can be expressed as follows:

$$n_{eff} = \sqrt{\varepsilon} = \frac{1}{2}\sqrt{\sqrt{\Omega^2 + 8n^2} - \Omega} \tag{4.59}$$

where, $\Omega = (n^2 - 2)(1 - f) + (1 - 2n^2) f$ (4.60)

The simulated transmissivity obtained using five-layer method was closer to the value of the experimental transmissivity through the fabricated substrates.

In more general form, the equation (4.58) can be written as

$$\sum_m f_m \frac{\varepsilon_m - \varepsilon}{\varepsilon_m + \zeta\varepsilon} = 0 \tag{4.61}$$

where ζ is an adjustable "structure" parameter, that can be expressed as

$$\zeta = \frac{1}{\ell} - 1\,; \quad 0 < \ell \leq 1 \tag{4.62}$$

and ℓ is a geometric factor (ℓ = 1/3 for spheres and ℓ = 1/2 for disks).

Then the Bruggeman EMA for air and silica, we used ζ = 1 and/or 2 values to build a structure of variable fill factor (f), such that each layer (made of silica disks in air) has an effective refractive index:

$$n_{eff} = \sqrt{\frac{\sqrt{\Omega^2 + 4\zeta n^2} - \Omega_m}{2\zeta}} \tag{4.63}$$

where $\Omega_m = (n^2 - \zeta)(1 - f_m) + (1 - \zeta n^2) f_m$ (4.64)

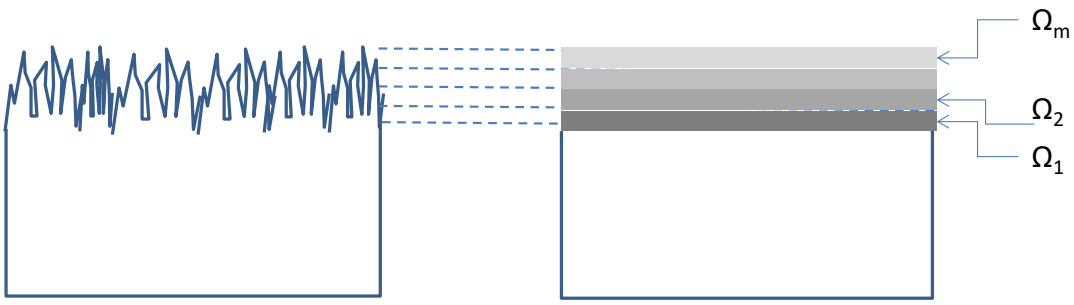

Figure 4.9. Random structured surface structure and its equivalent surface structure

The substrate structure with many layers of random structures and its equivalent thin film layered surface structure can be shown in figure (4.9).

4.5 Simulation of Transmissivity through Fabricated rARSS

The thin film matrix formula for calculating the transmissivity was used to simulate the transmissivity through the fabricated rARSS on planar fused silica. The simulated transmissivity using formula (4.51) was compared to the experimentally measured transmissivity from 300nm to 2200nm. Spectroscopic ellipsometry (SE) analysis was done to determine the thickness and the amount of substrate left at the given thickness. We used five layers of the fabricated rARSS on plane fused silica sample in SE analysis.

The tables 4.1, 4.2 and 4.3 show the comparison of the measured data using LEXT confocal microscope with the data obtained by SE analysis for three processed samples A, B and C respectively which were etched using different etching parameters.

Table 4.1. Measured Data of Sample A from SE analysis and by using LEXT confocal microscope

Data of Sample A from SE analysis	
Substrate Material left after Etching (%)	Distance of the layer from ambient (nm)
0	0
5.49	32.38
25.72	63.84
54.15	80.73
77.32	102.14
95.42	112.52
100	154.20

Measured Data of Sample A from LEXT confocal microscope	
Substrate Material left after Etching (%)	Distance of the layer from ambient (nm)
0	0
10	45.48
20	57.70
30	65.97
40	72.46
50	78.21
60	83.61
70	89.01
80	94.95
90	102.60
100	153.14

Table 4.2. Measured Data of Sample B from SE analysis and by using LEXT confocal microscope

Data of Sample B from SE analysis	
Substrate Material left after Etching (%)	Distance of the layer from ambient (nm)
0	0
4.69	148.79
34.52	335.45
52.94	390.28
77.32	462.68
95.42	574.32
100	768.36

Measured Data of Sample B from LEXT confocal microscope	
Substrate Material left after Etching (%)	Distance of the layer from ambient (nm)
0	0
10	217.98
20	281.45
30	321.78
40	353.07
50	380.76
60	407.50
70	435.71
80	469.11
90	518.03
100	780.24

Table 4.3. Measured Data of Sample B from SE analysis and by using LEXT confocal microscope

Data of Sample C from SE analysis	
Substrate Material left after Etching (%)	Distance of the layer from ambient (nm)
0	0
5.12	172.25
25.72	322.31
54.15	412.018
77.32	488.77
95.42	649.26
100	826.34

Measured Data of Sample C from LEXT confocal microscope	
Substrate Material left after Etching (%)	Distance of the layer from ambient (nm)
0	0
10	233.59
20	297.21
30	338.53
40	371.26
50	400.57
60	428.66
70	458.39
80	493.50
90	545.43
100	820.21

The values of thickness and void/material percentage obtained by SE analysis were compared with the values obtained experimentally measured values using LEXT confocal microscope, as shown in figures 4.10, 4.11 and 4.12. They correspond to the values given in the table 4.1, 4.2 and 4.3 respectively.

The material percentage of the fabricated sample A left at different five depths was obtained using SE analysis. This is shown in the figure 4.10 (a). The material percentage of the fabricated sample A at various depths obtained experimentally using LEXT UV confocal microscopy is shown in the figure 4.10 (b). The material percentage of the fabricated sample A left at different five depths obtained using SE analysis was compared with that obtained experimentally using LEXT UV confocal microscopy were compared with each other and they match perfectly with each other, using the conversion factor as described in the figure 3.21 (b) obtained using AFM and LEXT.

Similarly, the material percentage left at different five depths after etching the sample B was obtained using SE analysis. This is shown in the figure 4.11(a). The material percentage of the fabricated sample B at various depths obtained experimentally using LEXT UV confocal microscopy is shown in the figure 4.11 (b).

(a)

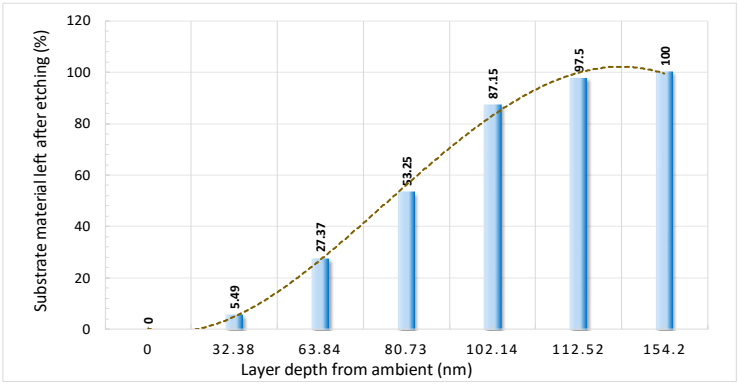

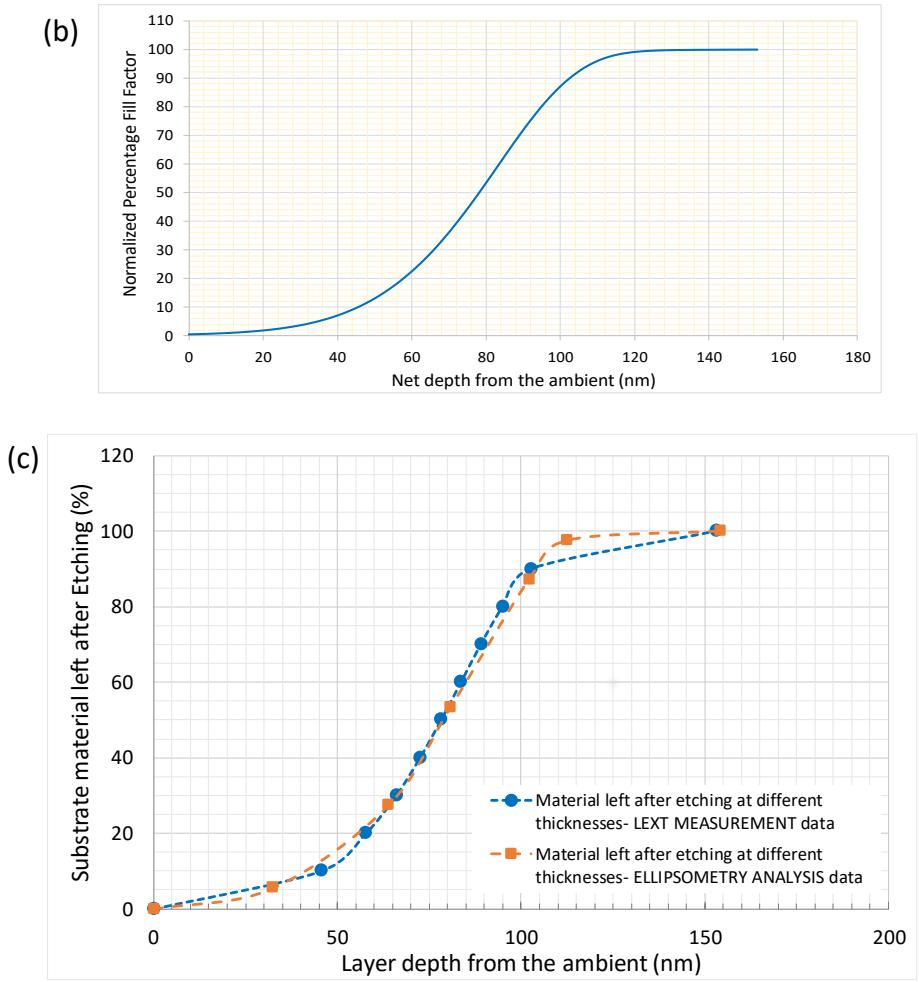

Figure 4.10. (a) Material percentage left at different five depths obtained from SE analysis of the fabricated sample A. (b) Material percentage at various depths obtained experimentally using LEXT UV confocal microscopy. (c) Comparison of the measured value with the values obtained by SE analysis.

The material percentage of the fabricated sample B left at different five depths obtained using SE analysis was compared with that obtained experimentally using LEXT UV confocal microscopy were compared with each other and they match perfectly with each other, using the conversion factor as described in the figure 3.21 (b) obtained using AFM and LEXT.

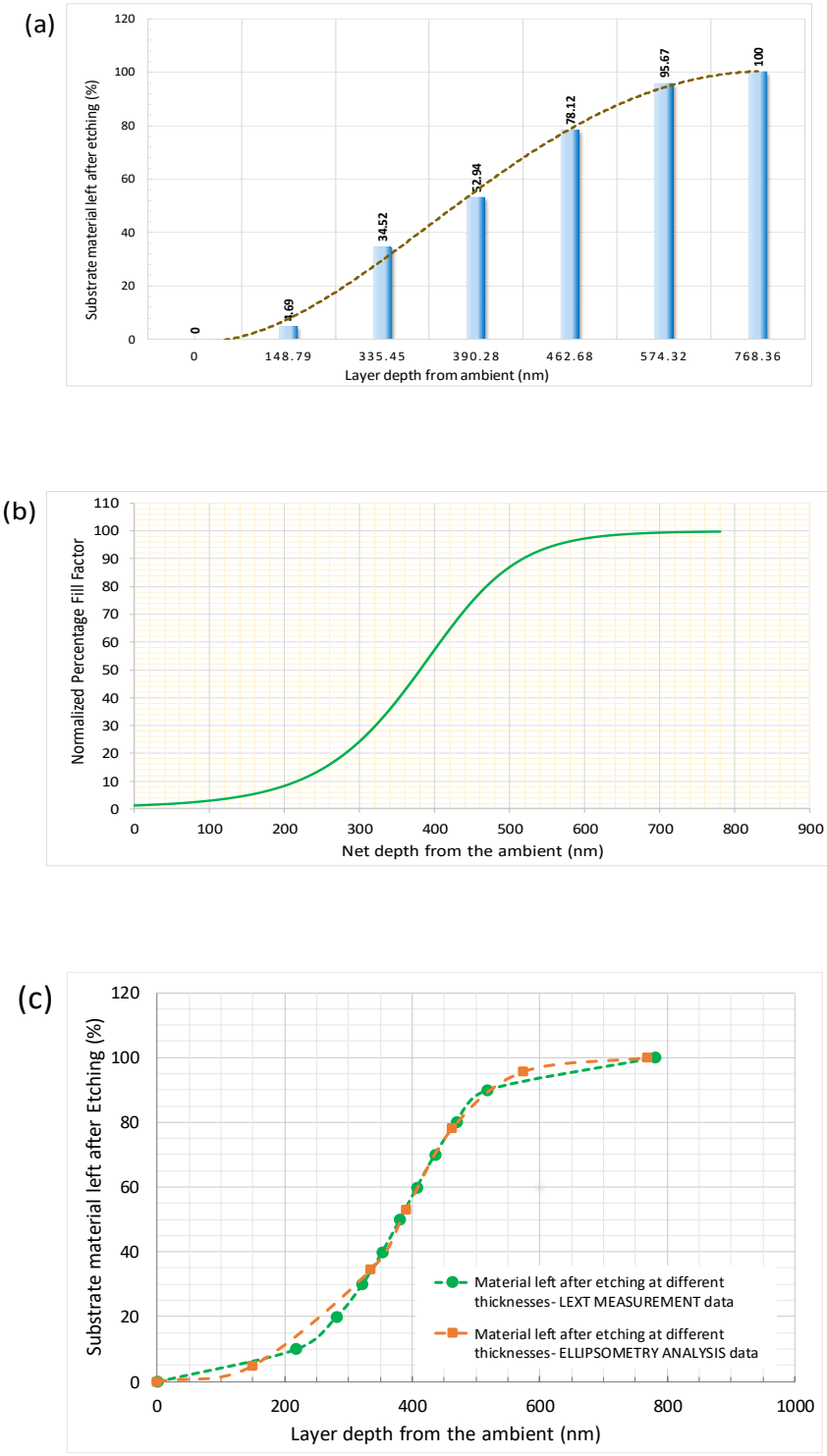

Figure 4.11. (a) Material percentage left at different five depths obtained from SE analysis of the fabricated sample B. (b) Material percentage at various depths obtained experimentally using LEXT UV confocal microscopy. (c) Comparison of the measured value with the values obtained by SE analysis.

The material percentage of the fabricated sample C left at different five depths was obtained using SE analysis. This is shown in the figure 4.12 (a). The material percentage of the fabricated sample C at various depths obtained experimentally using LEXT UV confocal microscopy is shown in the figure 4.12 (b). The material percentage of the fabricated sample C left at different five depths obtained using SE analysis was compared with that obtained experimentally using LEXT UV confocal microscopy were compared with each other and they match perfectly with each other, using the conversion factor as described in the figure 3.21 (b) obtained using AFM and LEXT.

(a)

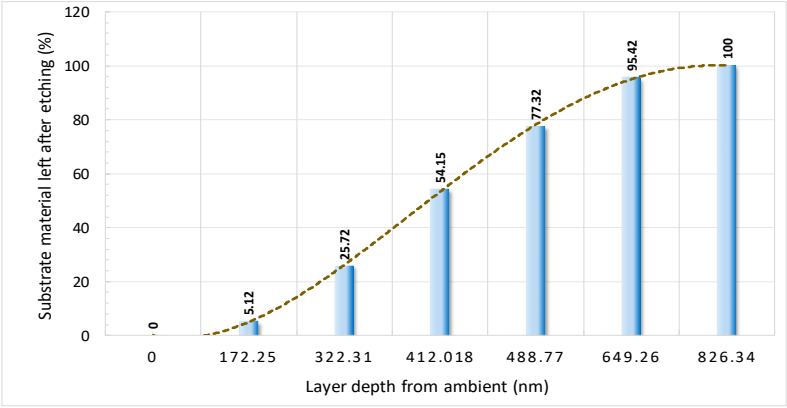

(b)

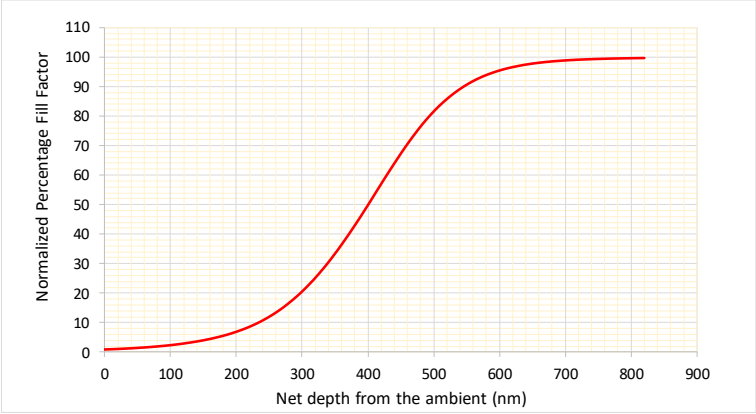

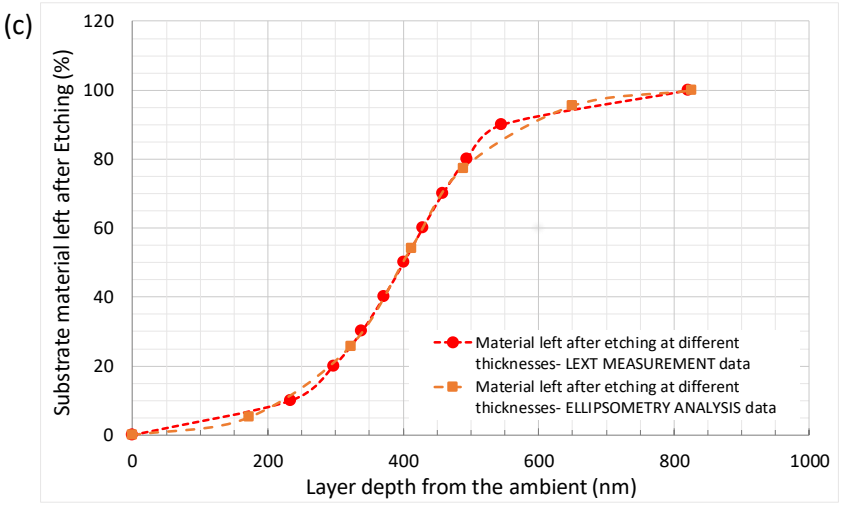

Figure 4.12. (a) Material percentage left at different five depths obtained from SE analysis of the fabricated sample C. (b) Material percentage at various depths obtained experimentally using LEXT UV confocal microscopy. (c) Comparison of the measured value with the values obtained by SE analysis.

They show a very good agreement with each other as shown in the figures 4.10, 4.11 and 4.12 for three different samples processed at three different chamber pressures, keeping other etching parameters fixed. These values were used in the modified Bruggeman theory to calculate the refractive indices of the thin layers to be used in the formula (4.51).

The five-layer model used in the SE analysis of the fabricated rARSS is shown in the figure 4.13.

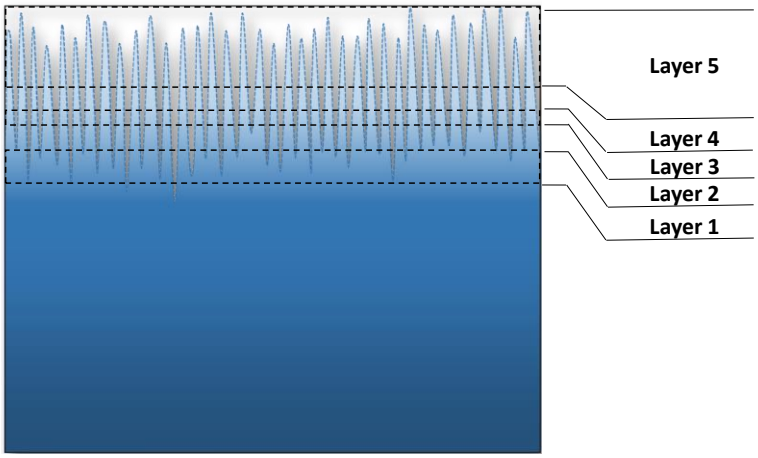

Figure 4.13. Five-layer model used in SE method for the analysis of thickness and fill factor of each layer

The corresponding layer thicknesses used in the simulation are shown in the figure 4.14, 4.15 and 4.16 for the three samples discussed in figures 4.8 (b), 4.8 (c) and 4.8 (d).

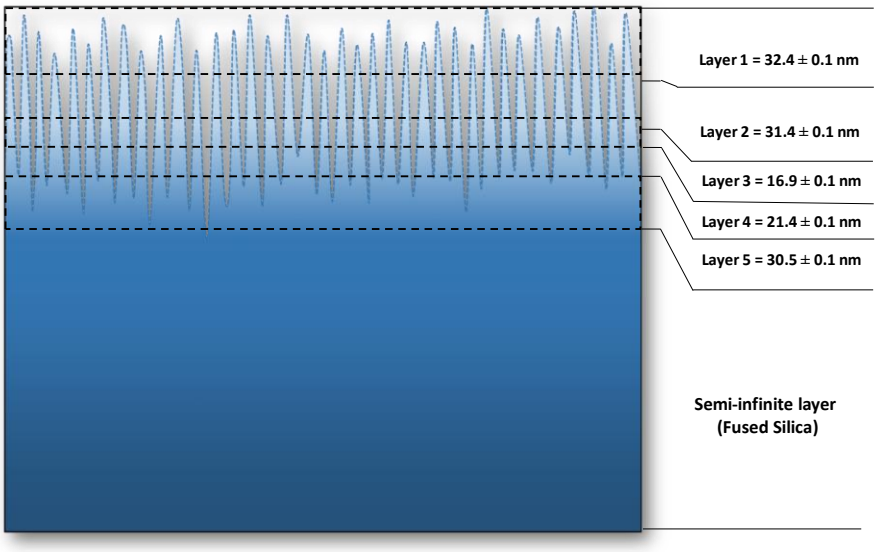

Figure 4.14. Five-layer model used in SE method for the analysis of thickness and fill factor of each layer of the fabricated sample A.

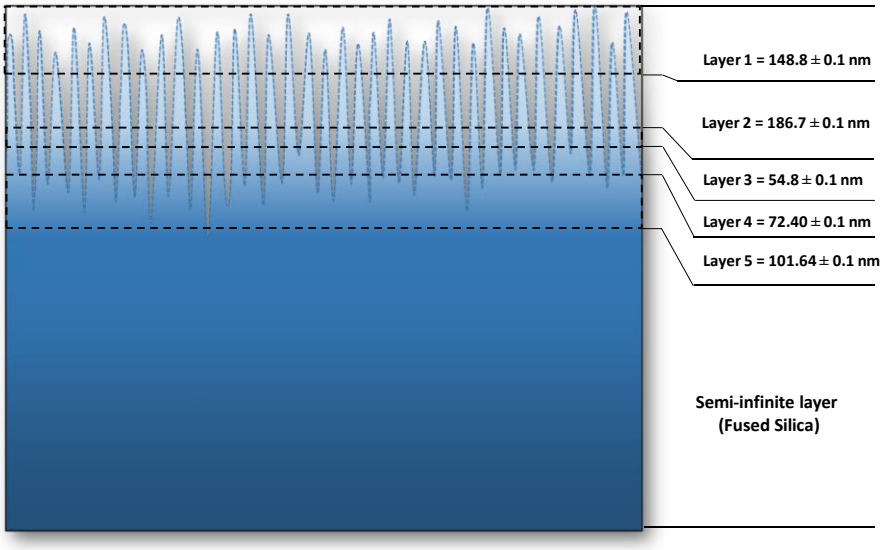

Figure 4.15. Five-layer model used in SE method for the analysis of thickness and fill factor of each layer of the fabricated sample B.

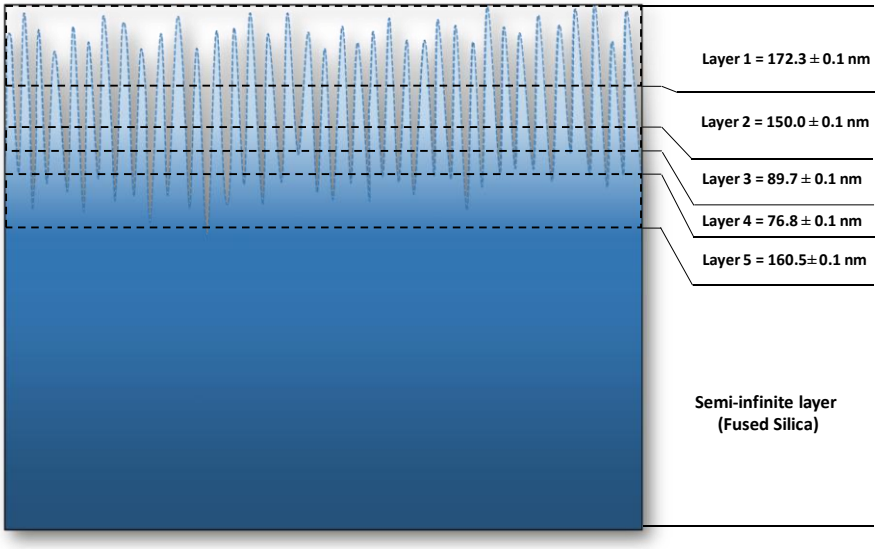

Figure 4.16. Five-layer model used in SE method for the analysis of thickness and fill factor of each layer of the fabricated sample C.

These parameters were used in the multi-layer anti-reflective surface dielectric medium simulation, and adding an appropriate scattering in the model, the transmittance through the samples described above were simulated. Since the transmittance of the sample

is between the transmittivities of the samples we are considering simulating. The comparison of simulated and measured transmittances for the three fabricated rARSS on fused plane silica samples B, is shown in the figures 4.18. The figure shows that the simulated data using 5- layers matched with the experimentally obtained data in large part of the wavelength region. But it is evident that the simulated data is drifted more in the scattering region. A more robust scattering term suitable for a random surface is needed to get more realistic matching of the data.

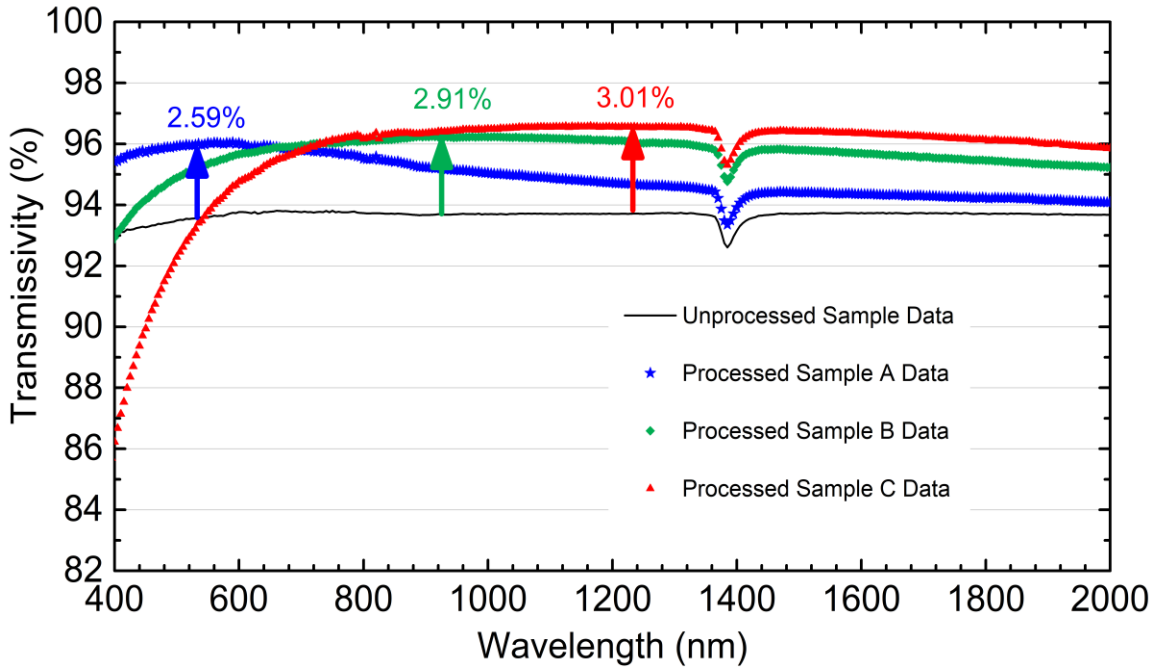

Figure 4.17. Measured optical transmittance of samples A, B and C, and the unprocessed fused silica sample

Also, the near infrared spectrum of the UV grade fused silica sample suffers the transmissivity because of the hydroxyl absorption. This dip in the transmittance has not been addressed in our simulations.

The transmissivity data of the three one-side processed fused silica samples A, B and C, and the unprocessed fused silica sample as measured by spectroscope is shown in the figure 4.17.

The transmissivity data was simulated for sample B using the 5-layer model as obtained by SE analysis and the comparison is shown in the figure 4.18.

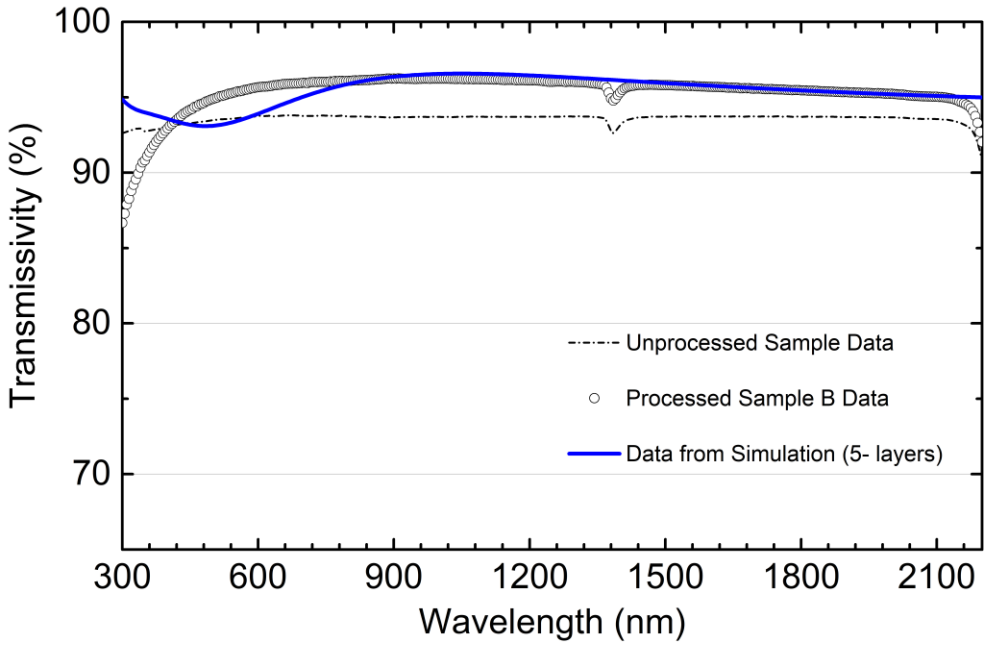

Figure 4.18. Comparison of simulated transmissivity data with the experimental data using 5- layers obtained from SE analysis

The simulated transmissivity data is in good agreement in the region higher than ~ 850 nm, but it does not match below ~ 850 nm. In order to match the simulated data more closely with the experimental data, more data points (i.e. the layer thicknesses) were used. The new data points were obtained from the LEXT confocal microscopy as shown in the figure 4.11. Since the data obtained from SE analysis and the data obtained using LEXT

confocal microscope match perfectly with each other, more thickness layers obtained experimentally using LEXT microscope were used. In figure 4.20, the comparison of simulated transmissivity data with the experimental data using 10- layers.

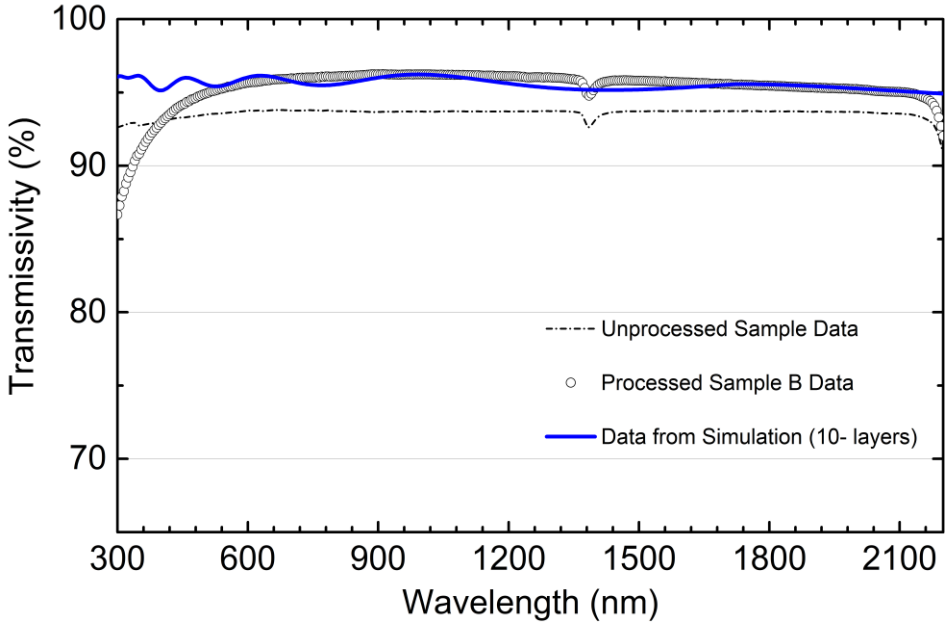

Figure4.19. Comparison of simulated transmissivity data with the experimental data using 10-layers obtained from SE analysis

The simulated transmissivity data using 10 layers matched in larger wavelength region than that using only 5 layers. In this case, the simulated data matched the experimental data in the region higher than ~ 550 nm but did not match in the region where the scattering phenomenon was observed, which was in the region lower than ~ 550 nm.

The transmitted data was multiplied with a scattering factor which is the function of the average feature size of the nanostructures, wavelength and total roughness of the structured surface.

The new relation for the transmissivity through the substrate was

$$T_d = T_l\,[1 - \exp(-x)] \qquad (4.65)$$

where, T_d is the transmissivity obtained using scattering factor, T_l is the transmissivity obtained using multi-layered model, and x is the scattering factor, which is given by

$x = f(\lambda, R_z, D)$ where D is the average feature size of the structure.

Using the relation (4.65) in the data obtained in simulated value of figure 4.19 gives the simulated values which are plotted in figure 4.21. It was simulated data of the processed sample B, which matched very well with the experimental transmissivity data.

Similarly, the transmissivity data were simulated for samples A and C which are plotted against the experimental data of the transmissivity in figures 4.20 and 4.22 respectively.

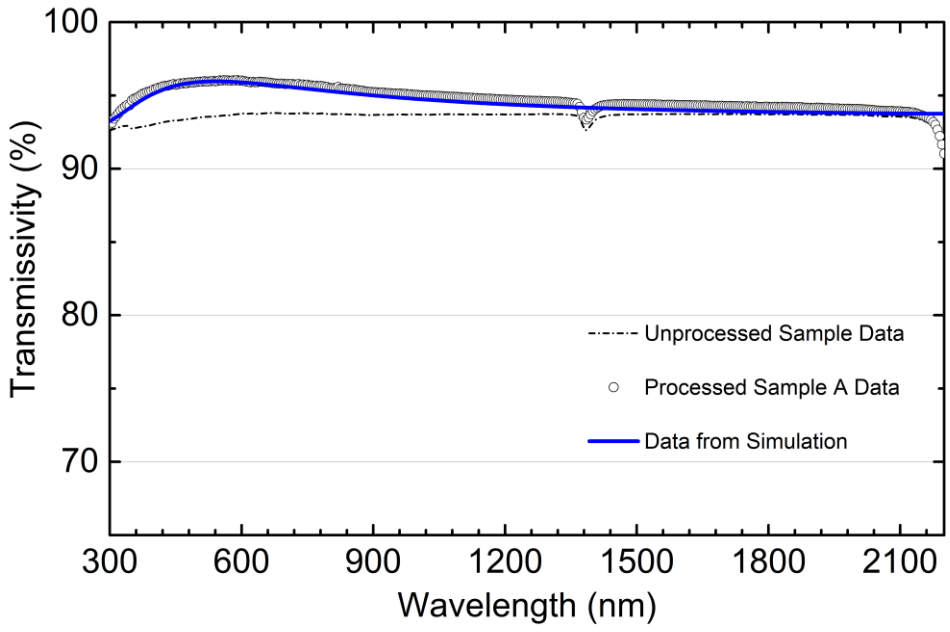

Figure 4.20. Comparison of simulated transmittance with measured optical transmittance of sample A using 10-layered dielectric substrate with scattering added.

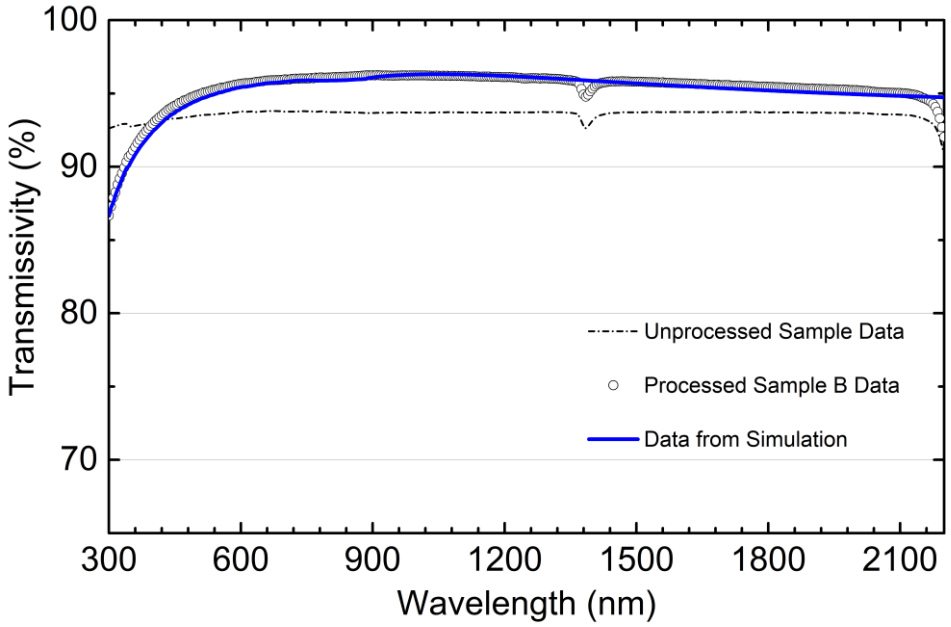

Figure 4.21. Comparison of simulated transmittance with measured optical transmittance of sample B using 10-layered dielectric substrate with scattering added.

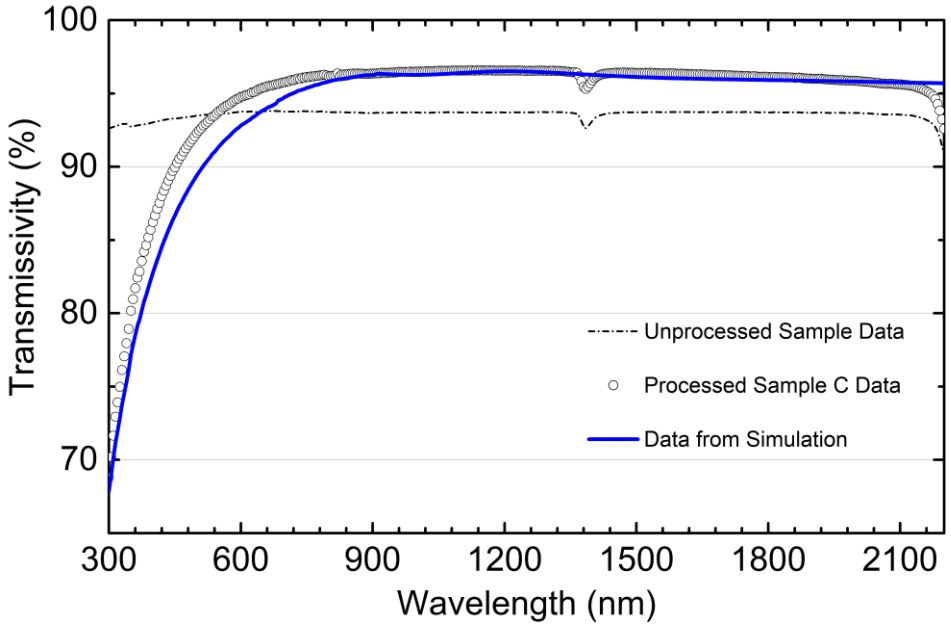

Figure 4.22. Comparison of simulated transmittance with measured optical transmittivity of sample C using 10-layered dielectric substrate with scattering added.

In summary, the derivation of reflection and transmission of plane waves using Maxwell's equations is given to make a basis for calculation of transmissivity through multilayer dielectrics, which is given in next section. We used LEXT confocal microscope to measure the amount of substrate left at a measured depth from the ambient after ICP DRIE through the thickness of the material. Then the calculation of material/void percentage of the material using SE analysis at given thickness and the comparison of these parameters with that calculated experimentally using LEXT confocal microscope is shown. An introduction to spectroscopic ellipsometry is given and the necessity to use five-layer method to simulate the transmissivity through the fabricated samples is also shown. Then we used modified Bruggeman effective medium approximation to calculate the effective refractive index of each layer of certain thickness at a given depth of the fabricated random structures. The values of thickness and fill factor (and then refractive index) were verified by spectroscopy ellipsometry (SE) analysis of the fabricated rARSS. Then using matrix method of calculating transmittance and reflectance through multilayers of dielectrics, we simulated the transmittance through the fabricated rARSS on plane fused silica samples making use of the modified Bruggeman effective medium approximation.

The simulated transmittance through the fabricated samples were compared with the experimentally measured transmittance through the samples using CARY spectrometer.

The simulated and measured transmittance values were found to be in good agreement in a broadband non-scattering region.

CHAPTER 5 CONCLUSION AND FURTHER WORK

Optical surfaces can be fabricated to act as an anti-reflective (AR) by coating single- or multi-layered dielectrics on it. However, the optical response through these surfaces is polarization- dependent and angle-dependent. Also, they degrade quickly on exposure to environment and laser radiation. The alternatives to these coated AR surfaces are periodic sub-wavelength AR structures fabricated on optical surfaces. There is no material mismatch with the substrate in this case, contrary to that in the case of dielectric-coated AR surfaces. The polarization-dependency and angle-dependency of optical response of these structured surfaces is still an issue for some applications.

The optical surfaces fabricated with random AR surface structures (rARSS) have been proved to be largely angle-independent and polarization-independent. They also withstand higher power laser damage threshold. There is a limited amount of research done in the area of fabrication and modeling of the rARSS.

We extended the research area in the fabrication of rARSS and added a physical model which will be able to simulate the optical response of the fabricated rARSS and relate it to the fabrication parameters. The fused silica substrates were etched using ICP DRIE method. The etching parameters were investigated and optimized to get very high transmittance (nearly perfect) from Visible to Short-wave Infrared (SWIR) region.

The fabricated samples were characterized using UV confocal microscopy, Scanning Electron Microscopy, Atomic Force Microscopy, Ellipsometry and Spectroscopy. The parameters obtained from these measurements were analyzed using Spectroscopic

Ellipsometry (SE). Then a physical model was developed using to simulate the transmissivity of the rARSS.

It can be seen from the analysis that the total roughness of the processed samples increases with the increase in the etching parameters varied in the experiments: chamber pressure, coil power, platen power, and etching time. The three representative wavelength regions, at which the transmissivity of the etched samples was maximum, were in visible, near-infrared, and in the short-wave infrared regions. These three samples were considered to characterize, analyze and build a physical model to simulate the transmissivities of the samples.

The processing parameters for the fabrication of rARSS on fused silica surface were estimated at which a minimal Fresnel reflection occurs for a given wavelength of light incident normally on it.

The etching parameters and the values obtained from the optical and physical characterization of the processed samples were determined. Then, modified Bruggeman effective medium approximation was used in the formula for the transmissivity of the multi-layered dielectric media with appropriate scattering. The physical model simulated the transmissivity of the representative samples, which matched very well with the experimental transmissivity of the samples obtained.

This research can be extended to estimate and find the etching parameters of the random anti-reflective surface structures needed in the higher wavelength regions, such as in 8-12 μm IR region or for millimeter region.

The application of in situ ellipsometry during ICP DRIE process could be used to get more robust processing parameters for broadband antireflection (BBAR) by restructuring an optical substrate with random surface on the it.

Also, the research can be extended to find the superhydrophobic random anti-reflective surface structures on the plane as well on the curved surfaces.

REFERENCES

1. Born, M., *Principles of optics : electromagnetic theory of propagation, interference and diffraction of light.* 1999.

2. Moreno, I., J.J. Araiza, and M. Avendano-Alejo, *Thin-film spatial filters.* Optics letters, 2005. **30**(8): p. 914-916.

3. Heavens, O.S., *Thin film physics.* 1970.

4. Dobrowolski, J., et al., *Toward perfect antireflection coatings. 3. Experimental results obtained with the use of Reststrahlen materials.* Applied optics, 2006. **45**(7): p. 1555-1562.

5. Lin, C.-W., et al., *Design and fabrication of an alternating dielectric multi-layer device for surface plasmon resonance sensor.* Sensors and Actuators B: Chemical, 2006. **113**(1): p. 169-176.

6. David, C., et al., *Nano-structured anti-reflective surfaces replicated by hot embossing.* Microelectronic Engineering, 2002. **61-62**(C): p. 435-440.

7. Lutey, A.H.A., et al., *Nanosecond and sub-nanosecond pulsed laser ablation of thin single and multi-layer packaging films.* Applied Surface Science, 2013. **285**(PB): p. 300-308.

8. Rayleigh, L., *On Reflection of Vibrations at the Confines of two Media between which the Transition is Gradual.* Proceedings of the London Mathematical Society, 1879. **s1-11**(1): p. 51-56.

9. Spinelli, P., M.A. Verschuuren, and A. Polman, *Broadband omnidirectional antireflection coating based on subwavelength surface Mie resonators.* Nature Communications, 2012. **3**.

10. Hobbs, D.S., B.D. MacLeod, and J.R. Riccobono. *Update on the development of high performance anti-reflecting surface relief micro-structures*. in *Conference on Window and Dome Technologies and Materials X*. 2007. Orlando, FL.

11. Schulze, M., et al. *New approach for antireflective fused silica surfaces by statistical nanostructures - art. no. 68830N*. in *Conference on Advanced Fabrication Technologies for Micro/Nano Optics and Photonics*. 2008. San Jose, CA.

12. Schaepkens, M. and G.S. Oehrlein, *A Review of SiO[sub 2] Etching Studies in Inductively Coupled Fluorocarbon Plasmas.* Journal of The Electrochemical Society, 2001. **148**(3): p. C211.

13. Busse, L.E., et al., *Review of antireflective surface structures on laser optics and windows.* Applied Optics, 2015. **54**(31): p. F303-F310.

14. Pacholski, C., et al., *Antireflective subwavelength structures on microlens arrays-comparison of various manufacturing techniques.* Applied Optics, 2012. **51**(1): p. 8-14.

15. Plummer, J.D., *Silicon VLSI technology : fundamentals, practice, and modeling.* 2000.

16. *Handbook of plasma processing technology : fundamentals, etching, deposition, and surface interactions.* 1990.

17. Lin, H.-H., et al., *Fabrication of antireflective nanostructures for crystalline silicon solar cells by reactive ion etching.* Thin Solid Films, 2013. **529**: p. 138-142.

18. Ray, T., H. Zhu, and D.R. Meldrum, *Deep reactive ion etching of fused silica using a single-coated soft mask layer for bio-analytical applications.* Journal of Micromechanics and Microengineering, 2010. **20**(9): p. 097002.

19. Domanski, M., et al., *Submicron-patterning of bulk titanium by nanoimprint lithography and reactive ion etching.* Nanotechnology, 2012. **23**(6): p. 065306.

20. Tian, W.C., J.W. Weigold, and S.W. Pang, *Comparison of Cl[sub 2] and F-based dry etching for high aspect ratio Si microstructures etched with an inductively coupled plasma source.* Journal of Vacuum Science & Technology B: Microelectronics and Nanometer Structures, 2000. **18**(4): p. 1890.

21. Oehrlein, G.S., *Study of sidewall passivation and microscopic silicon roughness phenomena in chlorine-based reactive ion etching of silicon trenches.* Journal of Vacuum Science & Technology B: Microelectronics and Nanometer Structures, 1990. **8**(6): p. 1199.

22. Vyvoda, M.A., et al., *Effects of plasma conditions on the shapes of features etched in Cl{sub 2} and HBr plasmas. I. Bulk crystalline silicon etching.* Journal of Vacuum Science and Technology, A, 1998. **16**(6).

23. Okumura, T., *Inductively Coupled Plasma Sources and Applications.* Physics Research International, 2010. **2010**: p. 164249.

24. Choi, J.H., et al., *Fabrication of SiC nanopillars by inductively coupled SF6/O2 plasma etching.* Journal of Physics D: Applied Physics, 2012: p. 45-235204.

25. Noda, S., et al., *Investigation of ion transportation in high-aspect-ratio holes from fluorocarbon plasma for SiO 2 etching.* Thin Solid Films, 2000. **374**(2): p. 181-189.

26. Lärmer, F. and A. Schilp, *Method of anisotropically etching silicon*, S. Robert Bosch GmbH, Germany, Editor. 1992, Robert Bosch GmbH: United States.

27. Sainiemi, L., *Cryogenic deep reactive ion etching of silicon micro and nanostructures.* Materials Science in Semiconductor Processing, 2009.

28. Donnelly, V.M. and A. Kornblit, *Plasma etching: Yesterday, today, and tomorrow*. Journal of Vacuum Science and Technology. A, Vacuum, Surfaces and Films, 2013. **31**(5).

29. Andersson, H., et al., *Micromachined flow-through filter-chamber for chemical reactions on beads.* Sensors & Actuators: B. Chemical, 2000. **67**(1): p. 203-208.

30. Matthews, B. and J.W. Judy, *Design and fabrication of a micromachined planar patch-clamp substrate with integrated microfluidics for single-cell measurements.* Journal of Microelectromechanical Systems, 2006. **15**(1): p. 214-222.

31. Busse, L.E., et al., *Antireflective surface structures on optics for high energy lasers*. 2014, SPIE. p. 89591L-89591L-6.

32. Taylor, C., et al., *Optical performance of random anti-reflection structures on curved surfaces*. 2015, SPIE. p. 935916-935916-8.

33. Joshi, R., G.J. Gbur, and M.K. Poutous. *Fabrication of Broadband Anti-reflective Surface on Fused Silica from Visible to SWIR Spectral Band*. in *OSA Advanced Photonics Congress (AP) 2019 (IPR, Networks, NOMA, SPPCom, PVLED)*. 2019. Burlingame, California: Optical Society of America.

34. Busse, L., et al., *Anti-reflective surface structures for spinel ceramics and fused silica windows, lenses and optical fibers.* Optical Materials Express, 2014. **4**(12): p. 2504-2515.

35. Sanghera, J.S., et al. *High Damage Threshold Anti-reflection Surfaces Based on "Motheye" Nano-structures*. in *Laser Ignition Conference*. 2015. Argonne, Illinois: Optical Society of America.

36. He, L., *Optical surface characterization with the structure function.* 2013.

37. Shanmugam, R., *Statistics for scientists and engineers.* 2015.

38. Roxhed, N., P. Griss, and G. Stemme, *Amethod for tapered deep reactive ion etching using a modified bosch process.* Journal of Micromechanics and Microengineering, 2007. **17**(5): p. 1087-1092.

39. D'Agostino, R. and D.L. Flamm, *Plasma etching of Si and SiO2 in SF6_O2 mixtures.* Journal of Applied Physics, 1981. **52**.

40. Lilienthal, K., et al., *Fused silica glass grass: fabrication and utilization.* Journal of Micromechanics and Microengineering, 2010. **20**(2): p. 025017.

41. Kolari, K., V. Saarela, and S. Franssila, *Deep plasma etching of glass for fluidic devices with different mask materials.* Journal of Micromechanics and Microengineering, 2008. **18**(6): p. 064010.

42. Southwell, W.H., *Gradient-index antireflection coatings.* Optics letters, 1983. **8**(11): p. 584-586.

43. Schulz, U., et al., *Gradient index antireflection coatings on glass containing plasma-etched organic layers.* Optical Materials Express, 2015. **5**(6): p. 1259-1265.

44. Taylor, C.D., *Optical performance of random anti-reflection structured surfaces (rARSS) on spherical lenses*. 2016, Ann Arbor: ProQuest LLC.

45. Taylor, C.D., et al., *Angle-of-incidence performance of random anti-reflection structures on curved surfaces.* Applied optics, 2016. **55**(9): p. 2203-2213.

46. Azzam, R.M.A., N.M. Bashara, and D. Thorburn Burns, *Ellipsometry and polarized light : North Holland, Amsterdam, 1987 (ISBN 0-444-87016-4). xvii + 539 pp. Price Dfl. 75.00.* Analytica Chimica Acta, 1987. **199**: p. 283-284.

47. Yeh, P., A. Yariv, and A.Y. Cho, *Optical surface waves in periodic layered media.* Applied Physics Letters, 1978. **32**(2): p. 104-105.

48. Fujiwara, H., *Spectroscopic ellipsometry principles and applications.* 2007.